Université de Lille
Centre national de la recherche scientifique (CNRS)

PhLAM Laboratoire de Physique des Lasers, Atomes et Molécules (UMR 8523)
Ecole doctorale Science de la Matière, du Rayonnement et de l'Environnement
(**ED SMRE**)

En vue de l'obtention du grade de docteur

Quantum Temporal Imaging with Single Photons and Photon Pairs

Imagerie Temporelle Quantique avec Photons Uniques et Paires de Photons

---

Présentée par Shivang Srivastava

Thèse de doctorat en Physique

Dans la specialité Milieux dilués et optique fondamentale

Soutenue le 29 mars 2024 devant le jury composé de:

Prof. Fabrice Devaux	Université de Franche-Comté	Rapporteur et président du jury
Prof. Nicolas J. Cerf	Université Libre de Bruxelles	Rapporteur
Prof. Polina P. Kuzhir	University of Eastern Finland	Examinatrice
Prof. Mikhail I. Kolobov	Université de Lille	Directeur de thèse
Dr. Dmitri B. Horoshko	CNRS, Université de Lille	Co-encadrant de thèse

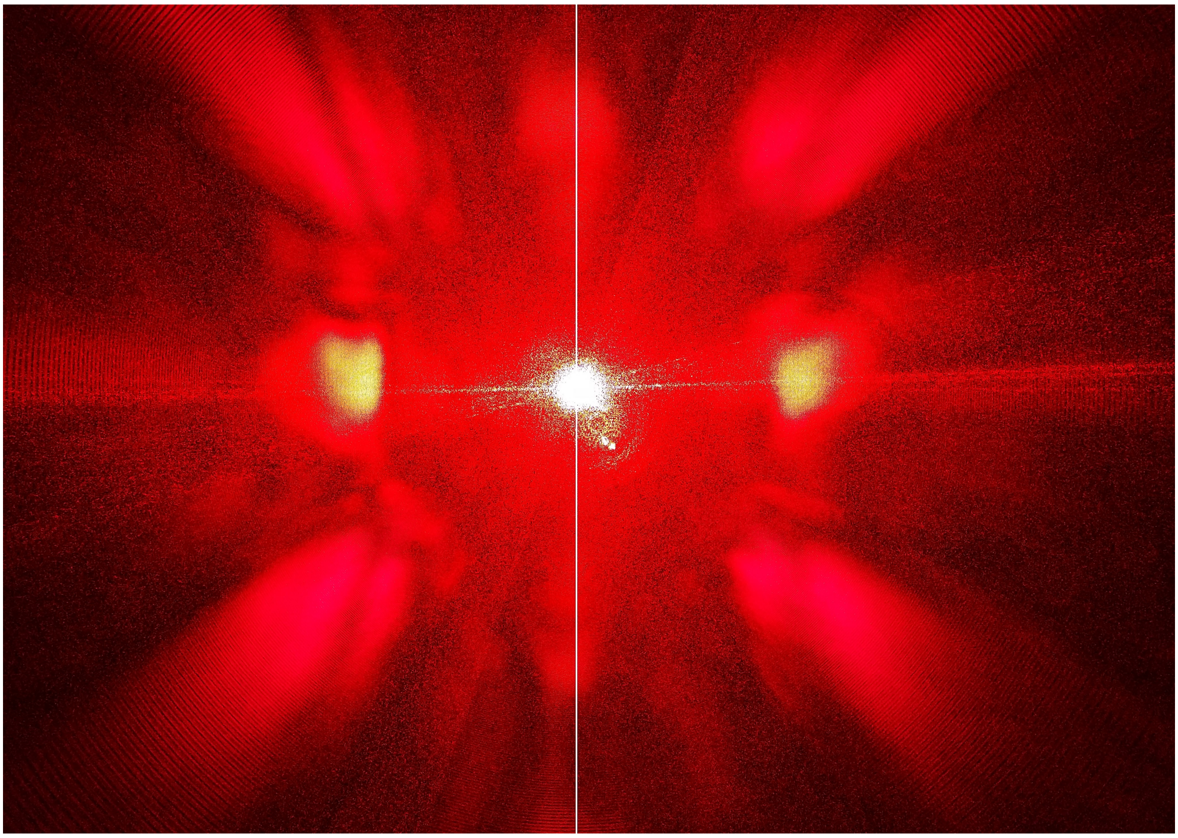

तमसो मा ज्योतिर्गमय ।

Acknowledgement

This thesis work was supported by the network QuantERA of the European Union's Horizon 2020 research and innovation program under the project Quantum Information and Communication with High-Dimensional Encoding (QuICHE), the French part of which is funded by Agence Nationale de la Recherche via Grant No. ANR-19-QUAN-0001. This contribution owes much to the collaboration and support of various institutions and organizations. Specifically, I extend my gratitude to the Université de Lille, the Centre national de la recherche scientifique (CNRS), the PhLAM Laboratory led by Cristian Focsa, the Doctoral School SMRE, with Christophe Van Brussel as coordinator, Frédéric Parol as director and Céline Toubin, director of doctoral studies. I sincerely thank them for their contributions.

I extend my thanks to the esteemed members of the committee for their invaluable participation and contributions to the public defense of this thesis: Professor Fabrice Devaux from the Université de Franche-Comté, Professor Nicolas Cerf from the Université Libre de Bruxelles, and Professor Polina Kuzhir from the University of Eastern Finland. Additionally, I express my thanks to Professor Nicolas Treps, Professor Stephan De Bièvre, and Professor Saliya Coulibaly for being part of my comité de suivi de thèse. I feel fortunate to have my work endorsed by such distinguished scientists.

I am extremely grateful to my directeur de thèse Professor Mikhail Kolobov for giving me this incredible opportunity to work in his group even though I was not experienced with the subject of research. While the situations were challenging at the beginning of my tenure, he consistently provided the support and guidance necessary for me to conduct my research effectively. Furthermore, under his supervision, I gained valuable insights into scientific communication, emphasizing the importance of focusing on ideas and also technical details. Doctor Dmitri Horoshko, my co-encadrant de thèse, has been instrumental in the success of my PhD. I owe him immense gratitude for imparting the foundational knowledge and mathematical tools necessary for conducting high-quality research in quantum optics. His guidance not only enriched my understanding but also honed my skills in scientific writing. With his boundless ideas, unwavering enthusiasm, moral support, and valuable advice, I was able to complete my thesis in time with high-impact publications successfully. I extend my heartfelt appreciation to Doctor Giuseppe Patera for conducting my interview for the PhD position, handling all the administrative tasks associated with my arrival in Lille, and assisting me in settling into the new environment. His guidance in the initial stages gave me valuable insights into my PhD subject's theory, paving the way for collaborative work ahead.

I am thankful to the human resources team at the PhLAM laboratory, particularly Walter Kolnierzak, for his prompt assistance with administrative matters, and to Hervé Damart for his information technology and electronic support. I also want to extend my appreciation to the secretary Nathalie Damart and the printing staff for their assistance. None of my administrative tasks in France would have been possible without the constant support of the CNRS délégation Hauts-de France human resources team: Ingrid Tiberghien and Coralie Docquois. Their efforts made everything easy for me in a foreign country, and I am truly thankful for their assistance.

For sure, life in Lille would not have been the same without friends. I will always cherish the moments shared with my office mates who became friends, Corentin, Martin, and Jordan, who made work enjoyable and memorable. Special mention goes to Corentin for his friendship, French lessons, and inviting me to various events. Working alongside Martin on the Optica Society student chapter and sharing laughter with Jordan made office life lively. Then there are those friends who've become like family: Alexandre, Cécilia, and Christelle with whom I never felt alone in the beginning and constantly received the feeling of a family atmosphere. Cheers to all the unforgettable moments we have passed together which are engraved in my mind forever. The circle of friends continued to grow, with each person adding something unique: Vikas, Rabih, Tony, Georges, Elias, and Rajesh. Thanks to Vikas for introducing me to the Indian markets in Lille and enjoying numerous coffee breaks. Rabih offered moral support in Lille and always openly gave his point of view, a highly desired trait in research. Thanks to Elias for all our historical and geopolitical discussions which were very important to deviate our minds during lunch hours. I would like to extend my thanks to Jean Dora for being an important support during hard times and for encouraging and motivating me before and throughout this journey. I can never forget my friends from India: Siddhant, Shaurya, Manohar, and Pragalbh. for their constant motivational support during my PhD journey. Your encouragement kept me going during tough times. I'll forever cherish the memories we created.

I owe a debt of gratitude to my family for their unwavering support throughout my thesis journey. I couldn't have reached this milestone without daily conversations with my father, mother, and sister nearly every day. Their constant support and help made me reach this stage in my life. I am deeply grateful for their emphasis on education and their belief in me. Growing up in such a nurturing environment inspired my passion for physics and paved the way for the success of my PhD. Thank you, Papa, Mummy, and Didi, for everything. *Aap sab ko mera bahut bahut dhanyawaad aur asha karte hain ki aap logon ki kripa humesha aise hi bani rahegi.*

Je voudrais également remercier ma belle-famille qui m'a donné le sentiment d'appartenir à ma propre famille loin de chez moi, je n'aurais pas pu espérer un accueil plus chaleureux. Merci à tous les événements et les fêtes que nous avons organisés ensemble, qui m'ont maintenu impliqué dans des activités en dehors de la recherche et m'ont aidé à m'intégrer dans la culture, la cuisine et la langue françaises.

Finally, I would like to express my profound gratitude to my compagne de vie, Alyssa, for her immense support throughout every challenge I encountered during my PhD. She stood by me during my highs and lows, an unforgettable presence to whom I attribute much of the success of this journey. I cannot imagine completing this PhD without her by my side, and I am incredibly thankful for her integral role in this. Her creative thinking inspired me during presentations and discussions, and our shared moments together have been invaluable in shaping this path.

Contents

List of Symbols

$A_i(t)$ Annihilation operator for a photon at time t

$A(z,\tau)$ Group delayed envelope of the optical pulse

C Degree of coherence in an optical beam

D_{f} Focal group delay dispersion (GDD) of a time lens

E_0 Peak amplitude of the optical pulse

$E_\mu^{(+)}(t,x)$ Positive frequency part of the field. μ is the index of polarization, o for ordinary wave and e for extraordinary wave

$G_d^{(1)}(t,\tau)$ First-order autocorrelation function of the delayed ordinary wave

$I_\mu(t)$ Average intensity of a photon

$\tilde{J}_0(t,t')$ Zero-centered joint temporal amplitude (JTA) of two PDC generated photons

$J(\Omega,\Omega')$ Joint spectral amplitude (JSA) of the two generated photons

K Schmidt number of the photon pairs

M Magnification by the temporal imaging system

P_b Probability of biphoton generation per pump pulse

$p_{\mathrm{int}}(\delta\tau)$ Conditional probability of destructive interference of two photons under the condition that they are generated

$P_{12}(t_1,t_2;\delta\tau)$ Probability of detecting one photon at time t_1 and one photon at time t_2 at the detectors

$R_c(\delta\tau)$ Average coincidence counting rate

T_μ Dimensionless delay of a photon

V Visibility of the Hong-Ou-Mandel interference picture

$\alpha(\Omega)$ Pump spectral amplitude of the two generated photons

Δt_μ Temporal width of a photon

$\epsilon_\mu(\Omega,x)$ Annihilation operator of a photon at position x with the frequency $\omega_0+\Omega$

τ_i Radiative lifetime of a quantum dot

τ_p Transform-limited full temporal width at half maximum (FWHM) for the pump pulse

τ_μ Relative group delay of a photon with respect to the pump at half crystal length

$\Phi(\Omega,\Omega')$ Phase-matching function of the photon pairs

Introduction

When wireless is perfectly applied, the whole earth will be converted into a huge brain.

– Nikola Tesla

Historical background

Electromagnetism, with its origins in ancient times, developed through a timeline of exploration and understanding. The 17th century marked a pivotal moment with the publication of Isaac Newton's "Opticks," where he presented his theory of colors and the nature of light. Classical optics reached new heights with Thomas Young's double-slit experiment, establishing the wave theory of light. The 19th century concluded with the unification of optics and electromagnetism by James Clerk Maxwell, setting the stage for the profound advances in optics that would follow in the modern era. The late 1800s witnessed the meticulous experiments of Albert A. Michelson, whose innovative work, including the famous Michelson-Morley experiment in 1887, played a crucial role in confirming Maxwell's theories and contributed to the development of modern optics. The experimental confirmation of Maxwell's predictions by Heinrich Hertz solidified the acceptance of the wave theory of light.

Quantum mechanics emerged from the challenge of the ultraviolet catastrophe in black body radiation. Planck's solution introduced energy quantization, inspiring Einstein to propose photons to explain the photoelectric effect. While Einstein was right about photons, a complete understanding of the photoelectric effect involves quantizing matter. Photons are elementary excitations of the electromagnetic field, much like electrons in the electron field. In today's quantum field theory, these fields form the foundational basis for our understanding of the Universe. Quantum electrodynamics (QED), describing the interaction between light and matter, stands as history's most successful theory, validated by precise predictions like the electron's anomalous magnetic moment.

The profound insights of quantum mechanics have catalyzed innovative technological advancements, notably exemplified by the transistor—a basis of modern electronics and the laser, widely applied in fields from metrology to medicine. While the operational principles of lasers are inherently quantum mechanical, the light they produce can be comprehensively explained by Maxwell's theory of electromagnetism. Yet, certain states of light fundamentally adhere to quantum mechanics, a concept beyond Maxwell's era. This revelation has led to unprecedented ways to perceive and interact with the world. Recent technological progress enables the creation of systems pushing light and matter to their ultimate quantum limits, promising exciting paths for exploring fundamental phenomena and designing innovative quantum technologies.

This thesis is devoted to the study of systems in which we characterize and manipulate the photons, for their applications in quantum technologies.

Origins of quantum technologies

With the revolutionary concepts introduced by quantum mechanics in the early 20th century, the properties of the quantum states such as the quantum superposition of states or entanglement led to the dawn of quantum technologies. As a notable example, a discipline founded on the concept of the *qubit*, the quantum counterpart to the fundamental unit of information in classical physics is *quantum information theory* [1].

Alan Turing's seminal paper "Computing Machinery and Intelligence" [2] is considered to have led the classical computation revolution, creating the model of *Turing machine*, and later bearing the idea of classical *bits* of computation. Quantum bits of the information or the qubits exist in a superposition of the states $|0\rangle$ and $|1\rangle$ *i.e.* $|\psi\rangle = \alpha|0\rangle + \beta|0\rangle$, where the probability amplitudes α and β are complex numbers. These amplitudes not only encode the probabilities of the outcomes of measurement but also the relative phase between them is responsible for the *quantum interference*.

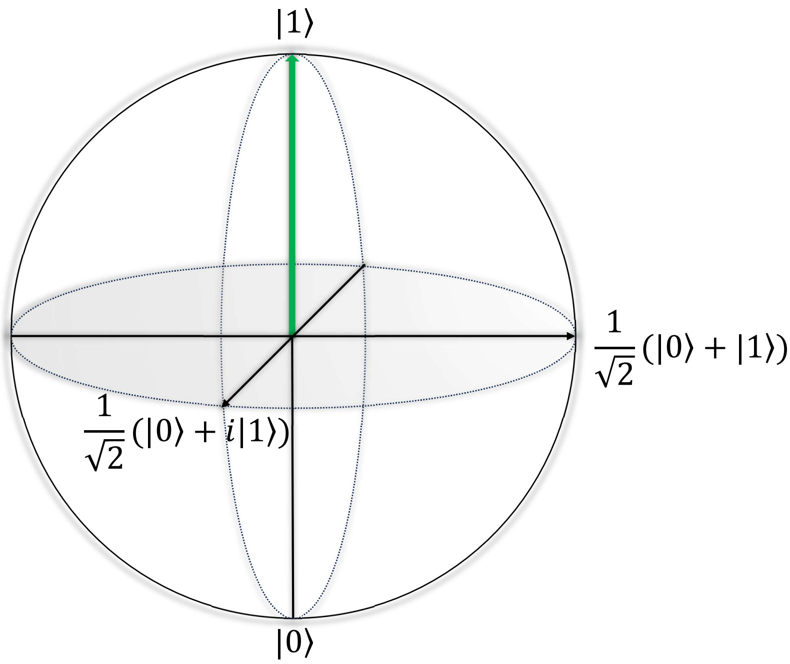

Figure 1: Geometrical representation of a two-level quantum system in the ground state $|0\rangle$ and the excited state $|1\rangle$, which can also exist in an arbitrary superposition of the two. This representation, known as the Bloch sphere, presents the qubit—the fundamental unit of information in quantum physics.

Quantum information theory, as highlighted by its applications in quantum cryptography [3], has emerged as the foundation for quantum computers [4]. These computers, leveraging the parallel computation of quantum superposition of qubits, achieve success in solving calculations of scales deemed impossible for classical computers [5]. Photon, with its ability to encode information in multiple degrees of freedom like polarization, frequency, or spatiotemporal modes, stands out as the ideal candidate for such tasks. In quantum communication [6], where low noise properties of photons are essential, they serve as quantum channels carrying qubits between nodes in a quantum network. Furthermore, photons prove to be very interesting contenders for various quantum information phenomena, notably the first demonstration of entanglement [7, 8] and their quantum state finds application in diverse quantum engineering domains, including *quantum metrology*, *quantum lithography*, or *quantum imaging* [9].

Quantum approach to temporal imaging

Quantum technologies are expected to revolutionize many aspects of human life, bringing numerous scientific and societal benefits. A global quantum network is envisaged by many scientists, where quantum processors, sensors, and memories at local nodes will be interconnected by optical fields in highly entangled states [10, 11]. One of the key elements of such networks are photonic-photonic interconnects [11], transforming the physical parameters of the optical carrier while leaving the encoded quantum information untouched, e.g. converting picosecond-scale pulses in the telecommunication band, optimal for high-rate fiber transmission, to nanosecond-scale pulses in the visible range processed by quantum memories. An efficient tool for such transformations is provided by the technique of temporal imaging [12, 13] allowing one to stretch and compress optical waveforms in time.

Classical temporal imaging is a technique of manipulation of ultrafast temporal optical waveforms similar to the manipulation of spatial wavefronts in conventional spatial imaging [12, 13]. It is based upon the so-called space-time duality or the mathematical equivalence of the equations describing the propagation of the temporal pulses in dispersive media and the diffraction of the spatial wavefronts in free space. Temporal imaging was first discovered in purely electrical systems, then extended to optics [14], and later converted into all-optical technologies using the development of non-linear optics and ultrashort-pulse lasers [15–17]. In the past two decades, classical temporal imaging has become a very popular tool for manipulating ultrafast temporal waveforms with numerous applications such as temporal stretching of ultrafast waveforms and compression of slow waveforms to sub-picosecond time scales, temporal microscopes, time reversal, and optical phase conjugation.

One of the key elements in classical temporal imaging is a time lens which introduces a quadratic time phase modulation into an input waveform, similar to the quadratic phase factor in the transverse spatial dimension, introduced by a conventional lens. Nowadays, optical time lenses are based on electro-optic phase modulation (EOPM) [15, 18, 19], cross-phase modulation [20, 21], sum-frequency generation (SFG) [22–26], or four-wave mixing (FWM)[27–30] and also on atom-cloud based quantum memory [31]. The temporal magnification factors of the order more than 100 times have been reported.

Quantum temporal imaging is a recent topic of research that brings the ideas from spatial quantum imaging [9, 32, 33] into the temporal domain. Quantum temporal imaging searches for such manipulations of non-classical temporal waveforms which preserve their nonclassical properties such as squeezing, entanglement, or nonclassical photon statistics. Some works have already been published on this subject. Schemes for optical waveform conversion preserving the nonclassical properties such as entanglement [34] and for aberration-corrected quantum temporal imaging of a coherent state [35] have been proposed. Spectral bandwidth compression of light at a single-photon level has been experimentally demonstrated by SFG [36] and EOPM [37–39]. Temporal imaging in the single-photon regime has been demonstrated with an atomic-cloud-based quantum memory [40, 41]. Quantum temporal imaging has been demonstrated for one photon of an entangled photon pair by SFG [42] and for both photons by EOPM [43]. Quantum temporal imaging of broadband squeezed light was studied for SFG [44–46], and FWM-based [47] lenses. In Ref. [48], it was demonstrated that a time lens can preserve nonclassical effects such as antibunching and sub-Poissonian statistics of photons. In Ref. [49] a temporal magnification of two weak coherent pulses with a picosecond-scale delay by FWM was reported.

Second-order autocorrelation function and Schmidt modes

The normalized second-order autocorrelation function of the optical field, $g^{(2)}(\tau)$, where τ is a time delay, is a powerful tool for determining the physical properties of light beams and their sources [50, 51]. In particular, the value of this function at $\tau = 0$ reveals the statistics of the photons: $g^{(2)}(0) = 2$ for a Gaussian statistics, $g^{(2)}(0) = 1$ for a Poissonian one, and the value $g^{(2)}(0) < 1$ indicates the phenomenon of photon antibunching, which is a signature of field nonclassicality [51]. Measurement of this function with fully resolved temporal dependence became in the last decade a routine task in the characterization of single-photon sources such as quantum dots [52], single molecules [53], and color centers in diamonds [54], where its width is in the nanosecond scale, above the resolution time of modern photodetectors amounting to about 100 ps. Another important source of single photons and photon pairs, parametric downconversion (PDC), is, however, hard to characterize in this way, because of a rather high bandwidth, more than 1 THz, of the generated light, placing the typical width of the $g^{(2)}(\tau)$ function into the sub-picosecond range, well below the photodetector resolution time. A time-integrated second-order autocorrelation function $g^{(2)}_{\text{int}}$ was introduced for this case [55], which in particular allows one to determine the number of Schmidt modes K of two entangled beams by measuring the autocorrelation function of one of them: $K = (g^{(2)}_{\text{int}} - 1)^{-1}$. However, in a highly multimode case, when $g^{(2)}_{\text{int}} \to 1$, the evaluated number of modes becomes highly sensitive to the measurement error in determining $g^{(2)}_{\text{int}}$.

Time-resolved measurement of the second-order autocorrelation function for a broadband field is possible with the help of the temporal imaging technique, allowing one to stretch or compress optical waveforms in time. Recent experiments with single photons [49, 56] demonstrated the possibility of bringing their picosecond-scale temporal features to the nanosecond scale, thus paving the way to the time-resolved measurement of the $g^{(2)}(\tau)$ function. In this thesis, we will also demonstrate how the temporal width of the second-order autocorrelation function measured in this way can be used for a precise determination of the number of Schmidt modes in PDC.

Organization of the thesis

This thesis is organized in the following way. First, we begin by introducing the elements of quantum optics and imaging which are necessary and sufficient to understand the underlying concepts of this thesis. We go through field quantization, examples of non-classical states of light, an overview of temporal imaging in the classical domain, and its effective implementation through quantum theory. The discussion also delves into the quantum behavior exhibited by photons, distinguishing them from classical light fields. Moving forward to Chapter 2, the focus turns to the parametric downconversion of a field and the generation of photon pairs in a non-linear crystal. We explain the spectro-temporal shape of the photon and how a time lens can be used to manipulate it. We show this by analyzing the quantum interference of the photons when their temporal shapes are made identical.

In Chapter 3, the exploration extends to a time telescope, capable of noiselessly stretching input waveforms without introducing residual phase chirp. The classification of time telescopes is outlined, emphasizing conditions under which minimal dispersion occurs. This time telescope is later considered in two different optical circuits with different light sources proving it to be an important instrument in photonic quantum networks. Finally, Chapter 4 establishes a link between temporal intensity correlations (a classical phenomenon) and Schmidt-mode decompositions of the joint spectral amplitude of ordinary photon pairs (a quantum phenomenon). This facilitates an important way towards counting temporal modes of a pulse produced in parametric downconversion with precision and towards quantum state engineering, allowing us to encode quantum information in multiple temporal modes.

Chapter 1

Fundamentals of quantum optics and imaging

Learning never exhausts the mind.

– Leonardo da Vinci

This chapter is devoted to theoretical study of the subject which is necessary to understand in the following chapters. We commence Section 1.1 by discussing the quantized electromagnetic field with examples of non-classical states of light. Next, Section 1.2 illustrates the space-time duality in optics and establishes a mathematical connection between the monochromatic beam expansion due to paraxial diffraction and the manipulation of a quasi-monochromatic pulse in narrowband dispersion. Furthermore, in Section 1.3 we consider the elements of quantum temporal imaging systems and the transformation of a pulse propagating through a nonlinear medium. Finally, we finish this chapter with Section 1.4 by learning several properties of nonclassical light and addressing the sub-Poissonian statistics, anti-bunching, and indistinguishability of photons.

1.1 Quantization of the electromagnetic field

In the realm of modern physics, the quantization of the electromagnetic field stands as a profound and fundamental pillar upon which the structure of the quantum theory of light is constructed. The electromagnetic field, as envisioned by James Clerk Maxwell's equations in the mid-19th century, is a complex and dynamic entity. It is responsible for the transmission of light, the behavior of charged particles, and the fundamental forces that govern the universe. In this section, we study the derivation of the wave equation and its solution for the quantum electric field operator from Maxwell's equations. The key steps outlined here can be found in several books on quantum optics [51, 57–59].

Maxwell's equations: Classical formulation

Maxwell's equations, a set of four fundamental equations that describe the behavior of electric and magnetic fields in free space, depict the foundations of classical electromagnetism. These equations for the free field in vacuum in the SI convention are formulated as

$$\nabla \mathbf{E}(\mathbf{r}, t) = 0, \tag{1a}$$

$$\nabla \times \mathbf{E}(\mathbf{r}, t) = -\frac{\partial \mathbf{B}(\mathbf{r}, t)}{\partial t}, \tag{1b}$$

$$\nabla \mathbf{B}(\mathbf{r}, t) = 0, \tag{1c}$$

$$\nabla \times \mathbf{B}(\mathbf{r}, t) = \mu_0 \epsilon_0 \frac{\partial \mathbf{E}(\mathbf{r}, t)}{\partial t}, \tag{1d}$$

where the spatial and time depending vectors $\mathbf{E}(\mathbf{r}, t)$ and $\mathbf{B}(\mathbf{r}, t)$ are the *electric* and *magnetic field strengths*, ϵ_0 is vacuum permittivity and μ_0 is vacuum permeability. We introduce the *vector potential* $\mathbf{A}(\mathbf{r}, t)$ and the *scalar potential* $V(\mathbf{r}, t)$ to perform the quantization and we express the electric and magnetic field strengths as

$$\mathbf{E}(\mathbf{r}, t) = -\frac{\partial \mathbf{A}(\mathbf{r}, t)}{\partial t} - \nabla V(\mathbf{r}, t), \qquad \mathbf{B} = \nabla \times \mathbf{A}(\mathbf{r}, t). \tag{2}$$

Inserting Eq. (2) into Eqs. (1a-1d) evaluates Maxwell's equations to

$$\nabla(\nabla \mathbf{A}(\mathbf{r}, t)) - \nabla^2 \mathbf{A}(\mathbf{r}, t) + \frac{1}{c^2}\frac{\partial^2 \mathbf{A}(\mathbf{r}, t)}{\partial t^2} + \frac{1}{c^2}\nabla \frac{\partial V(\mathbf{r}, t)}{\partial t} = 0, \tag{3a}$$

$$\nabla^2 V(\mathbf{r}, t) + \nabla \frac{\partial \mathbf{A}(\mathbf{r}, t)}{\partial t} = 0. \tag{3b}$$

Here, c is the speed of light,

$$c = (\epsilon_0 \mu_0)^{-1/2}, \tag{4}$$

and the vector identity being used reads

$$\nabla \times \nabla \mathbf{A}(\mathbf{r}, t) = \nabla(\nabla \mathbf{A}(\mathbf{r}, t)) - \nabla^2 \mathbf{A}(\mathbf{r}, t), \tag{5}$$

where

$$\nabla^2 \equiv \frac{\partial^2}{\partial x^2} + \frac{\partial^2}{\partial y^2} + \frac{\partial^2}{\partial z^2}, \tag{6}$$

is the Laplacian operator.

Gauge transformations and the free classical field

We can simplify the solution of Eqs. (3a, 3b) by imposing another condition of expressing the vector potential using the *gauge transformation*,

$$\mathbf{A}'(\mathbf{r},t) = \mathbf{A}(\mathbf{r},t) + \nabla f(\mathbf{r},t), \tag{7}$$

where $f(\mathbf{r},t)$ is a function of space and time.

Now, we specify the condition of *Coulomb gauge*, $\nabla\mathbf{A}(\mathbf{r},t) = 0$ and $V(\mathbf{r},t) = 0$. By definition of the Coulomb gauge, $\mathbf{A}(\mathbf{r},t)$ is a transverse vector field. In this way, the transverse component of the electric field is given by

$$\mathbf{E}(\mathbf{r},t) = -\frac{\partial\mathbf{A}(\mathbf{r},t)}{\partial t}. \tag{8}$$

This helps us to understand that the transverse equation of the electric field signifies the electromagnetic wave. The first step towards field quantization is to consider the electromagnetic field in a free space without the electric and magnetic charges. In this scenario, the gauge transformation leads to the wave equation

$$\nabla^2\mathbf{A}(\mathbf{r},t) - \frac{1}{c^2}\frac{\partial^2\mathbf{A}(\mathbf{r},t)}{\partial t^2} = 0. \tag{9}$$

To obtain a formal solution to the above equation in terms of normal modes, we confine the electromagnetic field inside a cubicle box of volume $V = L^3$, L is the side length, and take periodic boundary conditions. Through this, we expand the vector potential as a sum of contributions from the modes of the box and arrive at

$$\mathbf{A}(\mathbf{r},t) = \sum_{\mu}\sum_{\mathbf{k}} \mathbf{e}_{\mathbf{k},\mu}\left[\varepsilon_{\mathbf{k},\mu}e^{-i\omega_k t + i\mathbf{k}\mathbf{r}} + \varepsilon^*_{\mathbf{k},\mu}e^{i\omega_k t - i\mathbf{k}\mathbf{r}}\right], \tag{10}$$

where, $\mathbf{k}$ is the wavevector which can take the values $\mathbf{k} = (k_x, k_y, k_z) = 2\pi/L\times(n_1, n_2, n_3)$ and $n_1, n_2, n_3 \in \mathbb{Z}$. The polarization vectors $\mathbf{e}_{\mathbf{k},\mu}$ satisfy $\mathbf{e}_{\mathbf{k},\mu}\mathbf{k} = 0$ and $\mathbf{e}_{\mathbf{k},\mu}\mathbf{e}_{\mathbf{k},\nu} = \delta_{\mu,\nu}$ and $\omega_k = |\mathbf{k}|c$.

At this step, we write the Hamiltonian of the system of the classical fields as the integral of the energy density over the entire space

$$H_{EM} = \frac{1}{2}\int_V \mathrm{d}V\left[\epsilon_0\mathbf{E}^2(\mathbf{r},t) + \frac{1}{\mu_0}\mathbf{B}^2(\mathbf{r},t)\right]. \tag{11}$$

We identify this Hamiltonian with the harmonic oscillator by obtaining $\mathbf{E}(\mathbf{r},t)$ and $\mathbf{B}(\mathbf{r},t)$ in terms of $\mathbf{A}(\mathbf{r},t)$. So, we substitute Eq. (10) into Eq. (2) and arrive at

$$H_{EM} = \epsilon_0 V\sum_{\mu}\sum_{\mathbf{k}} \omega_k^2\left(\varepsilon_{\mathbf{k},\mu}\varepsilon^*_{\mathbf{k},\mu} + \varepsilon^*_{\mathbf{k},\mu}\varepsilon_{\mathbf{k},\mu}\right). \tag{12}$$

Now, we decompose the amplitude $\varepsilon_{\mathbf{k},\mu}$ into its real and imaginary parts, $p_{\mathbf{k},\mu}$ and $q_{\mathbf{k},\mu}$,

$$\varepsilon_{\mathbf{k},\mu} = \frac{1}{2\omega_k(\epsilon_0 V)^{1/2}}[\omega_k q_{\mathbf{k},\mu} + ip_{\mathbf{k},\mu}], \tag{13}$$

so that the Hamiltonian (11) takes the form

$$H_{EM} = \frac{1}{2}\sum_{\mu}\sum_{\mathbf{k}}\left[\omega_k^2 q_{\mathbf{k},\mu}^2 + p_{\mathbf{k},\mu}^2\right]. \tag{14}$$

Quantization

We now quantize the electric field, by converting the classical coefficients into quantum operators. Each pair of classical quantities $p_{\mathbf{k},\mu}$, $q_{\mathbf{k},\mu}$ represent the *canonical coordinates* and satisfy the Poissons bracket relations,

$$\{q_{\mathbf{k},\mu}, q_{\mathbf{k}',\nu}\} = 0,\ \{p_{\mathbf{k},\mu}, p_{\mathbf{k}',\nu}\} = 0,\ \{q_{\mathbf{k},\mu}, p_{\mathbf{k}',\nu}\} = \delta_{\mathbf{k},\mathbf{k}'}\delta_{\mu\nu}. \tag{15}$$

We follow the canonical quantization scheme and convert these coordinates into quantum operators $\hat{p}_{\mathbf{k},\mu}$ (momentum operator), $\hat{q}_{\mathbf{k},\mu}$ (position operator) by replacing the classical Poisson brackets with commutators multiplied with $(i\hbar)^{-1}$,

$$[\hat{q}_{\mathbf{k},\mu}, \hat{q}_{\mathbf{k}',\nu}] = 0,\ [\hat{p}_{\mathbf{k},\mu}, \hat{p}_{\mathbf{k}',\nu}] = 0,\ [\hat{q}_{\mathbf{k},\mu}, \hat{p}_{\mathbf{k}',\nu}] = i\hbar\delta_{\mathbf{k},\mathbf{k}'}\delta_{\mu\nu}. \tag{16}$$

We use these quantum operators to define the quantum creation and annihilation operators ,

$$\hat{a}_{k,\mu} = \frac{1}{(2\hbar\omega_k)^{1/2}}[\omega_k q_{\mathbf{k},\mu} + ip_{\mathbf{k},\mu}], \tag{17a}$$

$$\hat{a}_{k,\mu}^\dagger = \frac{1}{(2\hbar\omega_k)^{1/2}}[\omega_k q_{\mathbf{k},\mu} - ip_{\mathbf{k},\mu}], \tag{17b}$$

which satisfy the bosonic commutation relations,

$$[\hat{a}_{\mathbf{k},\mu}, \hat{a}_{\mathbf{k}',\nu}] = [\hat{a}_{\mathbf{k},\mu}^\dagger, \hat{a}_{\mathbf{k}',\nu}^\dagger] = 0, \tag{18a}$$

$$[a_{\mathbf{k},\mu}, \hat{a}_{\mathbf{k}',\nu}^\dagger] = \delta_{\mathbf{k},\mathbf{k}'}\delta_{\mu\nu}. \tag{18b}$$

In terms of these operators, the quantum Hamiltonian operator takes the form

$$\hat{H}_{EM} = \sum_{\mu}\sum_{\mathbf{k}} \hbar\omega_k\left(\hat{a}_{\mathbf{k},\mu}^\dagger\hat{a}_{\mathbf{k},\mu} + \frac{1}{2}\right). \tag{19}$$

Therefore, the electromagnetic field is explained as a collection of quantum harmonic oscillators of frequency ω_k. We make the amplitudes $\varepsilon_{\mathbf{k},\mu}$ the quantum operators and substitute into Eq. (10) and arrive at the electric field operator,

$$\hat{E}(\mathbf{r},t) = i\sum_{\mu}\sum_{\mathbf{k}}\left(\frac{\hbar\omega_k}{2\epsilon_0 V}\right)^{1/2}\mathbf{e}_{\mathbf{k},\mu}\left[\hat{a}_{\mathbf{k},\mu}e^{i(\mathbf{kr}-\omega_k t)} - \hat{a}^{\dagger}_{\mathbf{k},\mu}e^{-i(\mathbf{kr}-\omega_k t)}\right]. \tag{20}$$

We observe that the electric field operator we obtained in Eq. (20), can be expressed as the sum of positive and negative frequency parts,

$$\hat{E}(\mathbf{r},t) = \hat{E}^{(+)}(\mathbf{r},t) + \hat{E}^{(-)}(\mathbf{r},t). \tag{21}$$

where

$$\hat{E}^{(+)}(\mathbf{r},t) = i\sum_{\mu}\sum_{\mathbf{k}}\left(\frac{\hbar\omega_k}{2\epsilon_0 V}\right)^{1/2}\mathbf{e}_{\mathbf{k},\mu}\hat{a}_{\mathbf{k},\mu}e^{i(\mathbf{kr}-\omega_k t)}, \tag{22a}$$

$$\hat{E}^{(-)}(\mathbf{r},t) = -i\sum_{\mu}\sum_{\mathbf{k}}\left(\frac{\hbar\omega_k}{2\epsilon_0 V}\right)^{1/2}\mathbf{e}_{\mathbf{k},\mu}\hat{a}^{\dagger}_{\mathbf{k},\mu}e^{-i(\mathbf{kr}-\omega_k t)}. \tag{22b}$$

Fock states

Until now, we understood the mathematical formalism of quantizing a free electromagnetic field, however, it is mandatory to discuss an example of a nonclassical state of the light. The Eq. (19) revealed that each of the quantum Hamiltonians of each field mode resembles a quantum harmonic oscillator. To simplify, we limit our discussion to a single mode of the light field and omit the mode indices. We recall that the zero-point energy of the harmonic oscillator in the single mode of the light field reads $E_0 = \hbar\omega/2$ whereas, at the nth level, the energy is

$$E_n = E_0 + n\hbar\omega = \left(n + \frac{1}{2}\right)\hbar\omega. \tag{23}$$

We introduce the *photon number operator* $\hat{n} = \hat{a}^{\dagger}\hat{a}$ which fulfills the following eigenvalue equation

$$\hat{n}|n\rangle = n|n\rangle, \tag{24}$$

where the bosonic annihilation and creation operators satisfy the commutation relations

$$[\hat{a}, \hat{a}^{\dagger}] = 1, \tag{25a}$$

$$[\hat{a}, \hat{a}] = [\hat{a}^{\dagger}, \hat{a}^{\dagger}] = 0. \tag{25b}$$

This concept of number state representation leads us to the number states $|n\rangle$ which corresponds to the harmonic oscillator eigenstate with n quanta of energy excited above the ground state. Hence, we can write, $\hat{H}|n\rangle = E_n|n\rangle$, where $\hat{H} = \hbar\omega(\hat{a}^\dagger\hat{a} + \frac{1}{2})$ is the single-mode Hamiltonian, Eq. (19). The number states exhibit the properties of the Hermitian operators, orthonormality: $\langle n|n'\rangle = \delta_{nn'}$ and completeness: $\sum_{n=0}^{\infty}|n\rangle\langle n| = 1$. One can also show that the effect of annihilation and creation operators on the number states is

$$\hat{a}|n\rangle = n^{1/2}|n-1\rangle, \tag{26a}$$
$$\hat{a}^\dagger|n\rangle = (n+1)^{1/2}|n+1\rangle. \tag{26b}$$

The Eq. (26a) collapses to $\hat{a}|0\rangle = 0$ and Eq. (26b) implies that the number states can be built up from the vacuum state $|0\rangle$ by the following action

$$|n\rangle = \frac{1}{(n!)^{1/2}}(\hat{a}^\dagger)^n|0\rangle. \tag{27}$$

These photon number states are called *Fock states*.

Coherent states

Coherent states, with their indefinite number of photons, offer a more precisely defined phase compared to Fock states where the phase is completely random. Their product of the uncertainty in amplitude and phase complies with the minimum allowed by the uncertainty principle, making them the quantum states closest to a classical field description. Coherent states are the solutions of the eigenvalue equation

$$\hat{a}|\alpha\rangle = \alpha|\alpha\rangle. \tag{28}$$

The eigenvalue α is complex because $\hat{a}$ is a non-Hermitian operator. Now, the coherent states contain an indefinite number of photons, so they can be expanded in the Fock state basis as

$$|\alpha\rangle = e^{-|\alpha|^2/2}\sum_{n=0}^{\infty}\frac{\alpha^n}{(n!)^{1/2}}|n\rangle. \tag{29}$$

The absolute magnitude of the scalar product of two coherent states and their completeness relation take the forms respectively,

$$\left|\langle\beta|\alpha\rangle\right|^2 = e^{-|\alpha-\beta|^2}, \text{ and} \tag{30a}$$
$$\frac{1}{\pi}\int|\alpha\rangle\langle\alpha|\mathrm{d}^2\alpha = 1. \tag{30b}$$

Therefore, the coherent states α and β are not orthogonal, however in the limit $|\alpha - \beta| \gg 1$, they become approximately orthogonal.

These states are generated by the unitary displacement operator, $\hat{D}(\alpha)$, where, α is an arbitrary complex number. We define the displacement operator as

$$\hat{D}(\alpha) = e^{\alpha\hat{a}^\dagger - \alpha^*\hat{a}}. \tag{31}$$

This operator has a property $\hat{D}^\dagger(\alpha)\hat{a}^\dagger\hat{D}(\alpha) = \hat{a}^\dagger + \alpha^*$ that imposes a linear displacement, and operating $\hat{D}(\alpha)$ on the vacuum state, we get the coherent state $|\alpha\rangle$,

$$|\alpha\rangle = \hat{D}(\alpha)|0\rangle. \tag{32}$$

1.2 Space-time duality

In this section, we explore the fundamentals describing the transformation of a light field propagating through a dispersive medium as envisioned in Refs. [14, 17, 46]. The equation that describes the stretching or compression of a pulse in time as it propagates through a dispersive medium is mathematically equivalent to the equation that describes the transverse spreading of the light beam due to diffraction. We learn further how the paraxial diffraction is connected with the narrowband dispersion in the following parts of this section. After discussing the space-time duality, we consider the concepts of optical imaging. Optical imaging can be distinguished either into *spatial imaging*, which deals with the manipulation of a wavefront in space, or into *temporal imaging*, which allows us to manipulate a waveform in time. A wavefront is defined as the surface of the identical phase of a spatial wave distributed over the spatial coordinates, whereas, a waveform is the shape of a wave in the temporal domain distributed over time. To understand further we can think of these spatial and temporal distributions propagating along the z-axis, with the x and y degrees of freedom in space corresponding to the time t degree of freedom in time. These analogies establish the foundations of space-time duality and now we dive into the mathematics confirming these equivalences.

Paraxial diffraction: spatial domain

We begin by assuming that the wave is monochromatic and, the field can be written as

$$\mathbf{E}(\mathbf{r}, t) = \mathbf{E}_0(\mathbf{r})e^{-i\omega_0 t}. \tag{33}$$

Here, ω_0 is the *carrier frequency* and $\mathbf{E}_0(\mathbf{r})$ is the *field amplitude.*

Taking the partial derivative of Eq. (9) by time and using Eq. (8), we see that the electric field obeys the same wave equation (9) as the vector potential

$$\nabla^2\mathbf{E}(\mathbf{r}, t) - \frac{1}{c^2}\frac{\partial^2\mathbf{E}(\mathbf{r}, t)}{\partial t^2} = 0. \tag{34}$$

By Eq. (33), the wave equation can be simply reduced to the Helmholtz equation,

$$(\nabla^2 + \frac{\omega_0^2}{c^2})\mathbf{E}_0(x, y, z) = 0. \tag{35}$$

Under paraxial approximation, we can separate the slowly-varying complex envelope function and a fast-varying spatial exponential factor, considering the field propagating along the z direction and polarized along the x direction, we write

$$\mathbf{E}_0(x, y, z) = \tilde{E}(x, y, z)e^{ik_0 z}\mathbf{n}_x, \tag{36}$$

where $\mathbf{n}_x$ is a unit vector along the x-axis and $k_0 = \omega_0/c$ is the carrier wave vector.

Substituting Eq. (36) into (35), we produce

$$\left(\frac{\partial^2}{\partial x^2} + \frac{\partial^2}{\partial y^2} + \frac{\partial^2}{\partial z^2} + 2ik_0\frac{\partial}{\partial z}\right)\tilde{E}(x, y, z) = 0. \tag{37}$$

Now, since we assumed that the transverse profile changes slowly in the propagation direction (z-axis) in comparison to the phase variation, the second derivative in z is negligible with respect to the first derivative, and thus we obtain the paraxial wave equation as [51]

$$\left(\frac{\partial^2}{\partial x^2} + \frac{\partial^2}{\partial y^2} + 2ik_0\frac{\partial}{\partial z}\right)\tilde{E}(x, y, z) = 0. \tag{38}$$

In terms of the transverse Laplacian operator

$$\Delta_\perp \equiv \frac{\partial^2}{\partial x^2} + \frac{\partial^2}{\partial y^2}, \tag{39}$$

the Eq. (38) takes the form

$$\frac{\partial \tilde{E}(x, y, z)}{\partial z} = \frac{i}{2k_0}\Delta_\perp \tilde{E}(x, y, z), \tag{40}$$

which is a parabolic partial differential equation. As the light field traverses along the z-axis, this equation determines the evolution of the complex envelope function. Now we take the Fourier transformation defined as

$$\mathcal{F}\left[f(x)\right] = \int_{-\infty}^{\infty} f(x)e^{-ikx}\mathrm{d}x, \tag{41}$$

in the transverse dimension on both sides of Eq. (40),

$$\mathcal{F}\left[\frac{\partial \tilde{E}(x, y, z)}{\partial z}\right] = \mathcal{F}\left[\frac{i}{2k_0}\Delta_\perp \tilde{E}(x, y, z)\right], \tag{42}$$

with respect to x and y ($x \to k_x; y \to k_y$) and writing $\mathcal{F}[\tilde{E}(x, y, z)] = \tilde{\varepsilon}(k_x, k_y, z)$, we obtain

$$\frac{\partial \tilde{\varepsilon}(k_x, k_y, z)}{\partial z} = -\frac{i(k_x^2 + k_y^2)}{2k_0}\tilde{\varepsilon}(k_x, k_y, z), \tag{43}$$

with the solution,

$$\tilde{\varepsilon}(k_x, k_y, z) = \tilde{\varepsilon}(k_x, k_y, 0)e^{-iz(k_x^2+k_y^2)/2k_0}. \tag{44}$$

From this, we conclude that paraxial diffraction affects the frequency envelope by introducing a quadratic spatial-spectral phase. Next, we study the group velocity dispersion (GVD) to establish an equivalent equation of light transforming in the temporal domain.

Group velocity dispersion: temporal domain

To understand the *group velocity dispersion* (GVD), we first approximate the total electric field $\mathbf{E}(x, y, z, t)$ in a transparent dispersive medium as a quasi-monochromatic infinite plane wave traveling in the $+z$ direction. We start by writing the wave equation in a transparent dielectric with refractive index n

$$\nabla^2 \mathbf{E}(\mathbf{r}, t) - \frac{n^2}{c^2}\frac{\partial^2 \mathbf{E}(\mathbf{r}, t)}{\partial t^2} = 0. \tag{45}$$

For a plane wave polarized in x direction, $\mathbf{E}(\mathbf{r}, t) = E(z, t)\mathbf{n}_x$, so we write Eq. (45) as

$$\frac{\partial^2}{\partial z^2}E(z, t) - \frac{n^2}{c^2}\frac{\partial^2 E(z, t)}{\partial t^2} = 0. \tag{46}$$

Taking the Fourier transform of $E(z, t)$ with respect to t, we obtain the slowly varying envelope in the frequency domain,

$$E(z, t) = \int \tilde{E}(z, \omega)e^{-i\omega t}\frac{\mathrm{d}\omega}{2\pi}, \tag{47}$$

which upon substitution in Eq. (46) yields us

$$\frac{\partial^2}{\partial z^2}\tilde{E}(z, \omega) + \frac{\omega^2 n^2}{c^2}\tilde{E}(z, \omega) = 0. \tag{48}$$

Again taking the Fourier transform of $\tilde{E}(z, \omega)$ with respect to z, we obtain the field as a function of the wavenumber k and frequency ω,

$$\tilde{E}(z, \omega) = \int \tilde{\tilde{E}}(k, \omega)e^{ikz}\frac{\mathrm{d}k}{2\pi}, \tag{49}$$

which upon substitution in Eq. (48) yields us

$$\left[-k^2+\frac{\omega^2 n^2}{c^2}\right]\tilde{\tilde{E}}(k,\omega)=0, \tag{50}$$

and we arrive at the *dispersion law*: $k=\omega n/c$. The solution of Eq. (50) is

$$\tilde{\tilde{E}}(k,\omega)=\delta(k-\frac{\omega n}{c})\tilde{\tilde{E}}_0(\omega), \tag{51}$$

where $\tilde{\tilde{E}}_0(\omega)$ is a function determined by the initial condition for the field. We substitute in Eq. (49) to obtain

$$\tilde{E}(z,\omega)=\int \delta(k-\frac{\omega n}{c})\tilde{\tilde{E}}_0(\omega)e^{ikz}\frac{\mathrm{d}k}{2\pi}=\frac{1}{2\pi}\tilde{\tilde{E}}_0(\omega)e^{ik(\omega)z}. \tag{52}$$

Substituting the initial condition $\tilde{E}(0,\omega)=\tilde{\tilde{E}}_0(\omega)/2\pi$, we obtain

$$\tilde{E}(z,\omega)=\tilde{E}(0,\omega)e^{ik(\omega)z}. \tag{53}$$

In a dispersive medium, the dispersion law takes form $k(\omega)=n(\omega)\omega/c$, where $n(\omega)$ is a frequency-dependent refractive index of the dielectric medium. Next, the Taylor series expansion of $k(\omega)$ with respect to $\Omega=\omega-\omega_0$, where ω_0 is the central frequency of the field spectrum, limited to the second-order can be accurately expressed as

$$k(\omega)=k_0+k_0'\Omega+\frac{1}{2}k_0''\Omega^2, \tag{54}$$

where the second term $k_0'=(\mathrm{d}k(\omega)/\mathrm{d}\Omega)_{\Omega=0}$ is the inverse of the *group velocity* at the carrier frequency, and the third term $k_0''=(\mathrm{d}^2k(\omega)/\mathrm{d}\Omega^2)_{\Omega=0}$ is the GVD. The approximation of narrowband dispersion consists in limiting the decomposition (54) to the second order in frequency, which is justified for sufficiently narrowband fields.

Now, we substitute Eqs. (53) and (54) into (47) such that,

$$E(z,t)=\int \tilde{E}(0,\omega)e^{ik_0z+ik_0'\Omega z+ik_0''\Omega^2 z/2-i\omega_0 t-i\Omega t}\frac{\mathrm{d}\Omega}{2\pi}. \tag{55}$$

Further, we can simplify Eq. (55) by taking the traveling-wave reference frame, with the *group-delayed time* $\tau=t-t_g$, where, $t_g=k_0'z$ is the *group delay*, and $D=k_0''z$ is the *group delay dispersion* (GDD). Through these, we arrive at

$$E(z,t)=A(z,\tau)e^{ik_0z-i\omega_0 t}, \tag{56}$$

where $A(z,\tau)$ is defined as the *group delayed envelope*,

$$A(z,\tau) = \int \tilde{E}(0,\omega) e^{-i\tau\Omega + ik_0''\Omega^2 z/2} \frac{\mathrm{d}\Omega}{2\pi}. \tag{57}$$

This demonstrates that the narrowband dispersion introduces a quadratic phase to the temporal envelope, similar to the paraxial diffraction. Taking inverse Fourier transform on both sides of Eq. (57) for $z = 0$, we obtain

$$\tilde{A}(0,\Omega) = \tilde{E}(0,\omega_0 + \Omega). \tag{58}$$

where $\tilde{A}(z,\Omega)$ is the temporal Fourier transform of $A(z,t)$.

Substituting Eq. (58) into (57), we arrive at

$$A(z,t) = \int \tilde{A}(0,\omega) e^{-i\tau\Omega + ik_0''\Omega^2 z/2} \frac{\mathrm{d}\Omega}{2\pi}. \tag{59}$$

Now, differentiating Eq. (59) with respect to z gives us the temporal form of the parabolic differential equation which governs the evolution of the slowly varying envelope within a certain distance

$$\frac{\partial A(z,\tau)}{\partial z} = -\frac{ik_0''}{2} \frac{\partial^2 A(z,\tau)}{\partial \tau^2}. \tag{60}$$

which is a one-dimensional parabolic equation similar to Eq. (40).

Thus, we conclude that the GVD and the local curvature of the envelope determine the spreading of the envelope in time. From the equivalence of Eqs. (40) and (60), we summarize the analogs between diffraction and dispersion in Table. 1.

Diffraction	Dispersion
x, y	τ
$-1/k_0$	k_0''
z	z
k_x, k_y	Ω

Table 1: Correspondence between paraxial diffraction and narrowband dispersion

Having established the equivalence between equations guiding the paraxial diffraction and narrowband dispersion of a light field, we now examine the temporal imaging system. The optical imaging systems either spatial or temporal, allow us to form spatial or temporal images respectively. In case of the temporal imaging, we can think of the signal expanding in time τ while experiencing GDD.

1.3 Theory of quantum temporal imaging

In this section, we consider more details of the temporal imaging systems and search for their applications to quantum mechanics. To understand the functioning of the temporal imaging we need to find the temporal equivalent of the conventional lens, which is a *time lens* . We can easily state that the time lens would allow us to provide a quadratic phase modulation in time to the input waveform. Therefore, a temporal imaging system enables us to characterize and manipulate the quantum fields of light in time.

In Section 1.1, we studied how we can use quantum mechanics to quantize a free electromagnetic field. Now, we are going to learn the theory of quantum temporal imaging which searches for manipulations of nonclassical waveforms which preserve their nonclassical properties. There have been several works done on this subject already [9, 34, 36, 44–48], here the authors investigate the general theoretical performance of quantum temporal imaging. The time lens can be implemented using a number of ways like electro-optic phase modulation (EOPM) [15, 18, 19], cross-phase modulation [21, 60], sum-frequency generation (SFG) [22–26], or four-wave mixing (FWM) [27–30].

Single-lens temporal imaging system

In order to work with quantum imaging systems, it is important to study the elements of an ideal temporal imaging system and derive the field transformation by a time lens. We start by defining the effects of dispersions and GDD in the time domain as

$$G_{\text{in}}(\tau) = \frac{e^{i\tau^2/2D_{\text{in}}}}{\sqrt{2\pi i D_{\text{in}}}}, \text{ (input dispersion)} \tag{61a}$$

$$G_{\text{f}}(\tau) = e^{i\tau^2/2D_{\text{f}}}, \text{ (time lens)} \tag{61b}$$

$$G_{\text{out}}(\tau) = \frac{e^{i\tau^2/2D_{\text{out}}}}{\sqrt{2\pi i D_{\text{out}}}}. \text{ (output dispersion)} \tag{61c}$$

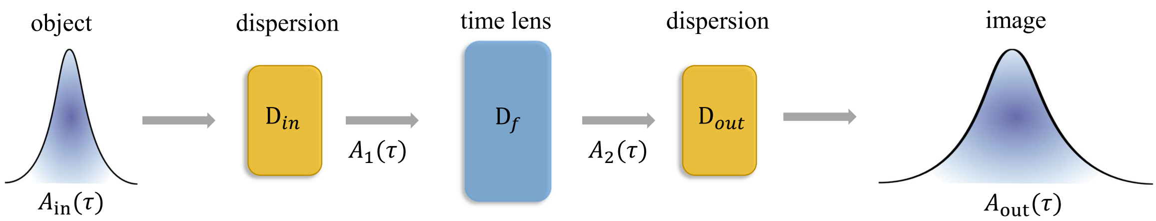

Figure 2: Pulse transformation in a single-lens temporal imaging system. The pulse passes through the input dispersive medium, time lens, and the output dispersive medium. The resulting output pulse is a magnified version of the input pulse.

We begin with considering an initial envelope function $A_{\text{in}}(\tau)$ propagating through a system as shown in Figure 2. This envelope function is our object and we are interested in analyzing the image it can form by a time lens. Now, $A_{\text{in}}(\tau)$ after propagating through the first dispersive medium becomes,

$$A_1(\tau) = \int_{-\infty}^{\infty} A_{\rm in}(\tau')G_{\rm in}(\tau - \tau')\mathrm{d}\tau'. \tag{62}$$

This equation describes a unitary transformation of the quantum field operators in time evolution because $\int_{-\infty}^{\infty} G_{\rm in}(\tau - \tau'')G^*_{\rm in}(\tau' - \tau'')\mathrm{d}\tau'' = \delta(\tau - \tau')$, wherefrom follows the conservation of the commutation relation.

Similarly, the field after the time lens and the output dispersion transforms respectively into

$$A_2(\tau) = A_1(\tau)G_{\rm f}(\tau), \tag{63a}$$
$$A_{\rm out}(\tau) = \int_{-\infty}^{\infty} A_2(\tau')G_{\rm out}(\tau - \tau')\mathrm{d}\tau'. \tag{63b}$$

Expressing $A_{\rm out}$ via $A_{\rm in}$ [24], we obtain that under the *single-lens temporal imaging condition* or the time lens condition ,

$$\frac{1}{D_{\rm in}} + \frac{1}{D_{\rm out}} = \frac{1}{D_{\rm f}}. \tag{64}$$

the field transformation is a simple scaling in time

$$A_{\rm out}(\tau) = \frac{1}{\sqrt{M}} e^{i\tau^2/2MD_{\rm f}} A_{\rm in}(\tau/M), \tag{65}$$

where

$$M = -\frac{D_{\rm out}}{D_{\rm in}}, \tag{66}$$

is the temporal magnification.

Equation (64) reminds us of the well-known imaging condition in the spatial domain for a thin-lens, which reads $1/d_{\rm in} + 1/d_{\rm out} = 1/f$, where the distances from the lens to the object and image are $d_{\rm in,out}$ and the focal length is f. If this condition is satisfied in space for a conventional imaging system, then the output envelope profile $E(x/M)$ is the scaled form of the input envelope $E(x)$, where the *magnification* is expressed as $M = -d_{\rm out}/d_{\rm in}$.

One important thing to note here is that the time lens always imparts the residual phase chirp $e^{i\tau^2/2MD_{\rm f}}$. Now, we will explore the functioning of the time lens by taking two examples.

Electro-Optic Phase Modulation (EOPM) based time lens

The creation of a time lens is most effectively achieved by employing an Electro-Optic Phase Modulator (EOPM) [61] driven by a quadratic voltage. The initial experimental implementations of time lens systems were based on this particular methodology. In practical applications, the Radio Frequency (RF) signal driving the phase modulator adopts a sinusoidal nature, exhibiting local quadratic behavior near its minima and maxima. As shown in Figure 3, when the input field duration is shorter than the temporal aperture $\Delta T = 1/\omega_m$, the cosine can be approximated by a parabola

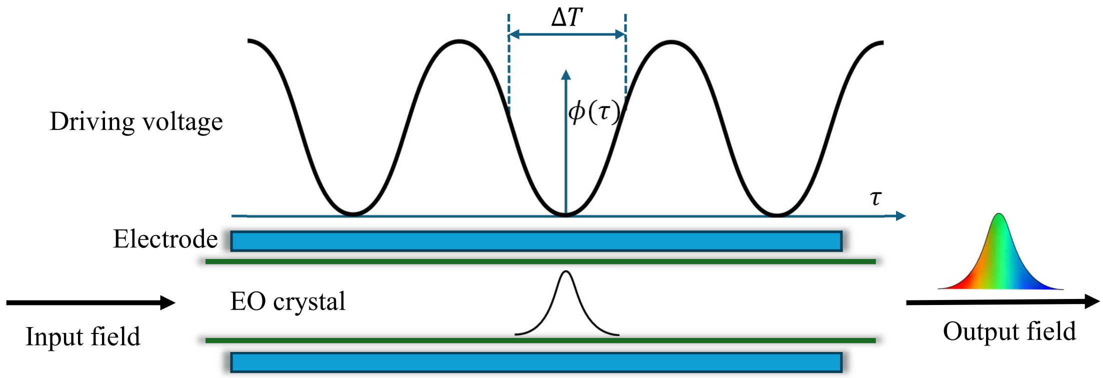

Figure 3: Schematic representation of a temporal imaging system with an electro-optic phase modulation (EOPM)-based time lens. The input field propagates in the same direction through the electro-optic (EO) crystal and interacts with the radio wave through the electro-optic effect.

$$\phi_{RF}(t) = -\left(\frac{\pi V_m}{V_\pi}\right)\cos(\omega_m t) \approx -\left(\frac{\pi V_m}{V_\pi}\right)\left(1 - \frac{\omega_m^2 t^2}{2}\right), \tag{67}$$

where V_m and ω_m denote the amplitude and frequency, respectively, of the modulating voltage, and V_π represents the voltage level required for the modulator to induce a phase shift equal to π. It is evident from comparing Eq. (67) to Eq. (61b) that the absolute value of the time lens focal Group Delay Dispersion (GDD) is given by [13]

$$D_f^{\mathrm{EOPM}} = \frac{V_\pi}{\pi V_m \omega_m^2}. \tag{68}$$

Sum-Frequency Generation (SFG) based time lens

In this subsection, we use the nonlinear process SFG, in which a strong pump wave of frequency ω_p interacts with a signal wave of frequency ω_s to produce an idler wave of frequency ω_i such that $\omega_i = \omega_p + \omega_s$. This lets us identify the index $\mu = s, i, p$ with the signal, idler, or pump respectively.

We start by writing the positive-frequency part of the field operator as

$$\hat{E}_\mu^{(+)}(t, z) = \hat{A}_\mu(\tau, z)e^{i(k_0 z - \omega_0 t)}, \tag{69}$$

where the field envelope $\hat{A}_\mu(\tau, z)$ is a function of the group-delayed time $\tau = t - k_0' z$.

Parametric processes, such as sum-frequency generation (SFG), involve a pump wave converting the wavelength of the signal under test into a new wavelength (idler). The resulting output field $\hat{A}_{out}(\tau)$ is a result of the interaction of the pump and input field $\hat{A}_{in}(\tau)$. By engineering the pump pulse to possess a temporally quadratic phase profile within a specific time window, the output field becomes proportional to the input field with an added quadratic phase. Achieving a pump pulse with a quadratic phase profile, corresponding to a linear frequency chirp is feasible by directing a short Gaussian pulse through a highly dispersive path. Figure 4 illustrates the concept of a parametric time lens through the SFG process. In this scenario, the idler frequency $\omega_i = \omega_p + \omega_s$ is related to the optical frequencies of the pump ω_p and signal ω_s beams.

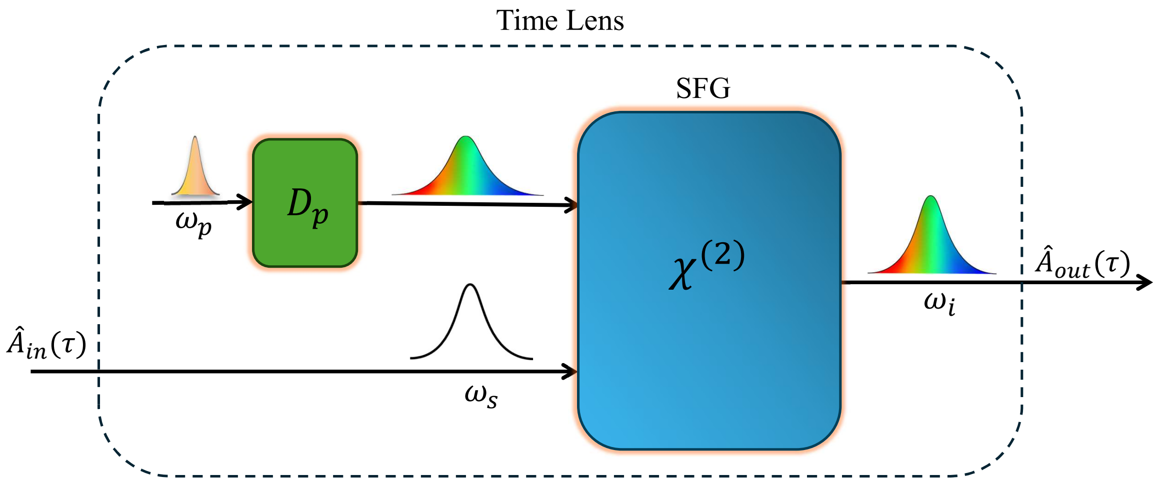

Figure 4: Schematic representation of a sum-frequency-generation (SFG)-based time lens. The pulse travels through the dispersive medium with GDD D_p and is stretched and chirped. Then it interacts with the input field in the non-linear crystal with non-linear susceptibility $\chi^{(2)}$. The output field is a product of the pump and input field as a result of the SFG parametric process.

Considering a short pump pulse with a bandwidth $\Delta\Omega_p$ generated from a femtosecond pulsed laser and passed through a dispersive component with a total Group Delay Dispersion (GDD) of D_p (neglecting higher-order dispersion terms), the temporal Fraunhofer limit condition $\Delta\Omega_p^2|D_p| \gg 1$ ensures that the phase $\phi_p(\tau)$ of the pump field is a quadratic function of time (see Appendix A),

$$\phi_p(\tau) = -\frac{\tau^2}{2D_p}. \tag{70}$$

The interaction between the pump and the signal happens in the nonlinear medium with the second-order nonlinear optical susceptibility. The general evolution of the signal and idler fields inside the nonlinear medium under the assumption that all the waves are traveling at the same group velocity reads [44],

$$\frac{\partial \hat{A}_s(\tau, z)}{\partial z} = gA_p^*(\tau)\hat{A}_i(\tau, z)e^{i\Delta kz}, \tag{71a}$$

$$\frac{\partial \hat{A}_i(\tau, z)}{\partial z} = gA_p(\tau)\hat{A}_s(\tau, z)e^{-i\Delta kz}. \tag{71b}$$

Here, g is the nonlinear coupling constant, $A_p(\tau) = |A_p(\tau)|e^{i\phi_p(\tau)}$ is the pump pulse, and $\Delta k = k_i - k_s - k_p$ is the phase mismatch between the signal, idler, and the pump wavevectors. The solutions of the Eqs. (71a) and (71b) in this scenario at zero phase mismatch $\Delta k = 0$, describe the unitary transformation from the point of time lens input z_1 to the output z_2 as

$$\hat{A}_s(\tau, z_2) = \cos[g|A_p(\tau)|(z_2 - z_1)]\hat{A}_s(\tau, z_1) - \sin[g|A_p(\tau)|(z_2 - z_1)]e^{-i\phi_p(\tau)}\hat{A}_i(\tau, z_1), \tag{72a}$$

$$\hat{A}_i(\tau, z_2) = \sin[g|A_p(\tau)|(z_2 - z_1)]e^{i\phi_p(\tau)}\hat{A}_s(\tau, z_1) + \cos[g|A_p(\tau)|(z_2 - z_1)]\hat{A}_i(\tau, z_1). \tag{72b}$$

The output field $\hat{A}_i(\tau, z_2)$ is a sum of the phase-modulated input field and a vacuum fluctuation $\hat{A}_i(\tau, z_1)$. To eliminate the vacuum fluctuations, we set $g|A_p(\tau)|(z_2 - z_1) = \pi/2$ since in the experimental conditions, the *conversion efficiency* $|\sin[g|A_p(\tau)|(z_2 - z_1)]|^2 = 1$, which should be satisfied for times within the *temporal aperture* ΔT. Under this condition, Eq. (72b) takes the form

$$\hat{A}_\mathrm{i}(\tau, z_2) = e^{i\phi_p(\tau)}\hat{A}_\mathrm{s}(\tau, z_1). \tag{73}$$

Comparing Eqs. (73) and (70) with (61b), we arrive at

$$D_f^{\mathrm{SFG}} = -D_p. \tag{74}$$

Thus, a time lens can be realized by a SFG process with the focal GDD determined by the GDD experienced by the pump pulse taken with the opposite sign.

1.4 Photon statistics

We now study the statistics of the quantum states of light in this section and consider the representation of the photon states and their properties. Additionally, we learn about interference and photodetection. The idea behind studying quantum optics is to view a light beam not as a classical wave but as a stream of photons. The characterization and manipulation of photons will be performed in the upcoming chapters, so it's critical to comprehend the underlying theory. What separates a nonclassical light from a classical light is the question that needs to be answered, and nonclassical characteristics like antibunching or sub-Poissonian statistics do just that. In the next subsection, we briefly analyze the theory of the Hanbury Brown-Twiss experiment and the phenomenon of antibunched light. Next, we study sub-Poissonian photon statistics followed by the quantum interference of photons.

Degree of second-order coherence

In this subsection, we look at a different way of quantifying light according to the normalized second-order correlation function $g^{(2)}(\tau)$. We introduce this function mathematically as

$$g^{(2)}(\tau) = \frac{\langle : \hat{I}(t)\hat{I}(t+\tau) : \rangle}{\langle \hat{I}(t) \rangle^2}, \tag{75}$$

where $\hat{I}(t) = \hat{a}^\dagger(t)\hat{a}(t)$ is the *photon flux* operator and notation $::$ stands for *normal* and *time* ordering [62]. The second-order correlation function is also known as *degree of second-order temporal coherence* [63] and it quantifies intensity fluctuations.

The measurement of the second-order correlation function, $g^{(2)}(\tau)$, can be carried out through a photocurrent correlation experiment, illustrated in Figure 5. A semitransparent mirror splits the primary electromagnetic wave into two components, each detected by independent photodetectors D_1 and D_2. After introducing a time delay τ into one of the detectors, the photocurrents from both detectors are multiplied.

The study of such correlations was first performed by Hanbury Brown and Twiss in Ref. [64] with subsequent more detailed accounts in Ref. [65] and [66]. The original experiments constituted the study of thermal light from the stars and galaxies and allowed the researchers to determine the angular size of stars not measurable by conventional astrometry. There have been works that contributed to the translation of the intensity correlations to the quantum field correlations [67–69].

We rewrite Eq. (75) as

$$g^{(2)}(\tau) = \frac{\langle : \hat{a}^\dagger(t)\hat{a}(t)\hat{a}^\dagger(t+\tau)\hat{a}(t+\tau) : \rangle}{\langle \hat{a}^\dagger(t)\hat{a}(t) \rangle^2}. \tag{76}$$

In other words, $g^{(2)}(\tau)$ is proportional to the conditional probability of detecting a second photon at time $t+\tau$ on the condition that the first photon was detected at time t. Evaluating this function gives us properties of the input field and classifies the light source as described in Table 2. We describe below the classical and nonclassical features of the light field through the $g^{(2)}(\tau)$ function.

Photon bunching. Classical effect $g^{(2)}(0) \geq g^{(2)}(\tau)$:

We observe that for short-time delays τ the conditional probability of detecting the second photon is higher than for long delays when these two events become independent and this phenomenon is called photon bunching. Bunching's typical time scale is related to intensity correlation time in thermal light, disappearing in coherent light without classical intensity fluctuations. For a fully coherent field, the photon annihilation and creation

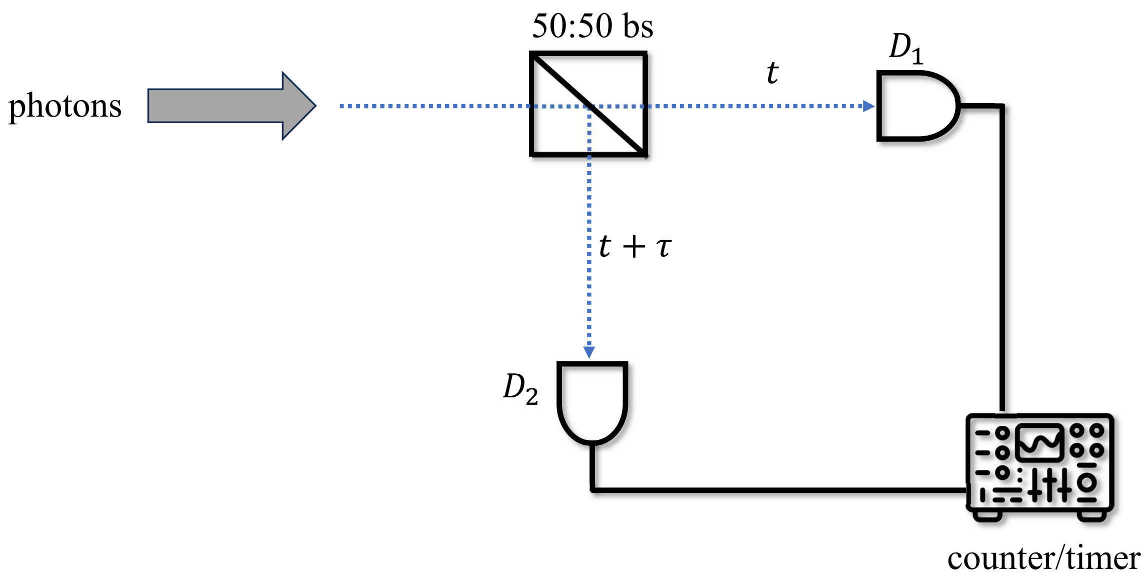

Figure 5: Hanbury Brown-Twiss experiment in the quantum regime. A beam of photons impinges upon a 50:50 beamsplitter. The detectors register the photon counts and the time elapsed between each count.

operators $\hat{a}(t)$ and $\hat{a}^{\dagger}(t)$ transition to stochastic c numbers $\alpha(t)$ and $\alpha^*(t)$. The correlation function $g^{(2)}(\tau)$ in Eq. (76) is expressed as $g^{(2)}(\tau) = \langle J(t)J(t+\tau)\rangle / \langle J(t)\rangle^2$, where $J(t) = |\alpha(t)|^2$ denotes the stochastic classical light intensity. For a stationary random process $J(t)$, this relationship follows from the Schwarz inequality, $g^{(2)}(0) \geq g^{(2)}(\tau)$, i.e., $g^{(2)}(\tau)$ has its absolute maximum at zero time delay, $\tau = 0$.

Light source	Property	Comment
Classical light	$g^{(2)}(0) \geq 1$	$g^{(2)}(\infty) = 1$ for any field
	$g^{(2)}(0) \geq g^{(2)}(\tau)$	
Perfectly coherent light	$g^{(2)}(\tau) = 1$	applies for all τ
Antibunched light	$g^{(2)}(0) < 1$	no classical description
	$g^{(2)}(0) < g^{(2)}(\tau)$	

Table 2: Properties of the $g^{(2)}(\tau)$ function

Photon antibunching. Nonclassical effect $g^{(2)}(0) < g^{(2)}(\tau)$:

Photon antibunching contradicts the bunching inequality, indicating that light fields exhibiting antibunching cannot be adequately described by random c numbers. The possibility of an opposite phenomenon to bunching arises when the conditional probability of the second photodetection at short-time delays (τ) is lower than for longer delays. A classical illustration demonstrating the existence of antibunching is found in the phenomenon of *resonance fluorescence* of a single atom driven by an external monochromatic light field [68]. Photon emission during an atom's transition from its excited state $|1\rangle$ to the ground state $|0\rangle$ is influenced by the excited state's population. After the first photon emission, the probability of an immediate second emission is zero. A time delay is necessary for the atom to return to the excited state $|1\rangle$ before emitting another photon. This leads to antibunching, with a lower probability of detecting a second photon for short-time delays compared to longer delays. Antibunching is a nonclassical phenomenon that cannot be explained in the framework of classical electrodynamics.

Sub-Poissonian photon statistics

Sub-Poissonian photon statistics represent another nonclassical effect. In contrast to the Poissonian photon statistics of a coherent light state $|\alpha\rangle$, where the probability of finding n photons follows a Poisson distribution, sub-Poissonian statistics deviate from this classical behavior. Poissonian distribution describes the photon statistics and is given by

$$\mathcal{P}(n) = |\langle n|\alpha\rangle|^2 = \frac{\langle n\rangle^n}{n!} e^{-\langle n\rangle}, \tag{77}$$

where $\langle n\rangle = |\alpha|^2$ is the average photon number equal to the intensity of the classical field. We introduce the dispersion of the photon number $\langle(\Delta n)^2\rangle = \langle n\rangle$ for a Poisson distribution, we characterize the photon statistics for an arbitrary single-mode quantum field using Mandel's Q parameter [70],

$$Q = \frac{\langle(\Delta n)^2\rangle - \langle n\rangle}{\langle n\rangle}. \tag{78}$$

A statistics is called super-Poissonian if $Q > 0$, and sub-Poissonian if $Q < 0$. For classical states, the photon statistics are either super-Poissonian or Poissonian (in coherent states), leading to a non-negative Mandel's Q parameter ($Q \geq 0$). Nonclassical states, such as Fock states with a definite photon number $\langle(\Delta n)^2\rangle = 0$, exhibit sub-Poissonian statistics, allowing Q to take on negative values, with the extreme being $Q = -1$. For a single-mode field, we relate the correlation function $g^{(2)}(\tau)$ with the dispersion of the photon number in the following way,

$$g^{(2)}(0) - g^{(2)}(\infty) = \frac{\langle(\Delta n)^2\rangle - \langle n\rangle}{\langle n\rangle^2}. \tag{79}$$

Hong-Ou-Mandel interference

Next, we study the interference of light in the quantum picture. The authors Hong, Ou, and Mandel in Ref. [71] presented for the first time an approach to investigating the two-photon interference effect. The effect occurs when two indistinguishable photons impinge upon a 50:50 beam splitter (BS), one in each port, then their temporal overlap being perfect, they exit the BS together in the same but random output mode. This means that the probability of having a coincidence event at each of the outputs is zero. This effect finds its applications in detecting the identicality of the input photons and shows up in practical implementations of quantum technologies. When we use the word indistinguishability or identicality of two photons, we denote their equality in properties like polarization, spectral mode, temporal mode, arrival time, or transverse spatial mode.

Let us consider two photons incident on BS modes a and b respectively as shown in Figure 6. The bosonic creation operators $\hat{a}^\dagger_{a,\mu}$ and $\hat{a}^\dagger_{b,\nu}$ identify the BS modes of the respective photons in addition to other properties (labeled by μ and ν) determining their distinguishability. The combined two-photon state at the input port reads

$$|\psi_{\rm in}\rangle_{ab} = \hat{a}^\dagger_{a,\mu}\hat{a}^\dagger_{b,\nu}|0\rangle_{ab}, \tag{80}$$

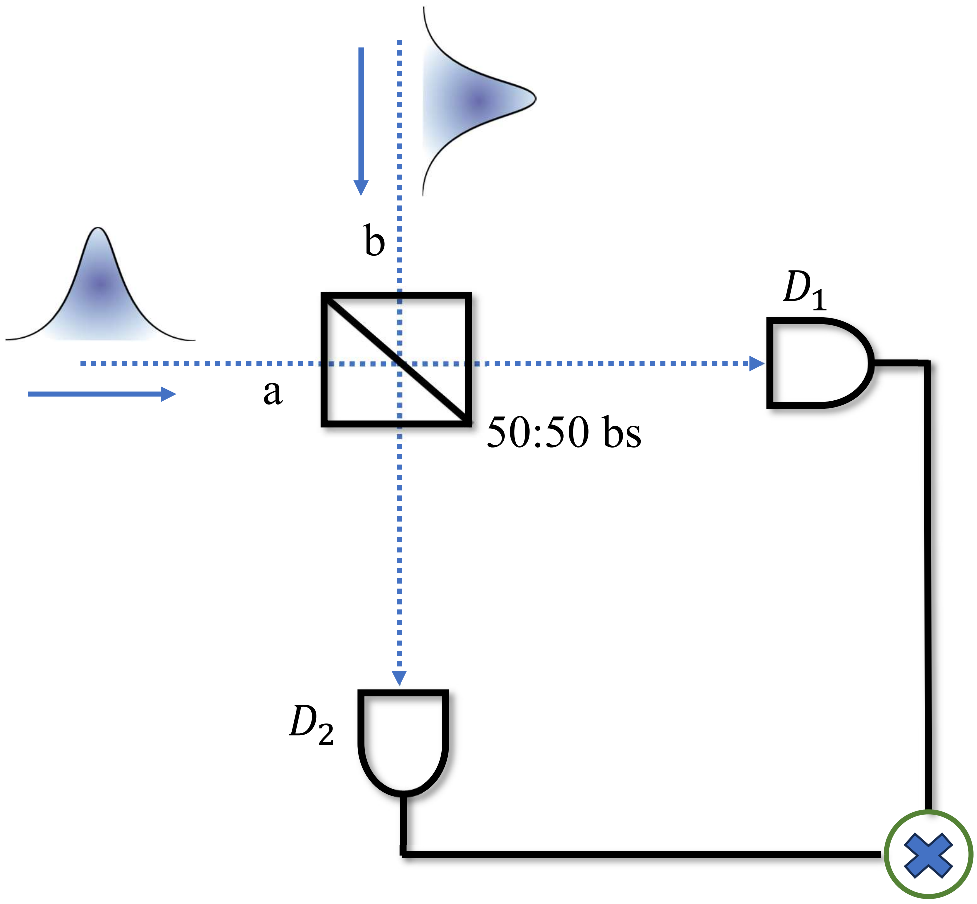

Figure 6: General HOM interference scheme with single photons. Two single photons impinge on a 50:50 beam splitter and the detectors register the incidents. Identical photons interfere and a perfect co-incidence is observed.

where $|0\rangle$ is the vacuum state or the ground state. This state evolves with the interference in the BS with reflectivity $\eta = 1/2$ and follows a unitary transformation. The combined two-photon state at the output of the BS takes the form [72],

$$|\psi_{\rm out}\rangle_{ab} = \frac{1}{2}\left(\hat{a}^\dagger_{a,\mu}\hat{a}^\dagger_{a,\nu} + \hat{a}^\dagger_{a,\nu}\hat{a}^\dagger_{b,\mu} - \hat{a}^\dagger_{a,\mu}\hat{a}^\dagger_{b,\nu} - \hat{a}^\dagger_{b,\mu}\hat{a}^\dagger_{b,\nu}\right)|0\rangle_{ab}. \tag{81}$$

Now, it is simple to state that for $\mu \neq \nu$, the photons are distinguishable and for $\mu = \nu$, the photons are indistinguishable or identical. In the case of distinguishable photons, mixed state output Eq. (81) stays the same but for identical photons, using Eqs. (18a) and (18b), the output state is formulated as

$$|\psi_{\text{out}}\rangle_{ab,\mu=\nu} = \frac{1}{2}\left(\hat{a}^{\dagger}_{a,\mu}\hat{a}^{\dagger}_{a,\mu} - \hat{a}^{\dagger}_{b,\mu}\hat{a}^{\dagger}_{b,\mu}\right)|0\rangle_{ab}. \tag{82}$$

This demonstrates that the photons exit from the same but random output port if they are identical and this effect is famously known as the *Hong-Ou-Mandel* (HOM) effect . In the experimental signature, the HOM effect is observed using photodetectors, which monitor the coincidence rate of the detectors. When the indistinguishable input photons overlap perfectly in time, the normalized coincidence rate drops to zero, famously known as the HOM dip (see Figure 7). On the contrary, this dip completely disappears if the photons are distinguishable. Another important parameter of the HOM interferometer is the interference visibility which is the probability of destructive interference of the photons.

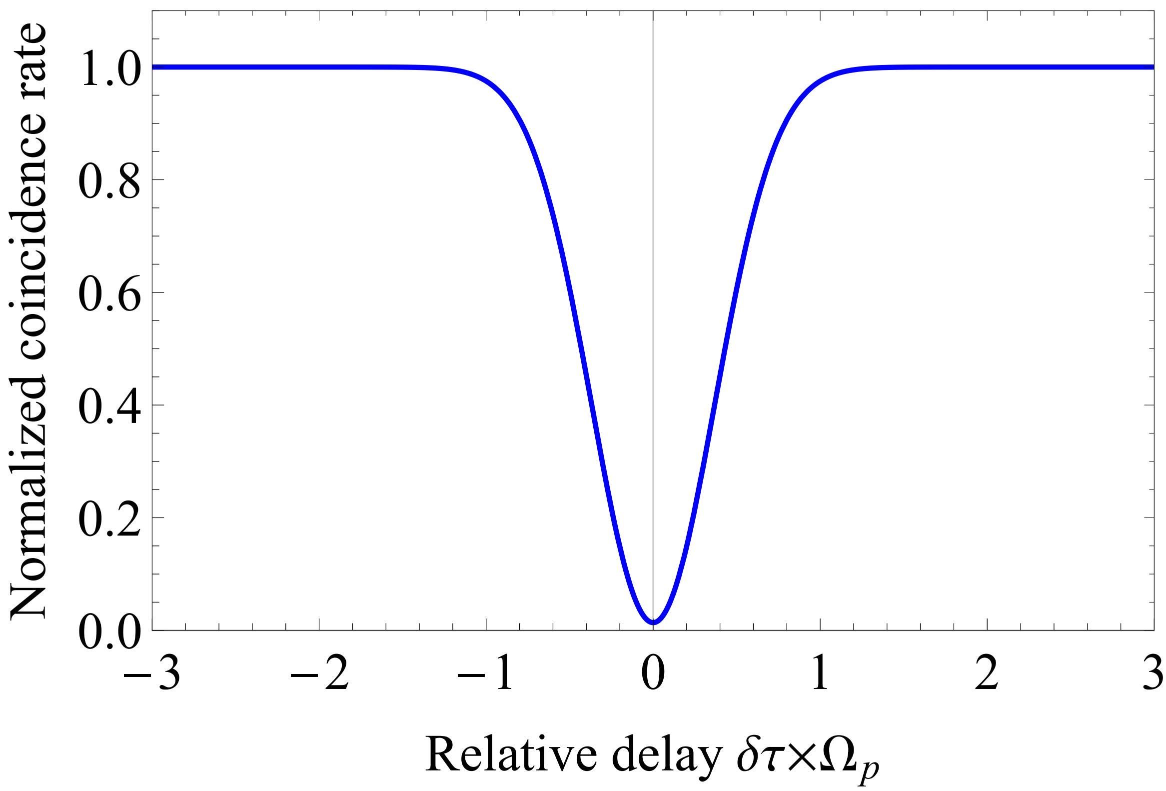

Figure 7: The HOM dip of normalized coincident count rate in the detectors plotted as a function of the relative delay between single-photon wave packets. The relative delay is measured in the units of Ω_p which denotes the pump bandwidth in the case where the photons are produced by parametric downconversion as in Ref. [71].

1.5 Summary

This chapter delves into the elements of quantum optics, laying the preliminaries for the subsequent studies of manipulating light quantum fields through temporal imaging systems. An essential aspect is comprehending the field quantization, which enables the distinction between classical and quantum fields. This leads us to quantum states of the light and before exploring quantum optical states, it's crucial to understand nonclassical light examples like Fock states and coherent states, establishing a strong foundation for a deeper understanding. Fock states represent discrete photon number states, while coherent states are superpositions of different photon number states, exhibiting classical-like behavior in quantum systems.

This thesis employs temporal imaging systems to characterize and manipulate photons, exploring the ability to stretch or compress pulses in time, similar to what is conventionally performed in space. We begin by understanding the concept of space-time duality in optics, establishing a mathematical equivalence between equations describing paraxial diffraction in space and narrowband dispersion in time. This leads us to the theory of a "time lens", the temporal counterpart of a spatial lens, capable of manipulating the waves in time. A quantum theoretic perspective on this phenomenon directs us to the principles of quantum temporal imaging that investigates the potentialities of manipulating the nonclassical waveforms that preserve their nonclassical properties.

Lastly, we study the representation and properties of photon states. This involves interference, photodetection, and a fundamental shift in perspective—treating a light beam not as a classical wave but as a flow of photons. The distinguishing factor between classical and nonclassical light lies in characteristics such as antibunching or sub-Poissonian statistics, revealing the essence of nonclassicality. In the upcoming chapter, we will examine the potential of observing the quantum interference of entangled photon pairs through the utilization of a time lens.

Chapter 2

Temporal imaging to observe quantum interference

Each Photon then interferes only with itself.

– Paul Dirac

This chapter explores the use of quantum temporal imaging on light generated in frequency-degenerate type-II spontaneous parametric down-conversion (SPDC) with a pulsed broadband source [73–75]. The study reveals that the temporal and spectral properties of down-converted photons can differ significantly with a pulsed pump, impacting their indistinguishability and Hong-Ou-Mandel interference visibility. To address this, we propose using a time lens instead of a spectral filter, achieving unit visibility in Hong-Ou-Mandel interferometry and restoring perfect indistinguishability while preserving entanglement. This approach is nondestructive and holds relevance for applications like boson samplers [76, 77] and quantum networks [78–80] requiring indistinguishable and disentangled single photons.

In our approach, we take a more realistic stance on the time lens compared to common literature practices. Instead of using a local time in a reference frame with the group velocity, we employ the absolute time in the laboratory reference frame. This method allows for accurate evaluation of time delays in the interferometric scheme used to observe the Hong-Ou-Mandel effect. We clarify the importance of synchronization between the pulsed photon-pair source and the time lens, examining how the precision of this synchronization affects the visibility of the Hong-Ou-Mandel interference.

The chapter is structured as follows: In Section 2.1, we detail the SPDC process with a pulsed broadband pump, providing spectra, and average intensities of the ordinary and extraordinary waves. In Section 2.2 we describe the time lens, the time delays in the interferometric scheme, and the theory of coincidence detection. Section 2.3 explicitly evaluates the coincidence counting rate in the Hong-Ou-Mandel interferometer, studying visibility as a function of various physical parameters. Section 2.4 studies the impact of perfect and imperfect synchronizations in our scheme.

2.1 Spontaneous parametric downconversion

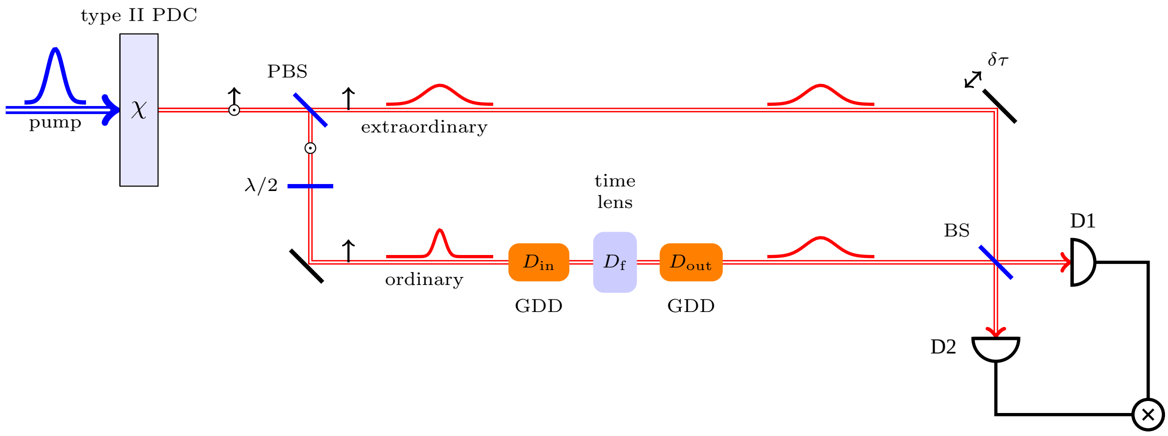

Figure 8: Scheme for generation of photon pairs and observation of their second-order interference. A pump pulse impinges on a nonlinear crystal cut for type-II PDC. Two subharmonic pulses appear as ordinary and extraordinary waves in the crystal. The pump is removed, while two subharmonic pulses are separated by a polarized beam splitter (PBS). Polarization of the ordinary pulse is rotated by a half waveplate. Subsequently, the ordinary pulse passes through a temporal imaging system, composed of an input dispersive medium, a time lens, and an output dispersive medium. The delay of the extraordinary pulse $\delta\tau$ is controlled by a delay line. The pulses interfere at a beam splitter (BS) and are detected by single-photon detectors D1 and D2. A coincidence is registered, if both detectors fire in the same excitation cycle.

Figure 8 illustrates the scheme for generating photon pairs and observing their second-order interference. The setup is divided into distinct components, each described individually below. Notably, the quantum description of the field transformation in each optical element is performed in the Heisenberg picture, deviating from the conventional Schrödinger picture typically used in similar schemes [71, 73, 74, 81–83]. This choice is motivated by the development of the time-lens formalism in the Heisenberg picture [45, 46].

Quantum field generation and evolution

The model describing single-pass pulsed parametric downconversion (PDC) in a $\chi^{(2)}$ nonlinear crystal within the Heisenberg picture is developed in various works, including Refs. [84–90]. In this context, we adopt its single-spatial-dimension version. The system involves a crystal slab of length L, extending infinitely in the transverse directions, and is cut for type-II collinear phase matching. The x axis represents the direction of pump-beam propagation, and the z axis is chosen so that the optical axis (or axes) of the crystal lies (lie) in the xz plane.

The pump is a planar wave polarized along either the y or z direction. In the time domain, it takes the form of a Gaussian transform-limited pulse, with its maximum at the position $x = 0$ during the time $t = t_0$. Its central frequency is denoted by ω_p. Treated as an undepleted deterministic wave, the pump is described by a c-number function of space and time coordinates. The positive frequency part of the pump field (in photon flux units) can be represented as

$$E_p^{(+)}(t, x) = \int \alpha(\Omega) e^{ik_p(\Omega)x - i(\omega_p+\Omega)t} \frac{d\Omega}{2\pi}, \tag{83}$$

where Ω represents the frequency detuning from the central frequency, and the integration limits can be extended to infinity. The pump spectral amplitude $\alpha(\Omega)$ is nonzero only within a limited band and does not depend on x since the pump is undepleted. Variations of the pump wave in the longitudinal direction are determined by the wave-vector $k_p(\Omega) = n_p(\omega_p + \Omega)(\omega_p + \Omega)/c$, where $n_p(\omega)$ is the refractive index corresponding to the polarization of the pump, and c is the speed of light in a vacuum.

We assume the pump pulse to be a Gaussian pulse with a transform-limited full width at half maximum (FWHM) of τ_p, given by

$$E_p^{(+)}(t, 0) = E_0 e^{-(t-t_0)^2/4\sigma_t^2 - i\omega_p t}, \tag{84}$$

where $\tau_p = 2\sqrt{2\ln 2}\sigma_t$ and E_0 is the peak amplitude. By combining this equation with Eq. (83), we obtain

$$\alpha(\Omega) = E_0 \frac{\sqrt{\pi}}{\Omega_p} e^{-\Omega^2/4\Omega_p^2 + i\Omega t_0}, \tag{85}$$

where $\Omega_p = 1/(2\sigma_t)$. The condition of being at the transform limit implies that the time–bandwidth product is at its minimum and indicates the absence of chirp.

Due to the nonlinear transformation of the pump field in the crystal, a subharmonic field emerges. In the case of frequency-degenerate type-II phase matching, considered here, two subharmonic waves with the central frequency $\omega_0 = \omega_p/2$ arise. These waves are polarized in the y (ordinary wave) and z (extraordinary wave) directions. Within the framework of quantum theory, these waves are described by Heisenberg operators. The positive frequency part of the Heisenberg field operator (in photon flux units) can be expressed as a Fourier integral,

$$\hat{E}_\mu^{(+)}(t, x) = \int \epsilon_\mu(\Omega, x) e^{ik_\mu(\Omega)x - i(\omega_0+\Omega)t} \frac{d\Omega}{2\pi}, \tag{86}$$

where $\epsilon_\mu(\Omega, x)$ is the annihilation operator of a photon at position x with the frequency $\omega_0 + \Omega$ and polarization along the y axis for the ordinary ($\mu = o$) wave or along the z axis for the extraordinary ($\mu = e$) one. The wave vector is denoted by $k_\mu(\Omega) = n_\mu(\omega_0 + \Omega)(\omega_0 + \Omega)/c$, where $n_\mu(\omega)$ is the refractive index corresponding to the polarization μ.

The evolution of the annihilation operator along the crystal is governed by the spatial Heisenberg equation [91],

$$\frac{d}{dx}\epsilon_\mu(\Omega, x) = \frac{i}{\hbar}\left[\epsilon_\mu(\Omega, x), G(x)\right], \tag{87}$$

where the spatial Hamiltonian $G(x)$ is determined by the momentum transferred through the plane x [92] and can be expressed as

$$G(x) = \chi \int_{-\infty}^{+\infty} E_p^{(-)}(t,x) E_o^{(+)}(t,x) E_e^{(+)}(t,x) dt + \text{H.c.}, \tag{88}$$

where χ is the nonlinear coupling constant, and $E_p^{(-)}(t,x) = E_p^{(+)*}(t,x)$ represents the negative-frequency part of the field. Substituting Eqs. (83), (86), into (88) and applying the properties of the delta functions, we obtain

$$G(x) = \chi \int\int \alpha(\Omega+\Omega')\epsilon_o^\dagger(x,\Omega)\epsilon_e^\dagger(x,\Omega')e^{i\Delta(\Omega,\Omega')x}\frac{\mathrm{d}\Omega}{2\pi}\frac{\mathrm{d}\Omega'}{2\pi} + H.c. \tag{89}$$

Here

$$\Delta(\Omega,\Omega') = k_p(\Omega+\Omega') - k_o(\Omega) - k_e(\Omega') \tag{90}$$

is the phase mismatch for the three interacting waves. Substituting Eq. (89) into (87), we arrive at

$$\frac{d}{dx}\epsilon_\mu(\Omega,x) = \kappa \int\int \alpha(\Omega'+\Omega'')\left[\epsilon_\mu(x,\Omega), \epsilon_o^\dagger(x,\Omega')\epsilon_e^\dagger(x,\Omega'')\right] e^{i\Delta(\Omega,\Omega')x}\mathrm{d}\Omega'\mathrm{d}\Omega'', \tag{91}$$

where $\kappa = i\chi/2\pi\hbar$ is the new coupling constant. Now, we use the canonical equal-space commutation relations [92, 93]

$$\left[\epsilon_\mu(\Omega,x), \epsilon_\nu^\dagger(\Omega',x)\right] = 2\pi\delta_{\mu\nu}\delta(\Omega-\Omega') \tag{92}$$

in Eq. (91) and obtain the spatial evolution equations

$$\frac{d\epsilon_o(\Omega,x)}{dx} = \kappa \int \alpha(\Omega+\Omega')\epsilon_e^\dagger(\Omega',x)e^{i\Delta(\Omega,\Omega')x}d\Omega', \tag{93a}$$

$$\frac{d\epsilon_e(\Omega,x)}{dx} = \kappa \int \alpha(\Omega+\Omega')\epsilon_o^\dagger(\Omega',x)e^{i\Delta(\Omega',\Omega)x}d\Omega'. \tag{93b}$$

In the low-gain regime, characterized by a sufficiently small pump amplitude, we can solve Eqs. (93a) and (93b) perturbatively. By substituting $\epsilon_\mu^\dagger(\Omega',x) \to \epsilon_\mu^\dagger(\Omega',0)$ under the integral, we obtain the fields at the crystal output,

$$\epsilon_o(\Omega,L) = \epsilon_o(\Omega,0) + \kappa L \int \alpha(\Omega+\Omega')\epsilon_e^\dagger(\Omega',0)\Phi(\Omega,\Omega')d\Omega', \tag{94a}$$

$$\epsilon_e(\Omega,L) = \epsilon_e(\Omega,0) + \kappa L \int \alpha(\Omega+\Omega')\epsilon_o^\dagger(\Omega',0)\Phi(\Omega',\Omega)d\Omega', \tag{94b}$$

where L represents the crystal length, and

$$\Phi(\Omega,\Omega') = e^{i\Delta(\Omega,\Omega')L/2}\mathrm{sinc}[\Delta(\Omega,\Omega')L/2] \tag{95}$$

is the phase-matching function .

By substituting these solutions into Eq. (86), we derive the field transformation from the crystal input face to its output face,

$$\hat{E}^{(+)}_{o,e}(t,L) = \int \left[\epsilon_{o,e}(\Omega,0) + \sigma L \int \alpha(\Omega+\Omega')\epsilon^{\dagger}_{e,o}(\Omega',0)e^{i\Delta(\Omega,\Omega')\frac{L}{2}}\,\mathrm{sinc}\left(\Delta(\Omega,\Omega')\frac{L}{2}\right)\mathrm{d}\Omega'\right] \times e^{ik_\mu(\Omega)L - i(\omega_0+\Omega)t}\frac{\mathrm{d}\Omega}{2\pi}. \tag{96}$$

To represent this transformation concisely, we introduce the envelopes of the ordinary wave at the crystal input and output faces as $A_0(t) = \hat{E}^{(+)}_o(t,0)e^{i\omega_0 t}$ and $A_1(t) = \hat{E}^{(+)}_o(t,L)e^{i(\omega_0 t - k^0_o L)}$, respectively. Similarly, we define the envelopes of the extraordinary wave at the same positions as $B_0(t) = \hat{E}^{(+)}_e(t,0)e^{i\omega_0 t}$ and $B_1(t) = \hat{E}^{(+)}_e(t,L)e^{i(\omega_0 t - k^0_e L)}$. Here, $k^0_\mu = k_\mu(0)$. Therefore, we express

$$\begin{aligned} A_1(t) = &\int \epsilon_o(\Omega,0)e^{ik_o(\Omega)L - i(\omega_0+\Omega)t}\frac{\mathrm{d}\Omega}{2\pi} \\ &+ \sigma L \int\int \alpha(\Omega+\Omega')\epsilon^{\dagger}_e(\Omega',0)e^{i\Delta(\Omega,\Omega')\frac{L}{2}}\,\mathrm{sinc}\left(\Delta(\Omega,\Omega')\frac{L}{2}\right)e^{ik_o(\Omega)L - i(\omega_0+\Omega)t}\mathrm{d}\Omega'\frac{\mathrm{d}\Omega}{2\pi}, \end{aligned} \tag{97a}$$

$$\begin{aligned} B_1(t) = &\int \epsilon_e(\Omega,0)e^{ik_e(\Omega)L - i(\omega_0+\Omega)t}\frac{\mathrm{d}\Omega}{2\pi} \\ &+ \sigma L \int\int \alpha(\Omega+\Omega')\epsilon^{\dagger}_o(\Omega',0)e^{i\Delta(\Omega,\Omega')\frac{L}{2}}\,\mathrm{sinc}\left(\Delta(\Omega,\Omega')\frac{L}{2}\right)e^{ik_e(\Omega)L - i(\omega_0+\Omega)t}\mathrm{d}\Omega'\frac{\mathrm{d}\Omega}{2\pi}, \end{aligned} \tag{97b}$$

where, we can evaluate $A_0(t)$ and $B_0(t)$ by substituting $L = 0$. Expressed in these terms, the field transformation within the crystal adopts the form of an integral *Bogoliubov* transformation

$$A_1(t) = \int U_A(t,t')A_0(t')dt' + \int V_A(t,t')B^{\dagger}_0(t')dt', \tag{98a}$$

$$B_1(t) = \int U_B(t,t')B_0(t')dt' + \int V_B(t,t')A^{\dagger}_0(t')dt', \tag{98b}$$

where the Bogoliubov kernels are defined as

$$U_A(t,t') = \int e^{i[k_o(\Omega)-k_o^0]L+i\Omega(t'-t)}\frac{d\Omega}{2\pi}, \tag{99a}$$

$$V_A(t,t') = \int e^{i[k_o(\Omega)-k_o^0]L-i(\Omega't'+\Omega t)}J(\Omega,\Omega')\frac{d\Omega d\Omega'}{2\pi}, \tag{99b}$$

$$U_B(t,t') = \int e^{i[k_e(\Omega)-k_e^0]L+i\Omega(t'-t)}\frac{d\Omega}{2\pi}, \tag{99c}$$

$$V_B(t,t') = \int e^{i[k_e(\Omega')-k_e^0]L-i(\Omega't+\Omega t')}J(\Omega,\Omega')\frac{d\Omega d\Omega'}{2\pi}. \tag{99d}$$

In this context,

$$J(\Omega,\Omega') = \kappa L\alpha(\Omega+\Omega')\Phi(\Omega,\Omega') \tag{100}$$

represents the joint spectral amplitude (JSA) of the two generated photons, or the biphoton [94].

Spectral and temporal shapes of the photons

The spectra of the ordinary and extraordinary waves are given by $S_\mu(\Omega) = \langle\epsilon_\mu^\dagger(\Omega,L)\epsilon_\mu(\Omega,L)\rangle$, where $\mu = o, e$. After substituting the solutions from Eqs. (94a) and (94b), we obtain for the ordinary photon,

$$\begin{aligned} S_o(\Omega) = \Big\langle &\left[\epsilon_o^\dagger(\Omega,0) + \kappa L\int \alpha^*(\Omega+\Omega')\epsilon_e(\Omega',0)\Phi^*(\Omega,\Omega')d\Omega'\right] \\ &\left[\epsilon_o(\Omega,0) + \kappa L\int \alpha(\Omega+\Omega')\epsilon_e^\dagger(\Omega',0)\Phi(\Omega,\Omega')d\Omega'\right]\Big\rangle. \end{aligned} \tag{101}$$

Applying the commutation relation from Eq. (92) in (101), and nullifying all normally ordered averages at $x=0$, we arrive at the following expression

$$S_o(\Omega) = 2\pi(\kappa L)^2\int\int \delta(\Omega'-\Omega'')\alpha^*(\Omega+\Omega')\alpha(\Omega+\Omega'')\Phi^*(\Omega,\Omega')\Phi(\Omega,\Omega'')\mathrm{d}\Omega'\Omega'' \tag{102}$$

and integrating with respect to Ω'', we obtain

$$S_o(\Omega) = 2\pi\int \left|J(\Omega,\Omega')\right|^2 d\Omega'. \tag{103}$$

A similar expression for $S_e(\Omega)$ can be evaulated, by replacing $J(\Omega,\Omega')$ with $J(\Omega',\Omega)$.

To obtain these spectra analytically, we make two approximations. The first approximation involves linear dispersion in the crystal, considering only linear terms in the dispersion law in the crystal. This is justified for a not-too-long crystal [73, 95]. Hence, we express $k_\mu(\Omega) \approx k_\mu^0 + k_\mu'\Omega$, where $k_\mu' = (dk_\mu/d\Omega)_{\Omega=0}$ is the inverse group velocity of the wave

$\mu = p, o, e$ in the nonlinear crystal. This approximation leads to

$$\Delta(\Omega, \Omega')L/2 \approx \tau_o\Omega + \tau_e\Omega', \tag{104}$$

where $\tau_o = (k'_p - k'_o)L/2$ and $\tau_e = (k'_p - k'_e)L/2$ are relative group delays of the ordinary and extraordinary photons with respect to the pump at half crystal length. Additionally, we assume perfect phase matching at degeneracy, i.e., $k_p^0 - k_o^0 - k_e^0 = 0$.

The second approximation involves replacing the $\mathrm{sinc}(x)$ function with a Gaussian function of the same width at half maximum, given by $e^{-x^2/2\sigma_s^2}$, where $\sigma_s = 1.61$ [90, 95]. Applying both approximations, we express

$$\Phi(\Omega, \Omega') \approx \exp\left[-\frac{(\tau_o\Omega + \tau_e\Omega')^2}{2\sigma_s^2} + i(\tau_o\Omega + \tau_e\Omega')\right]. \tag{105}$$

Substituting Eqs. (85), (105) and (100) into Eq. (103), we obtain

$$S_o(\Omega) = \pi\left(\frac{E_0\kappa L}{\Omega_p}\right)^2 \int \exp\left[-\frac{(\Omega+\Omega')^2}{2\Omega_p^2} - \frac{(\tau_o\Omega + \tau_e\Omega')^2}{\sigma_s^2}\right] \mathrm{d}\Omega'. \tag{106}$$

The given expression corresponds to a one-dimensional Gaussian integral and can be evaluated using the formula

$$\int_{-\infty}^{\infty} e^{-ax^2+bx+c}\, dx = \sqrt{\frac{\pi}{a}}\, e^{\frac{b^2}{4a}+c}. \tag{107}$$

Through this, we arrive at

$$S_\mu(\Omega) = \frac{\sqrt{2\pi}P_b}{\sigma_\mu} e^{-\Omega^2/2\sigma_\mu^2}, \tag{108}$$

where the spectral standard deviation of the ordinary photon is

$$\sigma_o = \frac{\sqrt{\sigma_s^2 + 2\tau_e^2\Omega_p^2}}{\sqrt{2}|\tau_e - \tau_o|}, \tag{109}$$

that of the extraordinary photon, σ_e, is obtained by replacing $\tau_o \leftrightarrow \tau_e$, and

$$P_b = \int \left|J(\Omega, \Omega')\right|^2 d\Omega d\Omega' = \frac{\sqrt{2}\pi^2(\kappa L E_0)^2\sigma_s}{\Omega_p|\tau_e - \tau_o|} \tag{110}$$

is the probability of biphoton generation per pump pulse.

The temporal shapes of the photons are determined by their average intensities (in photon flux units), denoted as $I_\mu(t) = \langle \hat{E}_\mu^{(-)}(t, L)\hat{E}_\mu^{(+)}(t, L)\rangle$. For the ordinary photon, using Eqs. (98a), (99a), and (99b), we derive

$$I_o(t) = \frac{1}{2\pi}\int e^{i[k_o(\Omega')-k_o(\Omega)]L+i(\Omega-\Omega')t}d\Omega d\Omega' \times \int J^*(\Omega,\Omega'')J(\Omega',\Omega'')d\Omega''. \tag{111}$$

Substituting Eqs. (85), (105) and (100) into Eq. (111), we obtain

$$I_o(t) = \left(\frac{\kappa L E_0}{\Omega_p}\right)^2 \frac{1}{4\pi}\int e^{i(\Omega-\Omega')(t-t_0-\tau_o-k_o'L)} \times \exp\left[-\frac{(\tau_o\Omega+\tau_e\Omega'')^2+(\tau_o\Omega'+\tau_e\Omega'')^2}{2\sigma_s^2}\right] \times \exp\left[-\frac{(\Omega+\Omega'')^2+(\Omega'+\Omega'')^2}{4\Omega_p^2}\right] d\Omega d\Omega' d\Omega''. \tag{112}$$

Introducing a change of variables $\Omega_+ = \Omega+\Omega'$ and $\Omega_- = \frac{1}{2}(\Omega-\Omega')$, we express Eq. (112) as

$$I_o(t) = \tilde{I}\int e^{2i\Omega_-(t-t_0-\tau_o-k_o'L)-\frac{\Omega_-^2}{2\Sigma_o^2}}d\Omega_-, \tag{113}$$

where

$$\frac{1}{\Sigma_o^2} = \frac{1}{\Omega_p^2}+\frac{2\tau_o^2}{\sigma_s^2} \tag{114}$$

and

$$\tilde{I} = \left(\frac{\kappa L E_0}{\Omega_p}\right)^2 \frac{1}{4\pi}\int \exp\left[-\frac{\left(\frac{1}{2}\Omega_+ + \Omega''\right)^2}{2\Omega_p^2}\right] \times \exp\left[-\frac{\left(\frac{1}{2}\Omega_+\tau_o+\Omega''\tau_e\right)^2}{\sigma_s^2}\right] d\Omega_+ d\Omega''. \tag{115}$$

The integral in Eq. (113) is evaluated using Eq. (107), and the integral in Eq. (115) is evaluated by applying this formula twice. As a result, we obtain

$$I_\mu(t) = \frac{P_b}{\sqrt{2\pi}\Delta t_\mu}e^{-(t-t_0-\tau_\mu-k_\mu'L)^2/2\Delta t_\mu^2}, \tag{116}$$

where the temporal standard deviation or the temporal width of the ordinary photon is

$$\Delta t_o = \frac{\sqrt{\sigma_s^2+2\tau_o^2\Omega_p^2}}{2\sigma_s\Omega_p}, \tag{117}$$

while that of the extraordinary photon, Δt_e, is obtained by replacing $\tau_o \leftrightarrow \tau_e$.

We note from Eqs. (108) and (116) that for both photons

$$\int_{-\infty}^{+\infty} I_\mu(t)dt = \int_{-\infty}^{+\infty} S_\mu(\Omega)\frac{d\Omega}{2\pi} = P_b, \tag{118}$$

and since $I_\mu(t)$ has the meaning of the photon flux, Eq. (118) justifies the interpretation of P_b as the probability of biphoton generation in one excitation cycle.

Characterization of light produced in BBO crystal

The Barium Borate (BBO) crystal, known for its nonlinear properties, has the capability to generate entangled photon pairs. The Sellmeier equation for this crystal, from Ref. [96], is expressed as follows

$$\tilde{n}_e^2(\lambda) = 2.373 + \frac{0.0128}{\lambda^2 - 0.0156} - 0.0044\lambda^2, \tag{119a}$$

$$\tilde{n}_o^2(\lambda) = 2.7405 + \frac{0.0184}{\lambda^2 - 0.0179} - 0.0155\lambda^2, \tag{119b}$$

where λ is measured in micrometers.

The Sellmeier equations give an empirical relationship between refractive index and wavelength for a particular transparent medium and they are used to determine the dispersion of light in the medium. Now we consider a BBO crystal of length $L = 2$ cm, pumped at 405 nm by Gaussian pump pulses with a FWHM bandwidth $\Delta\lambda = 0.2$ nm, similar to the experimental setup of Ref. [75], but with a longer crystal and longer pump pulses. The pump bandwidth corresponds to $\Omega_p = 0.98$ rad/ps or $\tau_p = 1.21$ ps.

Angle between the pump and the optical axis.

Utilizing Eqs. (119a) and (119b), we determine the refractive index $\tilde{n}_\mu(\lambda)$. Subsequently, we convert this value into a function of frequency, denoted as $n_\mu(\omega)$, and further derive the corresponding values of $k_\mu = n_\mu\omega_\mu/c$. Now, the refractive index along the direction of propagation of a wave can also be written as[58, 90]

$$n_\mu(\omega) = \left[\frac{\sin^2\theta_\mathrm{p}}{n_e(\omega)^2} + \frac{\cos^2\theta_\mathrm{p}}{n_o(\omega)^2}\right]^{-\frac{1}{2}}, \tag{120}$$

where θ_p is the angle between the optical axis and the pump.

The phase mismatch angle at degeneracy is defined as $\phi_0(\theta_p) = \Delta(0,0)L/2$, from Eqs.

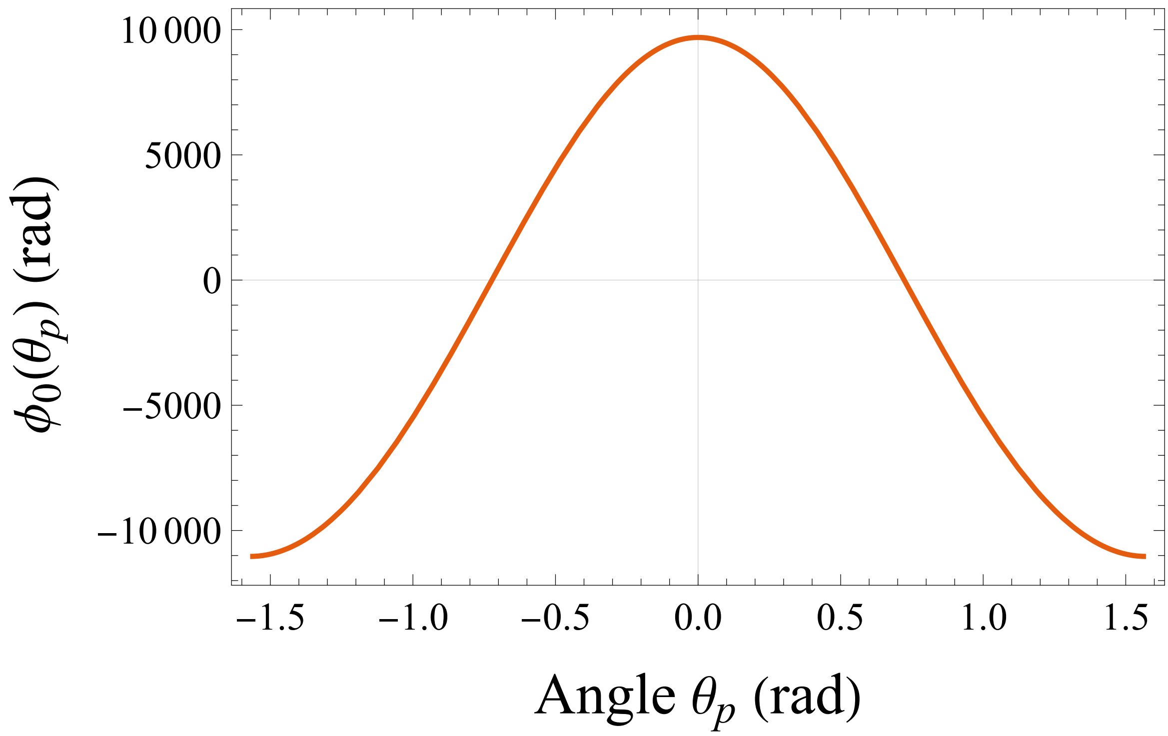

Figure 9: Phase mismatch angle as a function of the angle between the optical axis and the pump.

(221) and (120), we find

$$\phi_0(\theta_p) = \left(\left[\frac{\sin^2\theta_\mathrm{p}}{n_e(\omega_p)^2} + \frac{\cos^2\theta_\mathrm{p}}{n_o(\omega_p)^2} \right]^{-\frac{1}{2}} \times \frac{\omega_p}{c} - k_o(\omega_o) - \left[\frac{\sin^2\theta_\mathrm{p}}{n_e(\omega_e)^2} + \frac{\cos^2\theta_\mathrm{p}}{n_o(\omega_e)^2} \right]^{-\frac{1}{2}} \times \frac{\omega_e}{c} \right) \frac{L}{2}. \tag{121}$$

We substitute the numerical values in the above equation and plot $\phi_0(\theta_p)$ as a function of θ_p as illustrated in Figure 9. For having a perfect phase-matching, we need to have $\phi_0(\theta_p) \approx 0$, and so we find the angle θ_p at which this condition is satisfied. We calculate this angle to be 0.723 rad or $\theta_p = 41.42°$. The JSA calculated for these parameters is shown in Figure 10.

From Eqs. (119a) and (119b), we also calculate $\tau_o = 0.76$ ps and $\tau_e = 2.68$ ps. For these conditions, we find $\sigma_o = 1.48$ rad/ps and $\sigma_e = 0.71$ rad/ps, which give the ratio $\sigma_o/\sigma_e = 2.1$, showing the asymmetry in the spectral bandwidth of two generated photons. Substituting the value of τ_o in Eq. (117), we find $\Delta t_o = 0.61$ ps and for τ_e, we replace $\tau_o \leftrightarrow \tau_e$ to obtain $\Delta t_e = 1.28$ ps.

In the case of a sufficiently narrowband pump, where $\tau_\mu \Omega_p \ll \sigma_s$, both the temporal standard deviations of ordinary and extraordinary photons are approximately equal and given by $1/2\Omega_p = \sigma_t$. This implies that the downconverted photons have a probability of appearing until the pump pulse is inside the crystal. The spectral standard deviations for both photons are also the same in this scenario, and they are equal to the continuous-wave

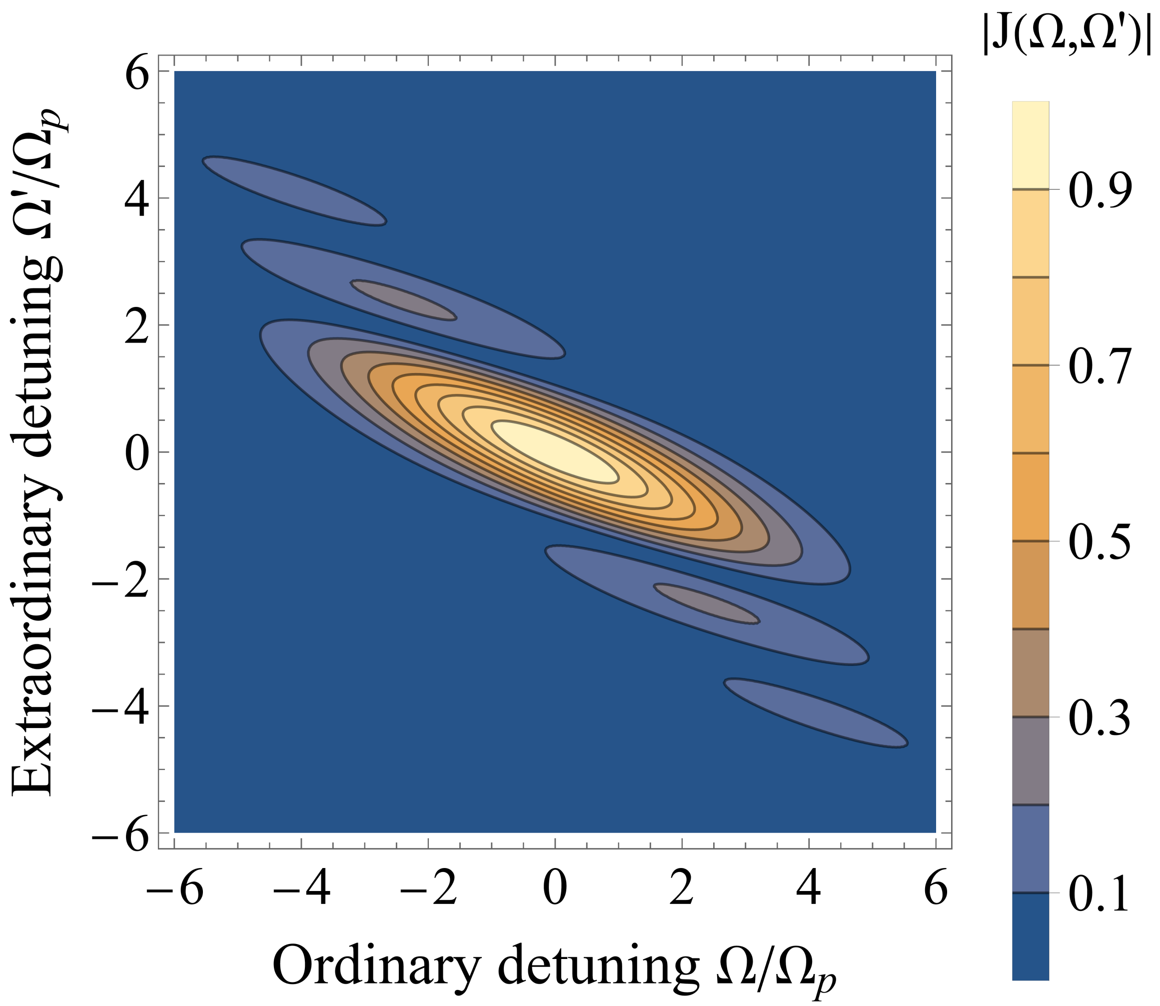

Figure 10: Normalized contour plot of the JSA for two photons generated in a 2-cm-long BBO crystal pumped at 405 nm. The tilted shape of the JSA indicates the frequency-time entanglement between the photons. The bandwidth of the ordinary photon is more than two times higher than that of the extraordinary one.

(CW) spectral standard deviation , given by

$$\sigma_{\text{cw}} = \frac{\sigma_s}{\sqrt{2}|\tau_e - \tau_o|}. \tag{122}$$

For our example of a BBO crystal, this results in $\sigma_{\text{cw}} = 0.59$ rad/ps.

However, when the above condition is not satisfied, and, in addition, the group velocities of the ordinary and extraordinary waves are significantly different, the durations and delays of the two generated photons are different too, as shown schematically in Figure 11. The peak of the single-photon wavepacket polarized in the direction $\mu = o, e$ passes the output face of the crystal at time $t_0 + \tau_\mu + k'_\mu L$, while the peak of the pump pulse passes this face at time $t_0 + k'_p L$. The relative delay with respect to the pump is thus $-\tau_\mu$, it is negative in a crystal with a positive dispersion, where the group velocity decreases with frequency, which means that the downconverted photons advance the pump pulse. The relative delay between the photons can be easily compensated by an optical delay line. Still, the difference in wavepacket duration is a serious problem for observing a Hong-Ou-Mandel interference of them. The photons are partially distinguishable in this case, and, as a consequence, the Hong-Ou-Mandel interference of these photons exhibits degraded visibility [73–75]. A time lens can be used for temporal stretching of the shorter wavepacket, as shown in the following sections.

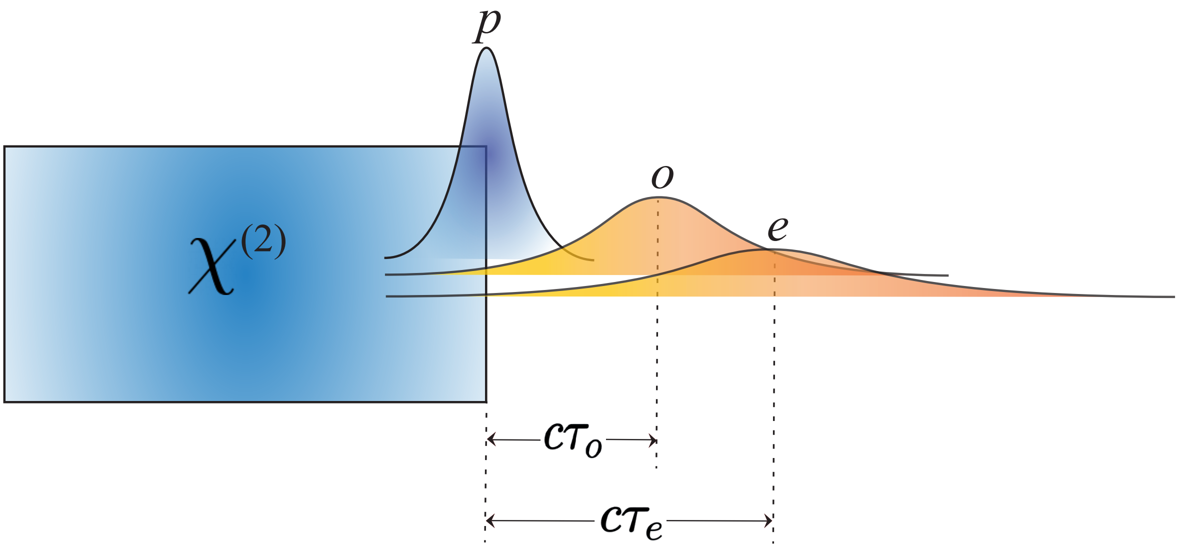

Figure 11: Schematic representation of the generation of two photons, ordinary (o) and extraordinary (e), by type-II PDC from a pump pulse (p) in a crystal with quadratic nonlinear susceptibility. For a broadband pump, the generated wave packets may be much longer than the pump pulse. In a crystal with positive dispersion, the generated photons travel at a higher group velocity in comparison to the pump and advance the pump pulse at the output.

2.2 Coincidence detection and relative group delays

The interferometer we consider includes a single-lens temporal imaging system in its arm where the ordinary wave propagates. Such a system realizes a temporal stretching or compression of a waveform similar to the action of an ordinary single-lens imaging system in space as we discussed in Section 1.3. A time lens is a device realizing a quadratic-in-time phase modulation of the passing waveform. It can be realized by an EOPM (electro-optical time lens) or by a nonlinear medium performing SFG of FWM (parametric time lens).

Here we rewrite the transformation of the field in a single-time-lens imaging system (65) as

$$A_3(t_{\text{out}} + \Delta t_{\text{out}}) = \frac{-1}{\sqrt{M}} e^{i\Delta t_{\text{out}}^2/2MD_{\text{f}}} A_2(t_{\text{in}} + \Delta t_{\text{in}}), \tag{123}$$

where $A_2(t)$ and $A_3(t)$ are field envelopes at the input and output of the temporal imaging system respectively. Here t_{in} is the time corresponding to the center of the temporal field of view [47], a time axis (similar to the optical axis of a spatial imaging system). This time is determined by the time of passage of the modulating signal in an EOPM or by the time of passage of the pump pulse in a parametric time lens. Correspondingly, t_{out} is the central time of the image waveform. It is related to t_{in} as $t_{\text{out}} = t_{\text{in}} + t_d$, where t_d is the group delay time in the temporal imaging system. In addition, Δt_{out} and Δt_{in} are times relative to the centers of the object and image, respectively; they are related by a scaling $\Delta t_{\text{out}} = M\Delta t_{\text{in}}$.

For practical use, we rewrite Eq. (123) as

$$A_3(t) = \frac{-1}{\sqrt{M}} e^{i(t-t_{\text{out}})^2/2MD_{\text{f}}} A_2\left(t_{\text{out}} - t_d + \frac{t - t_{\text{out}}}{M}\right), \tag{124}$$

where t_{out} and t_d can be considered as constants specific to a given time lens.

Equations (123) and (124) are obtained in several approximations, the two most important being that of the Fraunhofer limit for the dispersion and that of an infinitely large temporal aperture T_A of the time lens. The first approximation mentioned requires that $D_{\text{in}}^2 \gg 1/4\sigma_o^4$, as shown in Appendix A. The second one requires that the FWHM of the stretched pulse does not surpass the temporal aperture, i.e., $2\sqrt{2\ln 2}\Delta t_{\text{str}} < T_A$, where $\Delta t_{\text{str}} = |D_{\text{in}}|\sigma_o$ is the temporal standard deviation of the pulse stretched in the first dispersive medium, as also shown in Appendix A. While the first requirement sets a lower bound for σ_o, the second one sets its upper bound. We obtain from Eq. (64) and the definition of magnification that $D_{\text{in}} = D_{\text{f}}(M-1)/M$. Therefore, we can write both bounds as

$$\frac{M^2}{4D_{\text{f}}^2(M-1)^2} \ll \sigma_o^4 < \frac{T_A^4 M^4}{D_{\text{f}}^4(M-1)^4(8\ln 2)^2}. \tag{125}$$

The bounds are compatible if

$$T_A^4 \gg (4\ln 2)^2 D_{\text{f}}^2 (M-1)^2/M^2. \tag{126}$$

As mentioned in the Introduction, a time lens can be realized by an EOPM or a nonlinear optical process, such as SFG or FWM. An SFG-based time lens always changes the carrier frequency of the signal field and is therefore unsuitable for the case of two photons having the same carrier frequency, considered here.

For an EOPM-based time lens, the temporal aperture is given by $T_A = 1/2\pi f_{\text{RF}}$, where f_{RF} is the operating radio frequency of the phase modulator, while the focal GDD is $D_{\text{f}} = T_A^2/\theta_{\max}$, where $\theta_{\max}$ is the maximal achievable phase shift, limited by the damage threshold of the modulator crystal [12, 13, 17]. Thus, Eq. (126) implies $\theta_{\max}^2 \gg 7.7(M-1)^2/M^2$, which is feasible for modern EOPM-based time lenses, where a value of $\theta_{\max} = 25$ rad has been reported [37], and for a magnification $|M| > 1$, which we consider in the setup of Figure 8. Taking this value of the maximal phase shift and $f_{\text{RF}} = 40$ GHz [37, 79], we obtain $T_A = 4$ ps and $D_{\text{f}} = 0.64$ ps^2. For a magnification $M = -2.1$, required for the case of the previous section, we obtain from Eq. (125) the condition $\sigma_o^4 \gg 0.28$ rad^4/ps^4 and $\sigma_o < 1.8$ rad/ps. Both these conditions are satisfied by the BBO source considered in the previous section. We note that a Fresnel time lens based on an EOPM with a nonsinusoidal driving current provides a higher temporal aperture for fixed $\theta_{\max}$ and D_{f} [38, 39].

Frequency-degenerate FWM is technically more complicated but provides a wider range of possible focal GDDs and temporal apertures. In a FWM-based time lens, a pump pulse of FWHM duration τ_0 passes through a dispersive medium with GDD D_p and acquires a FWHM duration $T_A = 4\ln 2|D_\mathrm{p}|/\tau_0$, which constitutes the temporal aperture. The focal GDD is given by $D_\mathrm{f} = -D_\mathrm{p}/2$ [13]. Taking realistic values $\tau_0 = 0.1$ ps, $D_\mathrm{p} = -44$ ps^2 [30], and $M = -2.1$, we obtain from Eq. (125) the condition $\sigma_o^4 \gg 0.0002$ rad^4/ps^4 and $\sigma_o < 16$ rad/ps. Both these conditions are satisfied with very wide margins by the BBO source considered in the previous section.

Coincidence detection

We define the position of the output mirror of the interferometer shown in Figure 8 as $x = x_4$ and assume that the detectors are placed just after it at the same position. The field operators at detectors D1 and D2 are given by

$$\hat{E}_1^{(+)}(t) = \frac{1}{\sqrt{2}}[\hat{E}_o^{(+)}(t, x_4) + \hat{E}_e^{(+)}(t - t_z, x_1)], \tag{127a}$$

$$\hat{E}_2^{(+)}(t) = \frac{1}{\sqrt{2}}[\hat{E}_o^{(+)}(t, x_4) - \hat{E}_e^{(+)}(t - t_z, x_1)], \tag{127b}$$

where $t_z = t_{z0} + \delta\tau$ with t_{z0} the time delay experienced by the extraordinary wave in the interferometer and $\delta\tau$ the additional delay introduced for this wave.

The probability of detecting one photon at detector D1 at time t_1 and one photon at detector D2 at time t_2 is

$$\begin{aligned} P_{12}(t_1, t_2; \delta\tau) &= \langle \hat{E}_1^{(-)}(t_1)\hat{E}_2^{(-)}(t_2)\hat{E}_2^{(+)}(t_2)\hat{E}_1^{(+)}(t_1)\rangle \\ &= \left|\langle \hat{E}_2^{(+)}(t_2)\hat{E}_1^{(+)}(t_1)\rangle\right|^2 + O(\xi^4), \end{aligned} \tag{128}$$

where $\xi = \kappa L E_0 \ll 1$ is the smallness parameter of the low-gain regime of PDC.

The average coincidence counting rate is given by [73]

$$R_c(\delta\tau) = \frac{1}{T}\int\int_0^T dt_1 dt_2 P_{12}(t_1, t_2; \delta\tau), \tag{129}$$

where T is the coincidence detection time .

Relative delays

Uniting the transformations presented above, we need to take into account relative delays between the parts of the interferometric setup shown in Figure 8. In doing this, we need to remember that the field envelope travels in a dispersive medium at the group velocity, while the central frequency component travels at the phase velocity. In the air, these two velocities practically coincide, but, in a dense dispersive medium, they may be significantly different, which results in the appearance of a phase shift for the field amplitude.

In this way, we write $A_2(t) = A_1(t - t_{12})$, where t_{12} is the delay between the point $x_1 = L$ (PDC crystal output) and point x_2 (temporal imaging system input). Also, we write $\hat{E}_o^{(+)}(t, x_4) = A_3(t - t_{34})e^{-i\omega_0 t + i\phi}$, where t_{34} is the delay between the point x_3 (temporal imaging system output) and point x_4 (interferometer output mirror), while ϕ is a phase caused by the difference of the phase and group velocities in the media of the temporal imaging system. We do not write this phase explicitly, because it does not affect the second-order interference picture, as we show below.

For perfect interference, we expect that the total delay of the ordinary wave matches that of the extraordinary one. The ordinary wave emerges when the pump pulse enters the nonlinear crystal. In a crystal with positive dispersion, the subharmonic travels at a higher group velocity than the pump. This means that the ordinary wave is a longer pulse, advanced with respect to the pump pulse (see Figure 11). The center of this ordinary pulse is generated when the peak of the pump pulse passes the crystal center, which happens at time $t_0 + k'_p L/2$. We recall that $k'_p = 1/v_g$ is the inverse of the group velocity v_g of the pump. Thus, the center of the ordinary pulse leaves the crystal at time $t_0 + k'_p L/2 + k'_o L/2$ and arrives at the exit interferometer mirror, point x_4, at time $t_{4o} = t_0 + k'_p L/2 + k'_o L/2 + t_{12} + t_d + t_{34}$. Similar reasoning gives the time of arrival of the center of the extraordinary pulse $t_{4e} = t_0 + k'_p L/2 + k'_e L/2 + t_{z0}$. A perfect interference is expected to occur at $t_{4o} = t_{4e}$, wherefrom

$$k'_o L/2 + t_{12} + t_d + t_{34} = k'_e L/2 + t_{z0}. \tag{130}$$

Another important relationship is the synchronization condition for the photon pair source and the modulator. The center of the temporal field of view (time axis) t_{in} is expected to coincide with the center of the ordinary pulse, arriving at the time lens:

$$t_{\text{in}} = t_0 + k'_p L/2 + k'_o L/2 + t_{12} + \delta t, \tag{131}$$

where δt is a time shift, describing a possible synchronization imprecision .

Now Eqs. (98a), (98b), (124), (127a), (127b) and (128) represent a closed system of equations, allowing us to express the fields on the detectors through the vacuum fields at the PDC crystal input and calculate the average coincidence counting rate defined in Eq. (129).

2.3 Average coincidence counting rate

In this section, we calculate the average coincidence counting rate bringing together the relations for different parts of the interferometric setup, obtained in the preceding section. To this end, we express the fields in Eq. (128) via the vacuum fields $A_0(t)$ and $B_0(t)$ with the help of Eqs. (98a), (98b), (127a),(127b), (124) and the relations for the field envelopes, discussed in Section 2.2. Then we transform the obtained expression to the normal form using the commutation relations (92) and leave only the c-number terms since the normally ordered correlator for the vacuum field is zero. In the lowest (quadratic) order of $\xi =$

$\kappa L E_0 \ll 1$, we obtain

$$P_{12}(t_1,t_2;\delta\tau) = \frac{1}{4|M|}\left| e^{i(t_1-t_{34}-t_{\text{out}})^2/2MD_{\text{f}}} \int U_B(t_2-t_z,t')V_A(t_y+\frac{t_1-t_{34}-t_{\text{out}}}{M},t')dt' \right.$$
$$\left. - e^{i(t_2-t_{34}-t_{\text{out}})^2/2MD_{\text{f}}} \int U_A(t_y+\frac{t_2-t_{34}-t_{\text{out}}}{M},t')V_B(t_1-t_z,t')dt' \right|^2, \tag{132}$$

where $t_y = t_{\text{out}} - t_d - t_{12}$.

Now, we observe that Eqs. (99a) and (99c) can be expressed as delta functions, therefore we write

$$U_A(t_y+\frac{t_2-t_{34}-t_{out}}{M},t') = \delta(t'-t_y-\frac{t_2-t_{34}-t_{out}}{M}+k_o'L), \quad \text{and} \tag{133a}$$
$$U_B(t_2-t_z,t') = \delta(t'-t_2+t_z+k_e'L). \tag{133b}$$

We substitute Eqs. (133a), (133b), (99b) and (99d) into (132), integrate the delta functions and arrive at

$$P_{12}(t_1,t_2;\delta\tau) = \frac{(\kappa L)^2}{16|M|\pi^2}\left| e^{i(t_1-t_{34}-t_{out})^2/2MD_{\text{f}}} \int\int \mathrm{d}\Omega\mathrm{d}\Omega'\alpha(\Omega+\Omega')\Phi(\Omega,\Omega') \right.$$
$$\times\, e^{ik_o'\Omega L - i(\Omega'[t_2-t_z-k_e'L]+\Omega[t_y+\frac{[t_1-t_{34}-t_{out}]}{M}])} - e^{i(t_2-t_{34}-t_{out})^2/2MD_{\text{f}}} \int\int \mathrm{d}\Omega\mathrm{d}\Omega'$$
$$\left. \times\, \alpha(\Omega+\Omega')\Phi(\Omega,\Omega') \times e^{ik_e'\Omega' L - i(\Omega'[t_1-t_z]+\Omega[t_y+\frac{[t_2-t_{34}-t_{out}]}{M}-k_o'L])} \right|^2. \tag{134}$$

Next, we expand this expression, and substitute it into Eq. (129). Extending the limits of integration over t_1 and t_2 to infinity [73], we obtain

$$\begin{aligned} R_c(\delta\tau) = \frac{(\sigma L)^2}{16T\pi^2}[&\int\int \mathrm{d}\Omega\mathrm{d}\Omega'\alpha(\Omega+\Omega')\alpha^*(\Omega+\Omega')\Phi(\Omega,\Omega')\Phi^*(\Omega,\Omega')4\pi^2 \\ &- \int\int\int\int \mathrm{d}\Omega\mathrm{d}\Omega'\mathrm{d}\Omega''\mathrm{d}\Omega'''\alpha(\Omega+\Omega')\alpha^*(\Omega''+\Omega''')\Phi(\Omega,\Omega')\Phi^*(\Omega'',\Omega''') \\ &\times e^{\frac{iMD_{\text{f}}}{2}[(-\frac{\Omega}{M}+\Omega''')^2-(\frac{\Omega''}{M}-\Omega')^2]+i(\Omega-\Omega'')(k_o'L-t_y)+i(\Omega'-\Omega''')(t_z+k_e'L-t_{34}-t_{out})}(2\pi D_{\text{f}}) \\ &- \int\int\int\int \mathrm{d}\Omega\mathrm{d}\Omega'\mathrm{d}\Omega''\mathrm{d}\Omega'''\alpha(\Omega+\Omega')\alpha^*(\Omega''+\Omega''')\Phi(\Omega,\Omega')\Phi^*(\Omega'',\Omega''') \\ &\times e^{\frac{iMD_{\text{f}}}{2}[(-\frac{\Omega}{M}+\Omega''')^2-(\frac{\Omega''}{M}-\Omega')^2]+i(\Omega-\Omega'')(k_o'L-t_y)+i(\Omega'-\Omega''')(t_z+k_e'L-t_{34}-t_{out})}(2\pi D_{\text{f}}) \\ &+ \int\int \mathrm{d}\Omega\mathrm{d}\Omega'\alpha(\Omega+\Omega')\alpha^*(\Omega+\Omega')\Phi(\Omega,\Omega')\Phi^*(\Omega,\Omega')4\pi^2]. \end{aligned} \tag{135}$$

Simplifying the above expression and using the relations for relative delays (130) and

(131), we write,

$$R_c(\delta\tau) = \frac{P_b}{2T}\left[1 - p_{\text{int}}(\delta\tau)\right], \tag{136}$$

where

$$\begin{aligned} p_{\text{int}}(\delta\tau) &= \frac{D_{\text{f}}}{2\pi P_b}\int\int\int\int d\Omega d\Omega' d\Omega'' d\Omega''' \left|J(\Omega,\Omega')J(\Omega'',\Omega''')\right| \\ &\times \; e^{\frac{iMD_{\text{f}}}{2}[(\frac{\Omega}{M}-\Omega''')^2-(\frac{\Omega''}{M}-\Omega')^2]}e^{i(\Omega-\Omega'')\delta t - i(\Omega'-\Omega''')(\delta\tau-\delta t)}. \end{aligned} \tag{137}$$

This is the conditional probability of destructive interference of two photons under the condition that they are generated. By destructive interference we mean, in the spirit of Ref. [71], the case where both photons go to the same beam-splitter output. The expression (137) looks complex, but with a simple argument, we can prove that it is real. Indeed, if we interchange the variables Ω and Ω' with Ω'' and Ω''' respectively, then the expression becomes complex conjugate. At the same time, the change of variables should not change the integral; therefore we conclude that $p_{\text{int}}(\delta\tau)$ is real. At sufficiently high values of $|\delta\tau|$ and $|\delta\tau - \delta t|$, the function under the integrals in Eq. (137) oscillates very fast with the frequency and its integral is close to zero. Thus, at a high enough delay, the probability of interference tends to zero, and the total number of coincidences $TR_c(\pm\infty)$ tends to $P_b/2$, as expected since each photon can be reflected or transmitted at the beam splitter with a probability $\frac{1}{2}$, giving four possible combinations, two of which result in a coincidence.

The quadruple integral (137) can be made Gaussian with the help of the Gaussian approximation for the phase-matching function (105), already employed in Section 2.1 to calculate the spectral and temporal shapes of the ordinary and extraordinary waves. In this approximation, the integration can be taken analytically by the multidimensional Gaussian integration formula

$$\int_{-\infty}^{\infty} e^{-\mathbf{u}^T\Lambda\mathbf{u}/2+i\mathbf{v}^T\mathbf{u}}d^n u = \left[\frac{(2\pi)^n}{\det\Lambda}\right]^{\frac{1}{2}} e^{-\mathbf{v}^T\Lambda^{-1}\mathbf{v}/2}, \tag{138}$$

where $\mathbf{u}$ and $\mathbf{v}$ are two n-dimensional column vectors, while Λ is an $n\times n$ symmetric matrix.

To simplify the notation, we introduce dimensionless delays, relating them to the pump pulse duration τ_p,

$$T_{o,e} = \frac{\sqrt{2}\Omega_p}{\sigma_s}\tau_{o,e} = \frac{2\sqrt{\ln 2}}{\sigma_s}\frac{\tau_{o,e}}{\tau_p} \approx 1.034\frac{\tau_{o,e}}{\tau_p} \tag{139}$$

and a dimensionless focal GDD $D = 2\Omega_p^2 D_{\text{f}}$.

To transform Eq. (137) with the phase-matching function approximated by Eq. (105) into the matrix form of Eq. (138), we identify $n = 4$, $\mathbf{u} = (\Omega,\Omega',\Omega'',\Omega''')^T$, $\mathbf{v} = (\delta t, \delta t -$

$\delta\tau, -\delta t, \delta\tau - \delta t)^T$, and

$$\Lambda = \frac{1}{2\Omega_p^2}\begin{pmatrix} 1+T_o^2 - iD/M & 1+T_oT_e & 0 & iD \\ 1+T_oT_e & 1+T_e^2+iDM & -iD & 0 \\ 0 & -iD & 1+T_o^2+iD/M & 1+T_oT_e \\ iD & 0 & 1+T_oT_e & 1+T_e^2-iDM \end{pmatrix}. \tag{140}$$

We notice that the third and fourth elements of the vector $\mathbf{v}$ are equal to the first and second ones taken with the opposite sign. This allows us to simplify the quadratic form on the right-hand side of Eq. (138) significantly. Let us denote the inverse of Λ by Π and write it in a block form

$$\Pi = \begin{pmatrix} \Pi_{11} & \Pi_{12} \\ \Pi_{21} & \Pi_{22} \end{pmatrix}, \tag{141}$$

where Π_{ij} are some 2×2 matrices. Now we introduce a two-dimensional column vector $\mathbf{w} = (\delta t, \delta t - \delta\tau)^T$ and write

$$\mathbf{v}^T\Lambda^{-1}\mathbf{v} = \mathbf{w}^T\Gamma\mathbf{w}, \tag{142}$$

where Γ is a 2×2 matrix

$$\Gamma = \Pi_{11} - \Pi_{12} - \Pi_{21} + \Pi_{22}. \tag{143}$$

With the help of Mathematica 12 (as shown in Appendix E), we find

$$\Gamma = \nu\begin{pmatrix} 1+T_e^2+M^2F_+ & -1-T_eT_o-MF_+ \\ -1-T_eT_o-MF_+ & 1+T_o^2+F_+ \end{pmatrix}, \tag{144}$$

where

$$\nu = \frac{(T_e-T_o)^2}{4\Omega_p^6\det\Lambda}, \tag{145a}$$

$$\det\Lambda = \frac{(T_e-T_o)^4}{16\Omega_p^8}\left(1+M^2F_+F_-/D^2\right), \quad \text{and} \tag{145b}$$

$$F_\pm = \frac{D^2\left[(1\pm M)^2 + (T_e \pm MT_o)^2\right]}{M^2(T_e-T_o)^2}. \tag{145c}$$

Thus, we finally obtain

$$p_{\text{int}}(\delta\tau) = \frac{|T_e-T_o|\,D_{\text{f}}}{\Omega_p^2\sqrt{\det\Lambda}}e^{-\mathbf{w}^T\Gamma\mathbf{w}/2}. \tag{146}$$

Let us show that both eigenvalues of Γ are positive for any values of the parameters T_e, T_o, D, and M. First, we find

$$\det\Gamma = \nu^2(T_e-T_o)^2\left(1+M^2F_+F_-/D^2\right), \tag{147}$$

which is obviously positive for $T_o \neq T_e$. Then, we write the characteristic polynomial in the form

$$f(\lambda) = \lambda^2 - (\Gamma_{11} + \Gamma_{22})\lambda + \det\Gamma, \tag{148}$$

where Γ_{ij} are the elements of the matrix Γ. This function represents a parabola with a vertex at $\lambda_0 = (\Gamma_{11} + \Gamma_{22})/2$, which is positive, where $f(\lambda_0) = -(\Gamma_{11} + \Gamma_{22})^2/4 - \Gamma_{12}^2$, which is negative. This means that the parabola intersects the $f = 0$ axis at two points, one of which is positive. The second eigenvalue is positive too since the determinant is given by the product of eigenvalues. As a consequence, at high delay $\delta\tau$, $p_{\text{int}}(\delta\tau)$ tends to zero, as anticipated above.

The average coincidence rate reaches its minimum at some delay $\delta\tau_{\text{min}}$. This delay corresponds to the minimal value of the quadratic form $\mathbf{w}^T\Gamma\mathbf{w}$ and can be found by taking its derivative with respect to $\delta\tau$ and setting it to zero:

$$\delta\tau_{\text{min}} = \left(1 + \frac{\Gamma_{12}}{\Gamma_{22}}\right)\delta t. \tag{149}$$

The visibility of the Hong-Ou-Mandel interference picture is defined as the ratio of the dip to the coincidence rate at a high delay:

$$V = \frac{R_c(\infty) - R_c(\delta\tau_{\text{min}})}{R_c(\infty)} = p_{\text{int}}(\delta\tau_{\text{min}}), \tag{150}$$

where we have used the expression for the average coincidence rate (136) and the fact that $p_{\text{int}}(\infty) = 0$, established above. Below we analyze the visibility for the cases of perfect and imperfect synchronization.

2.4 Synchronizations and post-time lens analysis

Perfect synchronization

At perfect synchronization of the PDC pump pulse and the time axis of the time lens, $\delta t = 0$ and therefore, from Eq. (149), $\delta\tau_{\text{min}} = 0$. The interference probability is

$$p_{\text{int}}^{\text{PS}}(\delta\tau) = \frac{2D}{|T_e - T_o|\sqrt{1 + M^2F_+F_-/D^2}}e^{-\Gamma_{22}\delta\tau^2/2}, \tag{151}$$

where

$$\Gamma_{22} = 4\sigma_{\text{cw}}^2\frac{1 + T_o^2 + F_+}{1 + M^2F_+F_-/D^2}. \tag{152}$$

With varying magnification, the visibility $p_{\text{int}}^{\text{PS}}(0)$ reaches its maximum at the minimal value of the function $g(M) = M^2F_+F_-$. Equalizing its derivative to zero, we find the optimal magnification

$$M_{\rm opt} = \pm\sqrt{\frac{1+T_e^2}{1+T_o^2}} = \pm\frac{\Delta t_e}{\Delta t_o}, \tag{153}$$

where Δt_o and Δt_e are the standard deviations of the temporal shapes of the ordinary and extraordinary waves respectively, found in Section 2.1. The minimal value $g(M_{\rm opt}) = 4D^4/(T_e - T_o)^2$ and therefore the optimal visibility at perfect synchronization is

$$V_{\rm opt}^{\rm PS} = \frac{2D}{\sqrt{(T_e - T_o)^2 + 4D^2}}. \tag{154}$$

From a physical point of view, the optimal magnification, given by Eq. (153), is completely clear and expected. It corresponds to the ratio of the temporal widths of the ordinary and extraordinary photons, i.e., at the optimal magnification, the duration of the stretched ordinary photon equals the duration of the extraordinary one. The minus sign in Eq. (153) corresponds to the inversion of the temporal waveform, which does not affect the visibility, since the photon has a symmetric temporal shape and we are considering a perfect synchronization, where the center of the photon coincides with the center of the field of view of the time lens.

When the focal GDD of the time lens is high enough so that the relation $D^2 \gg (T_e - T_o)^2/4$ or

$$D_{\rm f}^2 \gg \frac{1}{4\Omega_p^2\sigma_{\rm cw}^2} \tag{155}$$

holds, the visibility approaches unity (see Figure 12).

At a lower D, the interference is not perfect because a time lens adds a residual chirp to the stretched ordinary pulse, which does not match perfectly the extraordinary one, notwithstanding having the same duration and the temporal intensity shape. This chirp tens to zero as $D_{\rm f}$ tends to infinity, as can be seen from Eq. (124). For the examples considered in Section 2.2, we obtain the values of $4D_{\rm f}^2\Omega_p^2\sigma_{\rm cw}^2$ equal to 0.55 and 650 for EOPM and FWM based lenses, respectively. We see that the FWM-based lens considered satisfies the condition (155), while the EOPM-based lens considered does not reach the limit $D \to \infty$ and allows one to obtain only a limited visibility of $(1 + 1/0.55)^{-1/2} = 0.6$.

The limit of $M = 1$ and $D_{\rm f} \to \infty$ corresponds to a lensless setup, where the imaging transformation (123) reduces to a translation in time. In this limit we find

$$p_{\rm int}^{\rm lensless}(\delta\tau) = \frac{2}{\sqrt{4 + (T_e + T_o)^2}} e^{-2\sigma_{\rm cw}^2\delta\tau^2}. \tag{156}$$

We see that for a lensless setup, the width of the HOM dip is independent of the pump spectral width, while the visibility is maximal in the CW limit ($\Omega_p \to 0$), where it is equal to one, and degrades with the growing pump spectral width [73, 74]. In Figure 13 we show the coincidence rate in the CW limit, its degraded version for a pulsed pump, and the interference picture restored by a time lens with a sufficiently high focal GDD.

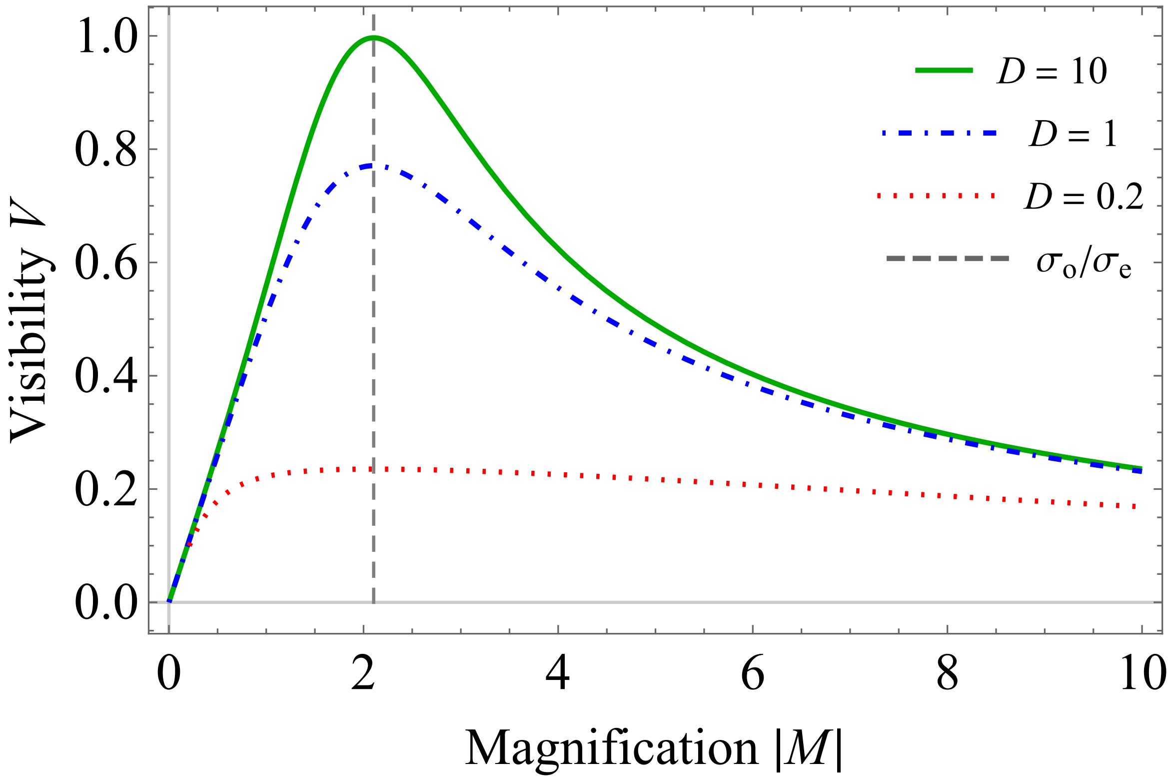

Figure 12: Interferometric visibility plotted at perfect synchronization as a function of the magnification $|M|$ for different values of focal GDD. The source parameters are as in Section 2.1. The maximal visibility is reached at the optimal magnification, corresponding to the ratio $\Delta t_e/\Delta t_o = \sigma_o/\sigma_e$.

We see in Figure 13 that the dip of the restored interference picture is much wider than that of the case of the CW pump. This might appear paradoxical, because the CW limit corresponds to long pump pulses, e.g., nanosecond scale, which produce long subharmonic pulses, as discussed in Section 2.1, while a short pump pulse produces subharmonic pulses of the same scale, picosecond in the considered example. It might be expected that longer pulses have a longer correlation time. However, that is not the case; the correlation time (standard deviation of the interference dip) in the lensless CW limit is equal to $\tau_{\text{cw}} = 0.5\sigma_{\text{cw}}^{-1}$, as follows from Eq. (156), and is unrelated to the pump pulse duration. For a pulsed pump and in the presence of a lens, the correlation time is $\tau_{\text{pulsed}} = \Gamma_{22}^{-1/2}$, as follows from Eq. (151). In the example considered this time is $\tau_{\text{pulsed}} = 1.4\sigma_{\text{cw}}^{-1}$ and is much longer than τ_{cw}. A longer correlation time may be beneficial for some applications of indistinguishable photons, such as boson samplers [76, 77], because it makes photons less sensitive to the emission time jitter.

Imperfect synchronization

In the case of imperfect synchronization, $\delta t \neq 0$ and the position of the dip of the average coincidence rate depends on δt (see Figure 14). In addition, this dip is less pronounced.

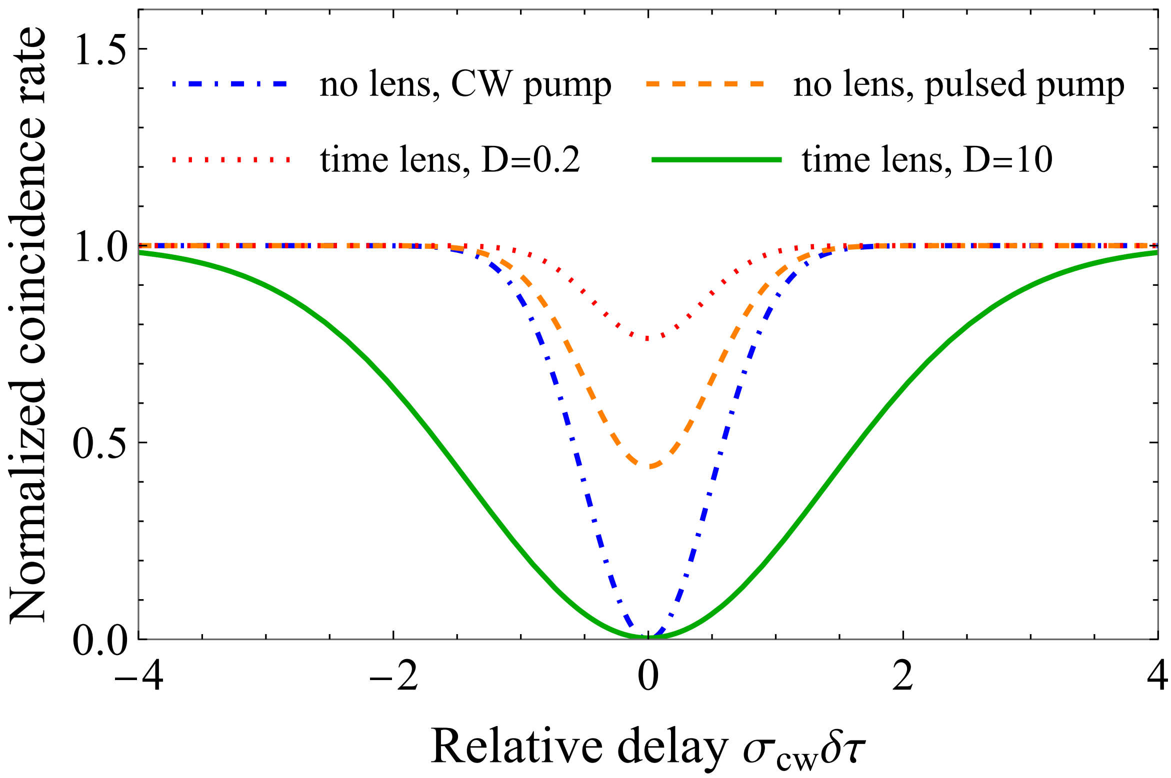

Figure 13: Normalized coincidence rate plotted against the relative delay. The source parameters are as in Section 2.1. The lines for a lensless case reproduce the well-known result: The pulsed pump reduces the visibility of Hong-Ou-Mandel interferometry [73–75]. A time lens with a low focal GDD is unable to restore the visibility, even at optimal magnification, because of the strong chirp, imposed on the magnified pulse. A time lens with a high focal GDD imposes a much weaker chirp and restores the visibility to 100%.

Substituting Eq. (149) into Eq. (146) and the result into Eq. (186), we obtain the visibility

$$V = \frac{2De^{-\gamma\delta t^2}}{|T_e - T_o|\sqrt{1 + M^2F_+F_-/D^2}}, \tag{157}$$

where

$$\gamma = \frac{2\Omega_p^2}{1 + T_o^2 + F_+}. \tag{158}$$

At high enough D, γ tends to 0 and the visibility approaches that of perfect synchronization, analyzed in the preceding section. The delay corresponding to the dip (149) takes a simple form in the limit $D \to \infty$:

$$\delta\tau_{\mathrm{min}} \to (1 - M)\delta t. \tag{159}$$

This result has a simple explanation. When the center of the single-photon pulse is delayed by $|\delta t|$ with respect to the time axis of the time lens with a magnification $M < 0$, the image pulse is shifted at the output by $|M\delta t|$ in the opposite direction (Figure 15), which

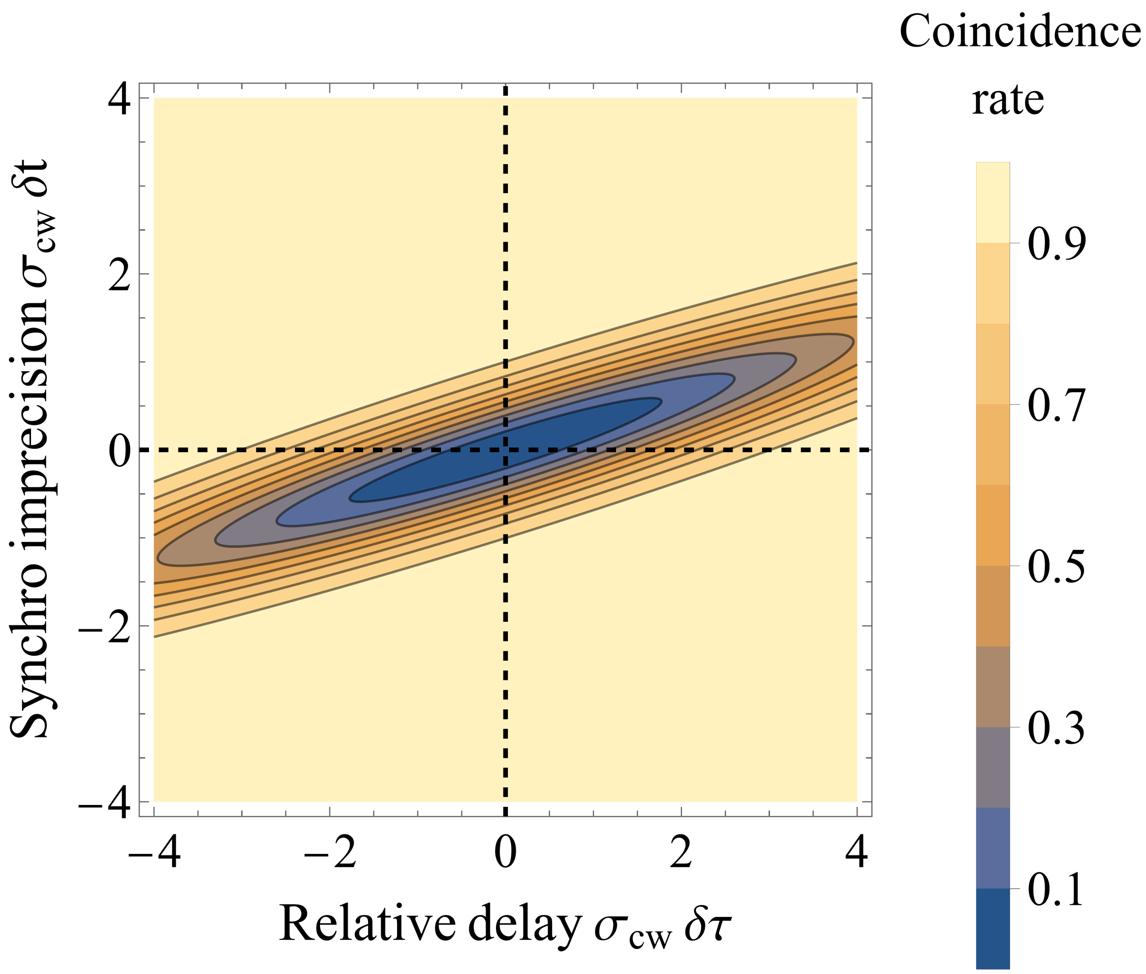

Figure 14: Normalized coincidence rate plotted versus the synchronization imprecision δt and the relative delay $\delta\tau$ measured in units of $\sigma_{\mathrm{cw}}^{-1}$. The source parameters are as in Section 2.1. The imaging system parameters are $D = 10$ and $M = -2.1$. The dashed axes illustrate that the coincidence rate is minimal for $\delta t = 0$ and $\delta\tau = 0$.

gives a total time shift of $(1 + |M|)|\delta t|$. This shift is to be compensated by a time delay, specified in Eq. (159). For a positive M, the image lies at the same side of the time axis with the object, and the total time shift is $|(1 - M)\delta t|$, again in agreement with Eq. (159).

The analysis of this section shows that, in general, the synchronization jitter reduces the visibility of the interference picture, but its effect can be greatly reduced by choosing a time lens with a sufficiently high focal GDD.

Properties of photons after the time lens

To make more intuitive the conclusions made above, let us consider the spectral and temporal shapes of two photons at position x_4 just before the output beam splitter of the interferometer and compare them to those found in Section 2.1. The extraordinary photon

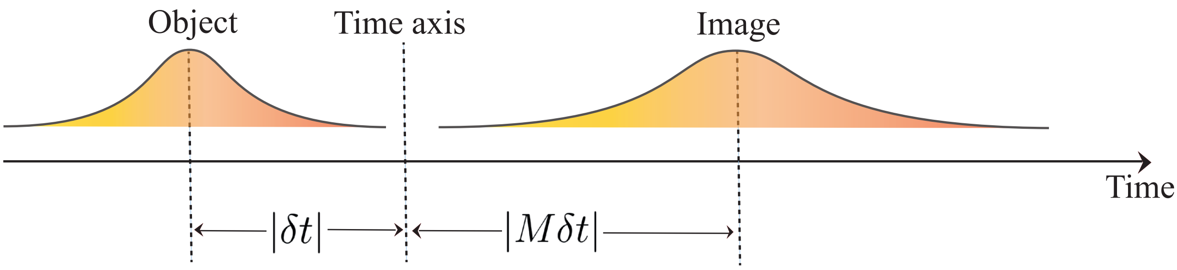

Figure 15: Schematic representation of the effect of a time lens on an input waveform in the case of imperfect synchronization of the source and the time lens. The waveform center has a time imprecision δt with the time axis of the lens. In the case of negative magnification, the output waveform is obtained by stretching $|M|$ times and inverting the input waveform. As a result, the magnified waveform experiences a time shift $(1 + |M|)|\delta t|$.

experiences just a delay, so its temporal and spectral widths are the same as at the crystal exit at position $x_1 = L$. In contrast, the ordinary photon, which passes through the time lens, changes both its temporal and spectral shapes. The intensity of the ordinary wave at x_4 is $I_o^{\text{out}}(t) = \langle \hat{E}_o^{(-)}(t, x_4)\hat{E}_o^{(+)}(t, x_4)\rangle$. Expressing the fields at x_4 through the fields at $x_1 = L$ by the relations given in Section 2.1, we find

$$I_o^{\text{out}}(t) = \frac{1}{|M|} I_o\left(\frac{t - t_{\text{delay}}}{M}\right), \tag{160}$$

where the delay time is $t_{\text{delay}} = t_{34} + t_{\text{out}} + Mt_{12} - Mt_{\text{in}}$. That is, the temporal width of the ordinary photon is increased $|M|$ times, as expected for a temporal imaging system with a magnification M.

To find the spectral shape of the ordinary photon we calculate the JSA at position x_4:

$$J_{\text{out}}(\Omega, \Omega') = \frac{1}{2\pi} \times \int \langle \hat{E}_o^{(+)}(t, x_4)\hat{E}_e^{(+)}(t', x_4)\rangle e^{i(\omega_0+\Omega)t+i(\omega_0+\Omega')t'} dt dt'. \tag{161}$$

Expressing the fields at x_4 through the fields at $x_1 = L$, as above, we obtain

$$J_{\text{out}}(\Omega, \Omega') = e^{i(k_e' L + t_z)\Omega'} \int G_o(\Omega, \bar{\Omega}) J(\bar{\Omega}, \Omega') \frac{d\bar{\Omega}}{2\pi}, \tag{162}$$

where

$$G_o(\Omega, \bar{\Omega}) = \sqrt{2\pi i D_{\text{f}}} e^{-\frac{i}{2} M D_{\text{f}} \left(\Omega - \frac{\bar{\Omega}}{M}\right)^2 + i\Omega\tau_2 + i\bar{\Omega}\tau_1 + i\phi'} \tag{163}$$

is the transfer function for the ordinary photon in the frequency domain. Here $\tau_2 = t_{\text{out}} + t_{34}$, $\tau_1 = k_o' L + t_{12} - t_{\text{in}}$, and $\phi' = \phi + k_e^0 L + \omega_0 t_z$. The transfer function satisfies the unitarity condition

$$\int G_o^*(\Omega, \Omega_1) G_o(\Omega, \Omega_2) \frac{d\Omega}{2\pi} = 2\pi\delta(\Omega_1 - \Omega_2). \tag{164}$$

As a consequence, the spectral and temporal shapes of the extraordinary photon, calculated from equations similar to Eqs. (103) and (111), remain unchanged except for a delay, as anticipated above.

The spectral width of the ordinary photon can be easily found in the limit $D_\mathrm{f} \to \infty$, where $G_o(\Omega, \bar{\Omega}) \to \frac{2\pi}{\sqrt{M}}\delta(\Omega - \bar{\Omega}/M)$ and

$$J_\mathrm{out}(\Omega, \Omega') \to \sqrt{M} J(M\Omega, \Omega'), \tag{165}$$

which means that the spectral width of the ordinary photon decreases $|M|$ times.

To find the spectrum of the ordinary photon in the general case of finite D_f, we perform a Gaussian modeling of the phase-matching function, as in Section 2.1. Substituting Eqs. (85), (100), and (105) into Eq. (162), we obtain

$$J_\mathrm{out}(\Omega, \Omega') = J_0 e^{-\frac{1}{4\Sigma^2}\left(B_{11}\Omega^2 + 2B_{12}\Omega\Omega' + B_{22}\Omega'^2\right) + i\psi(\Omega,\Omega')}, \tag{166}$$

where $B_{11} = D^2(1 + T_o^2)$, $B_{12} = D^2(1 + T_oT_e)/M$, and $B_{22} = D^2(1 + T_e^2)/M^2 + (T_e - T_o)^2(1 + T_o^2)$, while the values of J_0, Σ and $\psi(\Omega, \Omega')$ can be found by substituting Eqs. (85), (100) and (105) into Eq. (162) and taking a Gaussian integral with the help of Eq. (107), Eq. (166) with $\Sigma^2 = \Omega_p^2\left[(1 + T_o^2)^2 + D^2/M^2\right]$, $J_0 = \kappa L E_0 e^{i\phi'}\sqrt{2\pi i D_\mathrm{f}/(1 + T_o^2 + iD/M)}$ and

$$\begin{aligned}\psi(\Omega, \Omega') &= \tau_2(\Omega + \Omega') \\ &- \frac{D\left[M(1 + T_o^2)\Omega + (1 + T_oT_e)\Omega'\right]^2}{4M\Sigma^2}.\end{aligned} \tag{167}$$

The phase of the JSA, $\psi(\Omega, \Omega')$, becomes a symmetric function of its arguments in the limit $D \to \infty$, similar to the modulus of the JSA. We see that the spectral correlations (entanglement) between the photons are still present after the time lens, as indicated by the nonvanishing coefficient B_{12}.

The output JSA is evidently nonsymmetric at the optimal magnification, given by Eq. (153). Thus, the spectral widths of the photons are different at the optimal magnification for finite D_f. In the case $|D| > |T_o - T_e|$, the modulus of the output JSA can be made symmetric by choosing the magnification

$$M_\mathrm{sym} = \pm\frac{M_\mathrm{opt}}{\sqrt{1 - (T_e - T_o)^2/D^2}}, \tag{168}$$

which is, however, suboptimal.

Substituting Eq. (166) into Eq. (103), we obtain the spectrum of the ordinary photon after the time lens in a form of a Gaussian distribution with the dispersion

$$\sigma_{o,\mathrm{out}}^2 = \frac{\Omega_p^2}{D^2}\frac{\left[D^2/M^2 + (1 + T_o^2)^2\right](1 + T_o^2)\eta}{(1 + T_o^2)\eta - (1 + T_oT_e)^2/M^2}, \tag{169}$$

where $\eta = M_{\text{opt}}^2/M^2 + (T_e - T_o)^2/D^2$. At the optimal magnification and in the limit of high D, $\eta \to 1$ and $\sigma_{o,\text{out}} \to \sigma_o/|M| = \sigma_e$, as expected.

Thus, a single-lens temporal imaging system with a magnification M realizes a scaling of the field with the factor $|M|$ in the temporal domain: A pulse of duration Δt is stretched to the duration $|M|\Delta t$. However, in the spectral domain, the scaling factor is not given by $|M|$: A pulse of spectral width σ is transformed into a pulse with a spectral width higher than $\sigma/|M|$ because of an additional chirp imposed by the temporal imaging system. It is interesting that the highest visibility is attained at a magnification corresponding to equal durations of two photons, not to their equal spectral widths.

2.5 Summary

We have considered an application of a time lens for the light produced in a frequency-degenerate type-II SPDC pumped by a pulsed broadband source. In this type of SPDC, the signal and the idler photons have different spectral and temporal properties. Therefore, they lose their indistinguishability, and this effect deteriorates the visibility of the Hong-Ou-Mandel interference. We have demonstrated that by inserting a time lens in one of the arms of the interferometer and choosing appropriately its magnification factor one can achieve 100% visibility in the Hong-Ou-Mandel interference and, thus, restore perfect indistinguishability of the signal and idler photons.

In our theoretical model, we have taken into account the fact that for a pulsed source of the SPDC light one has to properly synchronize in time the source and the time lens in order to achieve the optimum destructive interference of the signal and the idler waves. We have studied the effect of desynchronization on the visibility of second-order interference. Our results show that for large values of the focal GDD of the lens, the effect of the desynchronization can be neglected and one can still have perfect visibility of the interference, however, for a nonzero time delay in the interferometric scheme.

In our calculations, we have assumed a Gaussian shape of the pump pulses for the SPDC source and also used a Gaussian approximation for the phase-mismatch function of the nonlinear crystal. These two conditions have allowed us to obtain several important analytical results, for example, for the spectra of the ordinary and the extraordinary waves and also for the temporal shapes of the emitted pulses. We have also obtained an analytical formula for the optimum value of the magnification factor of the time lens, which provides the unit visibility of the Hong-Ou-Mandel interference. We have given a simple physical interpretation of this result in terms of the temporal durations of the ordinary and the extraordinary pulses.

In order to assess the feasibility of our theoretical proposal in view of the possible experimental realizations, we have provided quantitative estimations for two possible implementations of the time lens: based on EOPM, and on FWM. Taking as an example a BBO crystal for the SPDC light source, we have shown that for both types of time lens our theoretical proposal is experimentally feasible, though for an EOPM-based time lens, the range of possible input bandwidths is much shorter than for a FWM-based time lens.

Chapter 3

Extending to time telescope

A very large part of space-time must be investigated, if reliable results are to be obtained.

– Alan Turing

A time lens never provides a pure scaling of the waveform, and a residual chirp is always present in the output, similar to the wavefront curvature imposed on the image by a single lens in spatial imaging. In the experiments, where the intensity of the output waveform is measured, this chirp is insignificant. However, when the output waveform is intended for further optical processing, as in a quantum network, its time-dependent phase may be of great importance. It is known, in particular, that even a slight distinguishability of photons used in boson sampling leads to classical simulability of the experimental results, destroying the quantum advantage [97, 98]. In the previous chapter, we studied the effect of the residual chirp on indistinguishability of two single-photon pulses whose durations are made equal by a single time lens and found that the residual chirp can be disregarded at rather high values of the focal group delay dispersion (GDD) of the time lens, which may be impractical, especially for an EOPM-based time lens. Thus, a truly noiseless temporal scaling of quantum fields requires the application of a two-time-lens system. As is shown below, the no-chirp condition implies a *telescopic condition* for a two-time-lens imaging system, i.e. the imaging system should be a *time telescope*.

Several particular cases of time telescope are studied in the literature [28–30, 35], all of them being *inverting*, where the output pulse (temporal image) is inverted in time and scaled replica of the input pulse (temporal object). Such an inverting time telescope has a spatial counterpart – Keplerian telescope [99, 100]. Surprisingly, the general case of a two-lens temporal imaging system was never considered. In this chapter, we fill this gap by developing a general theory of the time telescope. In particular, we show that a time telescope with a real erect (non-inverted) image can be easily built by choosing the negative sign for the output GDD. Such a time telescope has no spatial counterpart because the space-time analogy is incomplete: The dispersion can be positive or negative, while the diffraction is always positive. An erecting time telescope provides a pure temporal scaling of the input waveform, exactly what is necessary for a photonic-photonic interconnect in a quantum network.

A general two-lens temporal imaging system is studied in Sec. 3.1 and a no-chirp condition is deduced. Next, in Sec. 3.2 possible types of time telescopes are classified, and the conditions are found for a time telescope with minimal loss. In Sec. 3.3, we show how an erecting time telescope succeeds in making two photons, initially of very different durations, indistinguishable, by calculating the coincidence rate at the output of a Hong-Ou-Mandel interferometer.

3.1 General two-time-lens temporal imaging system

As discussed earlier, after the transformation by a time lens the output field $A_{\text{out}}(t)$ can be expressed via the input field $A_{\text{in}}(t)$ in a rather simple form

$$A_{\text{out}}(t) = \frac{1}{\sqrt{m}} e^{\frac{i}{2mD_{\text{f}}}t^2} A_{\text{in}}(t/m), \tag{170}$$

where $m = -D_{\text{out}}/D_{\text{in}}$ is the magnification. As we see, the output field intensity is a temporally scaled copy of the input field intensity, which is known as temporal imaging [16, 17]. We see also that the field amplitude, in addition to temporal scaling, has a chirp described by the term $e^{it^2/2mD_{\text{f}}}$, which corresponds in spatial imaging to wavefront curvature in the image plane. A more general expression for the field transformation by a non-ideal time lens can be found in Refs. [17, 46], where the last reference gives a unitary quantum transformation including the vacuum field added to the output due to a finite temporal aperture and a non-unit frequency conversion efficiency.

The chirp described by Eq. (170) may be highly undesirable in a quantum interconnect, preventing the achievement of indistinguishability of two waveforms from different sources as shown in Chapter 2. This chirp can be compensated by an additional dispersive medium when the input waveform is a Gaussian pulse. In the general case of an arbitrary input waveform, a second time lens is necessary for this purpose.

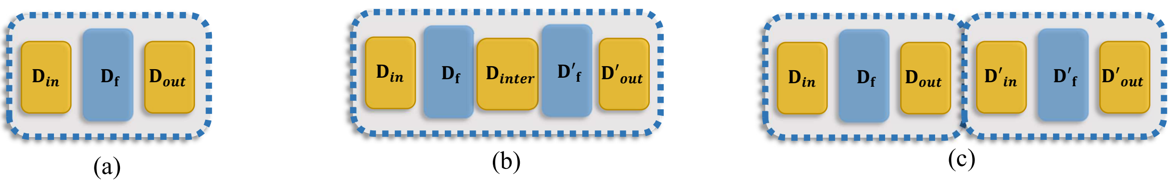

Figure 16: (a) Single-time-lens imaging system. Yellow boxes denote dispersive media with GDDs D_{in} and D_{out}, while the blue box denotes a time lens with the focal GDD D_{f}. (b) General two-time-lens imaging system with three dispersive elements. (c) Equivalent scheme of a general two-time-lens imaging system represented as a combination of two single-time-lens imaging systems with $D_{\text{out}} + D'_{\text{in}} = D_{\text{inter}}$.

Two time lenses

Now we consider a general two-time-lens imaging system, shown in Figure 16(b). It consists of two time lenses of focal GDDs D_f and D'_f, separated by a dispersive medium of GDD D_inter; the first time lens is preceded by a dispersive medium of GDD D_in, while the second one is followed by a dispersive medium of GDD D'_out. It is easy to see, that this system is equivalent to one shown in Figure 16(c). Indeed, let us find D_out from Eq. (64) and split the dispersive medium between the lenses into two sections with GDDs D_out and $D'_\mathrm{in} = D_\mathrm{inter} - D_\mathrm{out}$. The field between these sections $A_\mathrm{out}(t) = A'_\mathrm{in}(t)$ can be considered as the temporal image of the input field created by the first time lens and, at the same time, as the object for the second time lens. Similarly to Eq. (170), we write the field transformation by the second time lens as

$$A'_\mathrm{out}(t) = \frac{1}{\sqrt{m'}} e^{\frac{i}{2m'D'_\mathrm{f}}t^2} A'_\mathrm{in}(t/m'), \tag{171}$$

where $m' = -D'_\mathrm{out}/D'_\mathrm{in}$ is the magnification of the second time lens and the imaging condition is implied for the second lens similar to Eq. (64) but with primed GDDs. Using Eq. (170), we write,

$$A'_\mathrm{in}(t/m') = \frac{1}{\sqrt{m}} e^{\frac{i}{2mm'^2D_\mathrm{f}}t^2} A_\mathrm{in}(t/mm'). \tag{172}$$

Substituting Eq. (172) into Eq. (171) and taking into account the equality $A_\mathrm{out}(t) = A'_\mathrm{in}(t)$, we obtain the total field transformation in a two-time-lens imaging system

$$A'_\mathrm{out}(t) = \frac{1}{\sqrt{mm'}} \mathrm{e}^{i\frac{mm'D_\mathrm{f}+D'_\mathrm{f}}{2mm'^2D_\mathrm{f}D'_\mathrm{f}}t^2} A_\mathrm{in}\left(\frac{t}{mm'}\right). \tag{173}$$

We see, that the field at the output of a two-time-lens imaging system is a scaled version of its input field with a magnification $M = mm'$ and an additional chirp. This chirp is zero when $D'_\mathrm{f} = -MD_\mathrm{f}$, under which condition Eq. (173) reduces to

$$A'_\mathrm{out}(t) = \frac{1}{\sqrt{M}} A_\mathrm{in}(t/M). \tag{174}$$

Expressing m and m' through D_f, D'_f, D_in and D_inter via the imaging conditions of two time lenses, substituting the results into the no-chirp condition found above, and solving the obtained equation for D_inter, we obtain

$$D_\mathrm{inter} = D_\mathrm{f} + D'_\mathrm{f}, \tag{175}$$

which is equivalent to the telescopic (or afocal) condition in spatial imaging [99]. Thus, in order for a two-time-lens imaging system to be chirpless, it is necessary and sufficient that it is a time telescope.

A single-time-lens imaging system is characterized by two parameters, e.g. its input and focal GDDs, while the output GDD can be found from the imaging condition (64). Two such systems have four parameters, one of which can be found from the telescopic condition (175). Thus, a time telescope is determined by three real parameters, which can be chosen as M, D_{inter} and D_{in}. The first two parameters determine the type of telescope, while the third parameter determines the input GDD for the object field. The image is formed after the output GDD

$$D'_{\mathrm{out}} = -M^2 D_{\mathrm{in}} - M D_{\mathrm{inter}}. \tag{176}$$

We also find $D_{\mathrm{f}} = D_{\mathrm{inter}}/(1-M)$ and $D'_{\mathrm{f}} = -M D_{\mathrm{inter}}/(1-M)$.

Classification of time telescopes

Various types of time telescopes can be distinguished by the magnification M they provide. Some of these time telescopes have spatial counterparts and some do not because the space-time analogy is incomplete: In contrast to the diffraction, which is always positive, the dispersion can be positive or negative. We accept the convention that a time lens with a positive (negative) focal GDD corresponds to a convergent (divergent) spatial lens. As a consequence, a dispersive medium with a positive GDD corresponds to diffraction, which is always positive. A positive (negative) input or output GDD corresponds to a real (virtual) object or image respectively. The only parameter having no spatial counterpart is a negative D_{inter}, since the latter parameter corresponds to the telescope length, which cannot be negative.

Inverting magnifying time telescope, $M < -1$.

For a positive D_{inter}, we have $D'_{\mathrm{f}} > D_{\mathrm{f}} > 0$, which corresponds to a combination of two convergent lenses, where the second one has a higher focal length. In spatial imaging, such an imaging system is known as *beam expander*.

For a negative D_{inter}, we have $D'_{\mathrm{f}} < D_{\mathrm{f}} < 0$, which has no spatial counterpart. This would be a combination of two divergent lenses, which are unable to create a chirpless image for any distance between them.

Inverting compressing time telescope, $-1 < M < 0$

For a positive D_{inter}, we have $D_{\mathrm{f}} > D'_{\mathrm{f}} > 0$, which corresponds to a combination of two convergent lenses, where the first one has a higher focal length. In spatial imaging, such an imaging system is known as *Keplerian* or *astronomical telescope* [99, 100]. Compression in space corresponds to magnification in angular size, which is the aim of an astronomical observation. Similarly, a time telescope of this type can be used for spectral magnification. The image is inverted in this type of time telescope, which may be undesirable for quantum networks, as indicated above.

For a negative D_{inter}, we have $D_{\mathrm{f}} < D'_{\mathrm{f}} < 0$, which has no spatial counterpart.

Erecting compressing time telescope, $0 < M < 1$

For a positive D_{inter}, we have $D_{\text{f}} > 0$, $D'_{\text{f}} < 0$, $D_{\text{f}} > |D'_{\text{f}}|$, which corresponds to a combination of a convergent and divergent lens, where the first one has a longer focal length. In spatial imaging, such an imaging system is known as *Galilean* or *terrestrial telescope* [99, 100]. As in the previous case, compression in space corresponds to magnification in angular size. The image is erect in this type of time telescope, which makes it promising for photonic quantum networks.

For a negative D_{inter}, we have $D_{\text{f}} < 0$, $D'_{\text{f}} > 0$, $|D_{\text{f}}| > D'_{\text{f}}$, which has no spatial counterpart.

Erecting magnifying time telescope, $M > 1$

For a positive D_{inter}, we have $D_{\text{f}} < 0$, $D'_{\text{f}} > 0$, $|D_{\text{f}}| < D'_{\text{f}}$, which corresponds to a combination of a divergent and convergent lens, where the second one has a longer focal length. In spatial imaging, such an imaging system is known as *inverted Galilean telescope* [100], a Galilean telescope turned by the other side to the object.

For a negative D_{inter}, we have $D_{\text{f}} > 0$, $D'_{\text{f}} < 0$, $D_{\text{f}} < |D'_{\text{f}}|$, which has no spatial counterpart.

3.2 Time telescopes in photonic interconnects

Time telescopes studied in the literature

All time telescopes described in the literature up to date [28–30, 35] have spatial counterparts. The time telescope realized experimentally by Gaeta group [28–30] is inverting compressing, it was applied to temporal compression of digital optical signals [28], temporal pulse inversion [30], and spectral magnification [29]. It is a special case of the inverting compressing time telescope with $D_{\text{in}} = D_{\text{f}}$, and, as follows from Eq. (176), $D'_{\text{out}} = D'_{\text{f}}$. Such a time telescope creates a Fourier-transformed field between the time lenses and may be useful if a spectral manipulation of the signal is necessary. For pure temporal scaling, however, this time telescope is suboptimal, because it uses three dispersive media, while just two are enough, as is shown below.

The two-time-lens system studied analytically and numerically by Gauthier group [35] is based on the idea of using a temporal equivalent of the field lens: After the first single-time-lens system with positive D_{in} and D_{f}, one places the second time lens with $D'_{\text{f}} = -mD_{\text{f}}$, which dechirps the image. Since the second time lens is placed exactly where the first image is created, we have $D_{\text{inter}} = D_{\text{out}}$. It is easy to see that $D_{\text{out}} = D_{\text{f}}(1-m) = D_{\text{f}} + D'_{\text{f}}$, that is, this system satisfies the telescopic condition (175). This approach is equivalent to the limiting case $D'_{\text{in}} = \epsilon \to 0$, $D'_{\text{out}} = -\epsilon/(1-\epsilon/D_{\text{f}}) \to 0$, $m' \to 1$. This is a special case of application of the inverting magnifying time telescope, where the object is placed at the input GDD $D_{\text{in}} = -D_{\text{inter}}/M$ before the telescope, so that, according to Eq. (176), the image is created at $D'_{\text{out}} = 0$, which has an advantage of requiring one dispersive medium less.

Note, that though the paper of Christov [101] is titled *Theory of a 'time telescope'*, it considers a combination of a dispersive medium, represented by a pair of gratings, a parametric process with dispersed pump, and another dispersive medium. Such a combination can be considered as a two-time-lens system if the frequency is regarded as the counterpart of the transverse position. However, this system does not satisfy the telescopic condition and imparts a residual chirp on the output field. In the modern understanding of temporal imaging, where time is the counterpart of transverse position, the system of Ref. [101] is a single-parametric-time-lens imaging system.

Time telescope for quantum networks

A new type of time telescope, erecting compressing, i.e. having $0 < M < 1$, is proposed in this work. It is a temporal variant of the Galilean telescope and its scheme is shown in Figure 17. The principal difference with the Galilean telescope is that the latter creates a virtual image of a real object: We see from Eq. (176), that for a positive D_{in}, D'_{out} is always negative. In temporal imaging, however, the image is real, because the output GDD can be made negative.

In contrast to classical applications of temporal imaging, where high losses are typically tolerable, the losses in photonic quantum networks destroy the quantum coherence and should be minimized. For this purpose, one can consider a time telescope configuration with (i) a minimal number of dispersive media, which would minimize the insertion loss, and (ii) a minimal total modulus of GDD, which is typically connected to the total length of the dispersive media, and consequently, to total losses in them.

The minimal number of dispersive elements is obviously two: either D_{in} or D'_{out} can be made equal to zero. If we put $D_{\text{in}} = 0$, we have from Eq. (176) $D'_{\text{out}} = -MD_{\text{inter}}$, and the total dispersion modulus is $(1 + M)|D_{\text{inter}}|$. If we put $D_{\text{in}} = -D_{\text{inter}}/M$, as in the case of field lens of Ref. [35], we have from Eq. (176) $D'_{\text{out}} = 0$, and the total dispersion modulus is $(1 + 1/M)|D_{\text{inter}}|$. For an erecting compressing telescope with $0 < M < 1$, considered here, the first choice is preferable. Thus, we arrive at a configuration shown in Figure 18.

For a given M, the value $|D_{\text{inter}}| = (1 - M)|D_{\text{f}}|$ can be minimized by choosing $|D_{\text{f}}|$ as small as possible. We provide this optimization for an EOPM-based time telescope, assuming for definiteness $D_{\text{inter}} > 0$.

A great advantage of an EOPM-based time lens consists of the deterministic nature of the electrooptical effect, providing an almost lossless operation [37, 56]. Its main shortcoming is a rather short temporal aperture $T_A = \sqrt{AD_{\text{f}}}$ for the given focal GDD D_{f} and phase modulation amplitude A [13, 17]. This shortcoming is removed in the recently proposed Fresnel time lens [38], successfully applied to bandwidth compression of single photons [56]. The driving voltage in such a time lens is not sinusoidal, as in ordinary modulators, but represents a wrapped parabola, created by an arbitrary waveform generator. To create a phase shift $\phi = t^2/2D_{\text{f}}$ within the temporal aperture T_A, the modulator should realize the instantaneous circular frequency $\partial\phi/\partial t = t/D_{\text{f}}$ at times $t = \pm T_A/2$, i.e. its driving

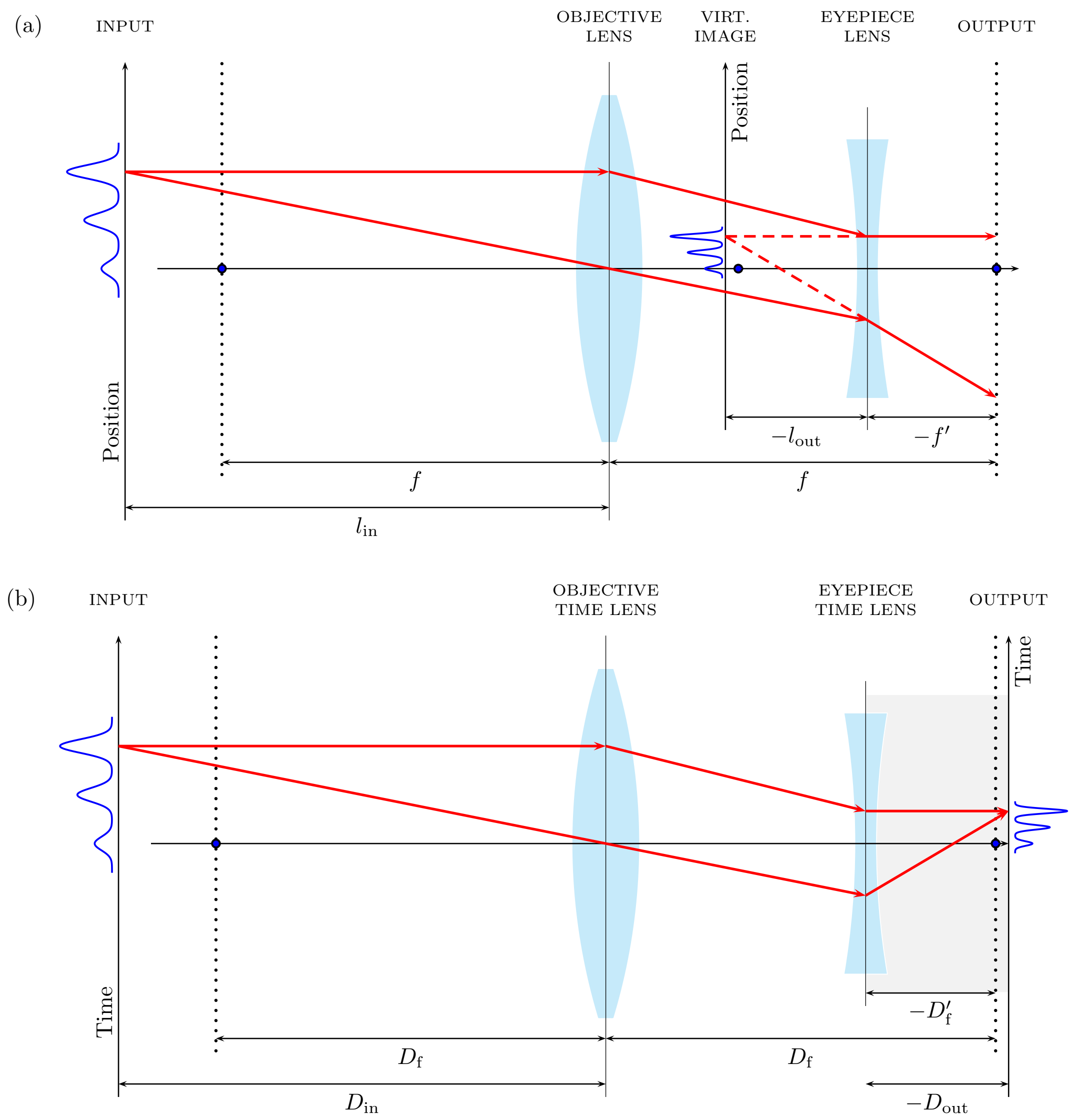

Figure 17: Galilean telescope and erecting compressing time telescope with the same magnification $M = 1/3$. (a) Galilean telescope is composed of two lenses with focal lengths $f > 0$ and $f' < 0$. When an object is placed at a distance $l_{\text{in}} > f$ before the objective lens, its virtual image is formed at the output distance $l_{\text{out}} < 0$. The geometrical light rays (red lines) show transformations of individual spatial frequency components in the imaging system. (b) Erecting compressing time telescope. The objective time lens has a focal GDD $D_{\text{f}} > 0$, while the eyepiece time lens has a focal GDD $D'_{\text{f}} < 0$, where the condition $D_{\text{f}} > |D'_{\text{f}}|$ is satisfied. The time rays (red lines) show transformations of individual frequency components in the imaging system: vertical position corresponds to time while the direction of the time ray corresponds to frequency [24]. The grey area shows a dispersive medium with a negative GDD, resulting in the creation of a real image at the output. This element is not possible in the spatial domain because negative diffraction does not exist while negative dispersion does.

voltage should have a bandwidth $\Omega_m = T_A/D_{\text{f}}$. Thus, for a Fresnel time lens, the temporal aperture scales linearly with the focal GDD: $T_A = D_{\text{f}}\Omega_m$, while the phase modulation amplitude is limited to 2π [38]. Now, if we wish to compress a pulse of full width at half

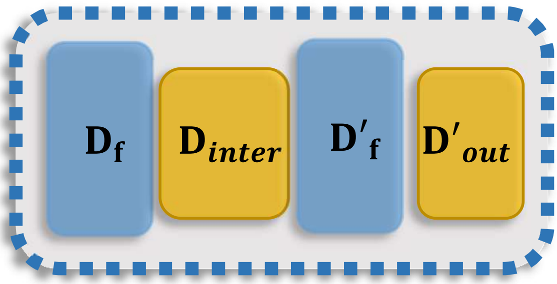

Figure 18: Erecting compressing time telescope with no input dispersive medium. Blue rectangles are time lenses and yellow ones are dispersive elements. The signs of D_f and $D'_\mathrm{f} = -MD_\mathrm{f}$ are opposite. The signs of $D_\mathrm{inter} = D_\mathrm{f} + D'_\mathrm{f}$ and $D'_\mathrm{out} = -MD_\mathrm{inter}$ are also opposite.

maximum (FWHM) duration T_0 to duration MT_0, we need to choose D_f big enough so that the temporal apertures of both time lenses surpass the pulse durations at their positions. We recall that Eqs. (123) and (124) are valid only under these conditions [16], otherwise including integrals over point-spread functions [46] similar to spatial imaging, where a point-spread function describes a limited resolution due to a finite lens aperture. Assuming a transform-limited Gaussian shape of the pulse, we calculate in the Appendix the temporal standard deviation Δt_2 of the pulse at the second time lens. Thus, we obtain the following inequalities: $T_0 \leq D_\mathrm{f}\Omega_m$ and $\sqrt{2\ln 2}\Delta t_2 \leq MD_\mathrm{f}\Omega'_m$, where Ω_m and Ω'_m are bandwidths of the first and second Fresnel time lenses respectively. The second of these inequalities can be satisfied (for practically interesting values $M \ll 1$) only for $\Omega'_m \geq \Omega_0/M$, where Ω_0 is FWHM spectral width of the input pulse, which has a simple physical explanation: the bandwidth of the second time lens should be at least equal to the bandwidth of the output pulse. Assuming $\Omega'_m = \Omega_0/M$, we obtain the minimal focal GDD of the first time lens as

$$D_\mathrm{f} = \frac{\sqrt{2M}T_0^2}{8\ln 2}. \tag{177}$$

Substituting this value into the first inequality, we obtain $\Omega_m \geq \Omega_0\sqrt{2/M}$, which again has a simple physical explanation: the bandwidth of the first time lens should be at least equal to the bandwidth of the signal after it, which is exactly $2\sqrt{2\ln 2}\Delta\Omega_1 = \Omega_0\sqrt{2/M}$ (see Appendix B).

Taking as an example the Fresnel time lens of Ref. [56] with $\Omega'_m/2\pi = 70$ GHz, we obtain the minimal output duration $MT_0 = 4\ln 2/\Omega'_m = 6.3$ ps. Let us consider a time telescope with $M = 0.003$ and a pulse of duration $T_0 = 2.1$ ns at the input. From Eq. (177) we obtain the value $D_\mathrm{f} = 61700$ ps^2, and, as a consequence, $D'_\mathrm{f} = -185$ ps^2. The input bandwidth is $\Omega_0/2\pi = 210$ MHz and, therefore, the minimal bandwidth of the first time lens is $\Omega_m/2\pi = 5.4$ GHz.

When the input pulse has a Gaussian temporal profile, a similar effect, temporal compression or spectral magnification, can be obtained by a much simpler system composed of one time lens and one dispersive medium of the same GDD [36–38, 56]. Such a system represents a temporal Fourier processor and can be used for stretching or compressing Gaussian pulses since they are eigenfunctions of the Fourier transform. For comparison, we calculate the bandwidth magnification ratio, achievable with the same resources by a Fourier transform based on a Fresnel time lens [38, 56]: $M_\Omega = D_f \Omega_m'^2 / 4 \ln 2 = 4300$, which is much higher than $1/M = 333$ in our example. However, in contrast to a Fourier processor, a time telescope provides temporal scaling for any shape of the input waveform.

Concluding this section, we notice, that an erecting magnifying time telescope is obtained by using the erecting compressing one, considered here, in the reverse order. Both types of telescopes can be used in photonic networks for stretching and compressing optical pulses as shown in Figure 19.

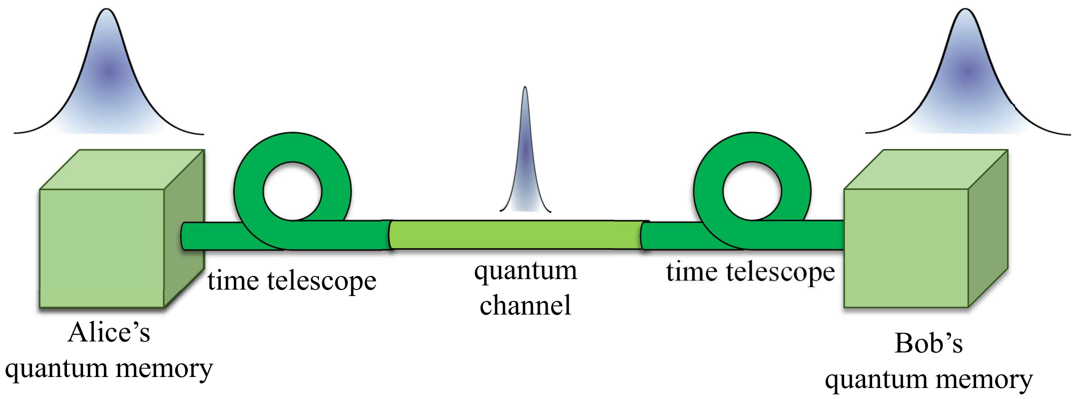

Figure 19: Time telescopes can play a prominent role in photonic networks by converting picosecond-scale pulses in the telecommunication band, optimal for high-rate fiber transmission, to nanosecond-scale pulses in the visible range processed by quantum memories. The pulses can be made identical leaving the encoded quantum information untouched.

3.3 Applications in different photonic networks

In this section, we describe possible applications of the erecting time telescope to reach the indistinguishability of single photons coming from different sources and having initially different temporal sizes. We consider the two most important sources of single photons: spontaneous parametric downconversion (SPDC) and a single quantum emitter such as a quantum dot. Similar to our previous work in Chapter 2, the quantum description of the field transformation is done in the Heisenberg picture, instead of the Schrödinger picture traditionally employed for such schemes [71, 73, 95, 102, 103], because the time-lens formalism is developed in the Heisenberg picture [45, 46]. In addition, the Heisenberg picture formalism provides a natural extension to the high-gain regime of parametric downconversion, where multiple photon pairs are created at once.

Parametric downconversion

As the first example, we consider an SPDC source of unentangled photon pairs. As the model crystal, we choose potassium-dihydrogen phosphate (KDP) crystal pumped at $\lambda_p = 415$ nm [37, 102], where a generation of separable photons was first demonstrated. Three waves propagate collinearly in the crystal, the strong undepleted extraordinary pump wave at the carrier frequency $\omega_p = 2\pi c/\lambda_p$ and two signal waves at the same carrier frequency $\omega_o = \omega_e = \omega_p/2$ generated spontaneously in the crystal: the ordinary and extraordinary. The interaction of these waves is most easily described in the Heisenberg picture in the spectral domain as discussed in Chapter 2.

The JSA and the phase-matching functions can be calculated numerically using Sellmeier equations for the ordinary $n_o(\omega)$ and extraordinary $n_e(\omega)$ refractive indices of KDP [104]

$$\tilde{n}_e^2(\lambda) = 2.26 + \frac{0.01}{\lambda^2 - 0.013} + \frac{13.005\lambda^2}{\lambda^2 - 400}, \tag{178a}$$

$$\tilde{n}_o^2(\lambda) = 2.133 + \frac{0.008}{\lambda^2 - 0.012} - \frac{3.228\lambda^2}{\lambda^2 - 400}, \tag{178b}$$

where λ is measured in micrometers, and writing $k_\mu(\Omega) = n_\mu(\omega_\mu + \Omega)(\omega_\mu + \Omega)/c$. Similar to the preceding chapter, we find the angle between the propagation direction and the optical axis of the crystal $\theta_p = 67.8°$, corresponding to the collinear degenerate type-II phase matching with $k_p^0 - k_o^0 - k_e^0 = 0$. The inverse group velocities of the pump and the ordinary wave coincide in this configuration: $k_p' = k_o'$, where k_μ' is the derivative of $k_\mu(\Omega)$ at $\Omega = 0$, which is known as asymmetric group velocity matching [78]. This means that the pump pulse and the ordinary photon exit the crystal simultaneously. The extraordinary photon, however, has a higher group velocity and advances them by the time $\tau_e = (k_p' - k_e')L/2 = 360$ fs, for a crystal of length $L = 5$ mm. Similar to Ref. [102], we consider a pump of spectral width 4.1 nm, which corresponds to $\tau_p = 62$ fs and $\Omega_p = 19$ rad/ps. The calculated JSA is shown in Figure 20.

We see from Figure 20, that when the sidelobes are filtered out, the JSA becomes separable and can be approximately written as

$$J(\Omega, \Omega') = \alpha_0 e^{-\Omega^2/4\Omega_p^2} e^{-\tau_e^2 \Omega'^2/2\sigma_s^2 + i\tau_e\Omega'}, \tag{179}$$

where we have made three approximations. The first one is the approximation of linear dispersion in the crystal [73, 95]: $k_\mu(\Omega) \approx k_\mu^0 + k_\mu'\Omega$, so that $\Delta(\Omega, \Omega') \approx \tau_e\Omega'$. The second one is the assumption that the width of the function $\mathrm{sinc}(\tau_e\Omega')$ is so small compared to the pump bandwidth, $\pi/\tau_e \ll \Omega_p$, that the dependence of the pump spectrum on Ω' can be disregarded, $\alpha(\Omega + \Omega') \approx \alpha(\Omega)$. The third approximation is the replacement of the $\mathrm{sinc}(x)$ function by a Gaussian function having the same width at half maximum, $e^{-x^2/2\sigma_s^2}$, where $\sigma_s = 1.61$ [90, 95].

The spectra of the ordinary and extraordinary photons $S_\mu(\Omega)$ can be obtained by integrating $|J(\Omega, \Omega')|^2$ over the frequency of the other photon (as shown in Chapter 2). Using the approximate JSA, Eq. (179), we obtain $S_\mu(\Omega) \propto \exp(-\Omega^2/2\sigma_\mu^2)$, where the spectral standard deviations are $\sigma_o = \Omega_p = 19$ rad/ps, $\sigma_e = \sigma_s/\sqrt{2}\tau_e = 3.15$ rad/ps.

The temporal shapes of the photons are given by their average intensities (in photon flux units) $I_\mu(t) = \langle \hat{E}_\mu^{(-)}(t, L)\hat{E}_\mu^{(+)}(t, L)\rangle$. With the help of the same approximations as above, $I_\mu(t) \propto \exp(-(t - t_\mu)^2/2\Delta t_\mu^2)$, where t_μ is some delay and the temporal standard

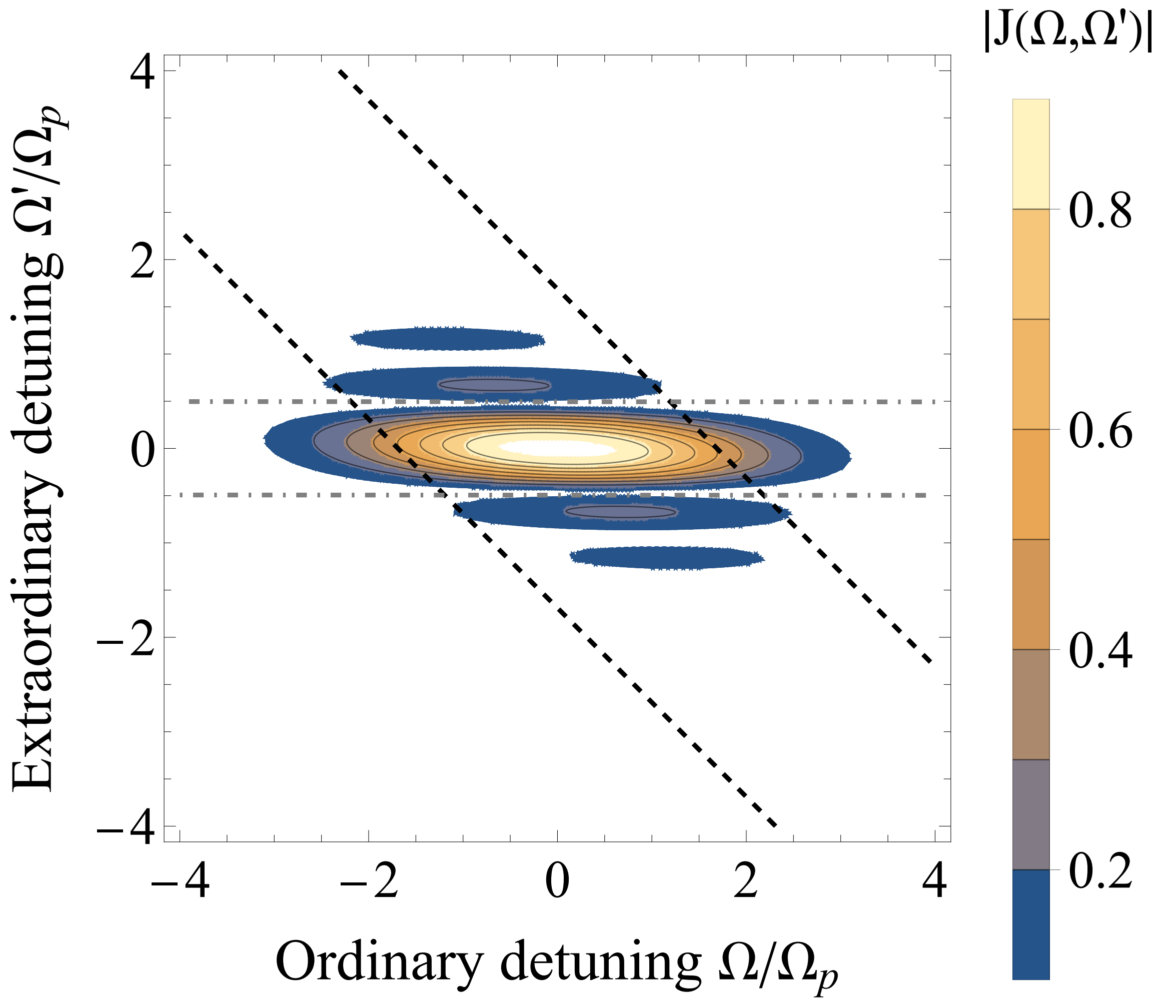

Figure 20: JSA of a photon pair generated by SPDC in a 5-mm-long KDP crystal pumped at 415 nm by pulses of spectral width 4 nm. The dashed lines delimit the pump envelope region. When the sidelobes are filtered out by a filter shown by the dot-dashed lines, the JSA becomes separable in two of its arguments.

deviations are $\Delta t_o = 1/2\Omega_p = 26$ fs, $\Delta t_e = \tau_e/\sqrt{2}\sigma_s = 158$ fs, which corresponds to FWHM widths $\Delta T_o = 2\sqrt{2\ln 2}\Delta t_o = 62$ fs and $\Delta T_e = 2\sqrt{2\ln 2}\Delta t_e = 373$ fs. We see that the ordinary photon has the same duration as the pump pulse; this is a consequence of the group velocity matching between these two waves. The ratio of the temporal widths of the extraordinary and ordinary photons is equal to the inverse of that of their spectral widths: $\gamma = \Delta t_e/\Delta t_o = \sigma_o/\sigma_e \approx 6$.

The duration of the ordinary photon can be made equal to that of the extraordinary one by an erecting magnifying time telescope, similar to the one described in the preceding section, but used in the reverse order. For this purpose, one needs to choose $M = 6$ and the input bandwidth corresponding to a 62-fs-long pulse. The latter is out of reach of any EOPM-based time telescope and a parametric one should be used. Since we are considering a frequency-degenerate source of single photons, it is important that the parametric time telescope has the same output carrier frequency as its input one: If the first time lens shifts the frequency, which is typical for SFG- or FWM-based time lenses, then the second time lens should shift it back. After the ordinary photon is stretched, it becomes indistinguishable from the ordinary one, and their Hong-Ou-Mandel interference (HOMI) [71] can be observed in an experiment, depicted in Figure 21.

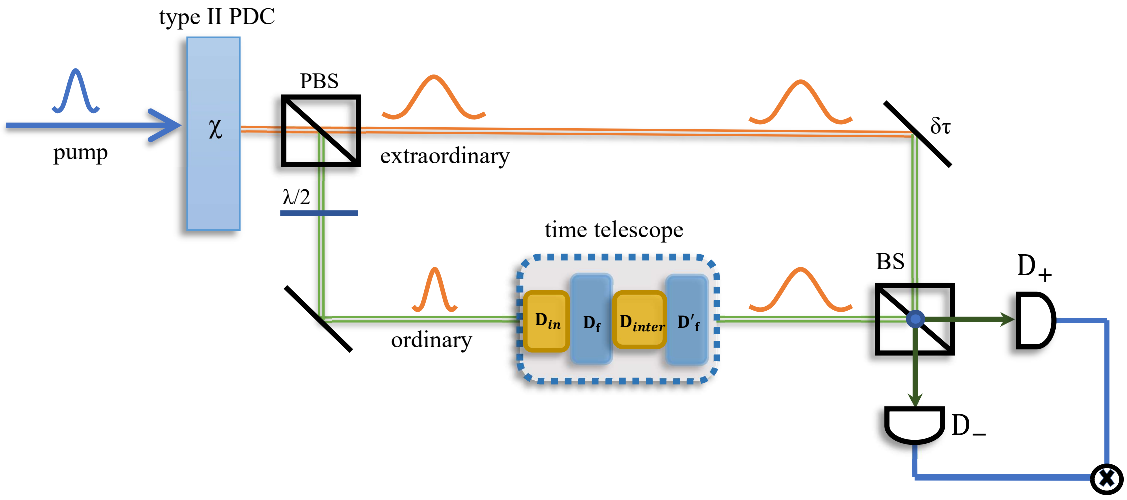

Figure 21: Scheme of the proposed experiment for observing a two-photon interference using a time telescope when the photons have different durations. A polarization beam splitter (PBS) is used to separate the ordinary and extraordinary photons produced in type-II SPDC with asymmetric group velocity matching. The ordinary photon is temporally stretched by the time telescope and then interferes with the extraordinary one (delayed by the time which can be adjusted by $\delta\tau$) on the beam splitter (BS), whose outputs are monitored by detectors D_+ and D_-. A coincidence is registered if both detectors click in the same excitation cycle.

The average coincidence rate is given by Eq. (129),

$$R_c(\delta\tau) = \frac{1}{T}\int_0^T\int_0^T dt_1 dt_2 \left|\langle E_-^{(+)}(t_2)E_+^{(+)}(t_1)\rangle\right|^2, \tag{180}$$

with the only difference that the field transformation in the temporal imaging system is given by Eq. (173) instead of (124):

Expressing the fields through the group-delayed envelopes, rewriting the time telescope transformation (174) as,

$$A_2(t) = A_1(t/M)/\sqrt{M}, \tag{181}$$

and assuming $B_2(t) = B_1(t - t_d)$, where t_d is the delay time in the extraordinary arm, we obtain

$$R_c(\delta\tau) = \frac{1}{4T|M|} \int \int_0^T dt_1 dt_2 \Bigg| \int U_B(t_2 - t_d, t') V_A\left(\frac{t_1}{M}, t'\right) dt' - \int U_A\left(\frac{t_2}{M}, t'\right) V_B(t_1 - t_d, t') dt' \Bigg|^2. \tag{182}$$

Substituting the solutions (98a) and (98b), applying the commutation relations $[A_0(t), A_0^\dagger(t')] = [B_0(t), B_0^\dagger(t')] = \delta(t - t')$, and equating to zero all normally ordered averages at $x_0 = 0$, the above expression reads

$$R_c(\delta\tau) = \frac{P_b}{2T}\left[1 - p_{\text{int}}(\delta\tau)\right], \tag{183}$$

where

$$p_{\text{int}}(\delta\tau) = \frac{|M|}{P_b} \int \int J_{\text{out}}(M\Omega, \Omega') J^*_{\text{out}}\left(M\Omega', \Omega\right) e^{i(\Omega - \Omega')(\delta\tau - t_d)} d\Omega d\Omega' \tag{184}$$

is the conditional probability of destructive interference of two photons under the condition that they are generated and $P_b = \int \left|J(\Omega, \Omega')\right|^2 d\Omega d\Omega'$ is the probability of biphoton generation per pump pulse. The JSA at the crystal output $J_{\text{out}}(\Omega, \Omega')$ differs from the JSA at its input by a phase (relative to the carrier wave) acquired by the photons during the dispersive propagation in the crystal: $J_{\text{out}}(\Omega, \Omega') = J(\Omega, \Omega') e^{i[k_o(\Omega) - k_o^0]L + i[k_e(\Omega') - k_e^0]L}$. The probability of destructive interference can be calculated analytically from the approximate JSA, Eq. (179), which gives

$$p_{\text{int}}(\delta\tau) = \frac{2\gamma|M|}{\gamma^2 + M^2} \exp\left(-\frac{2\Omega_p^2 \delta\tau^2}{\gamma^2 + M^2}\right), \tag{185}$$

where we have put the time delay in the extraordinary arm to $t_d = [(2M - 1)k_p' - k_e']L/2$, which provides the maximal interference probability at $\delta\tau = 0$.

As Eqs. (183) and (185) show, the coincidence rate has a dip at $\delta\tau = 0$. The HOMI visibility is defined as the ratio of the dip to the coincidence rate at a high delay:

$$V = \frac{R_c(\infty) - R_c(0)}{R_c(\infty)} = p_{\text{int}}(0). \tag{186}$$

This function is shown in Figure 22. It reaches the maximum value $V_{\max} = 1$ when $M = \pm\gamma$, i.e. when the magnification modulus is equal to the ratio of the temporal standard deviations of the extraordinary and ordinary photons. Note, that the sign of magnification is irrelevant in the case of symmetric in time pulses: the inverting time telescope is as good as the erecting one.

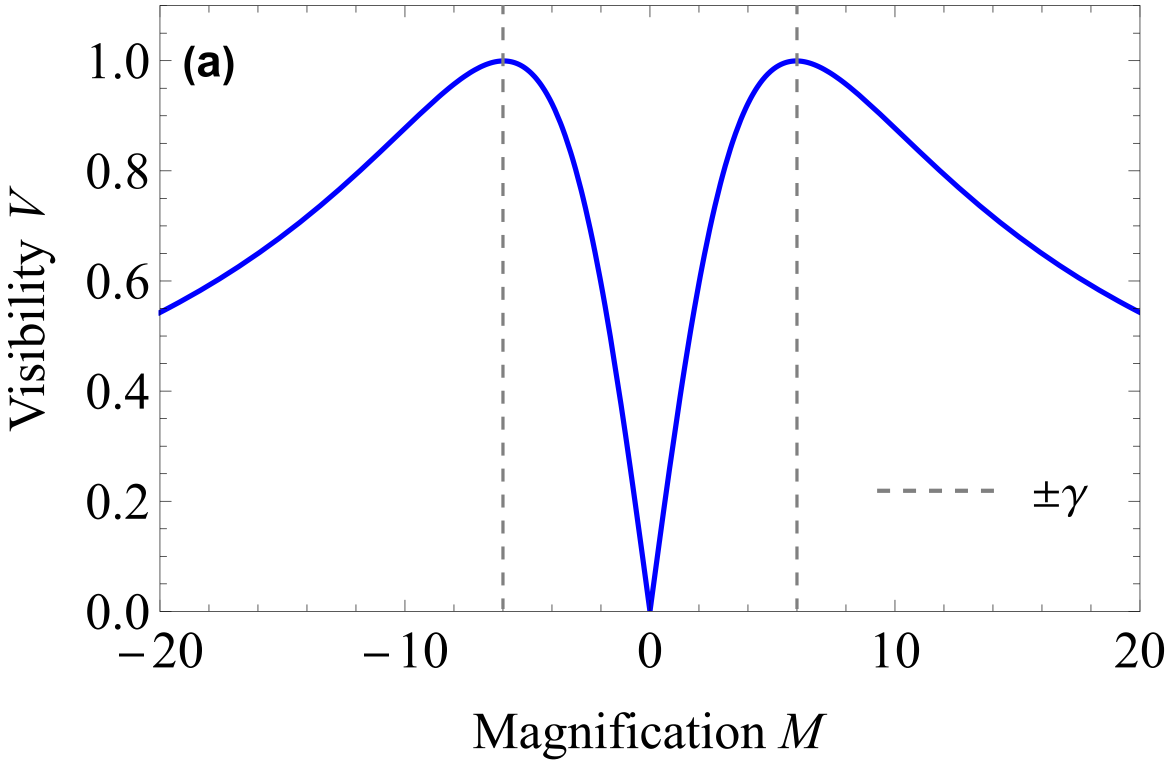

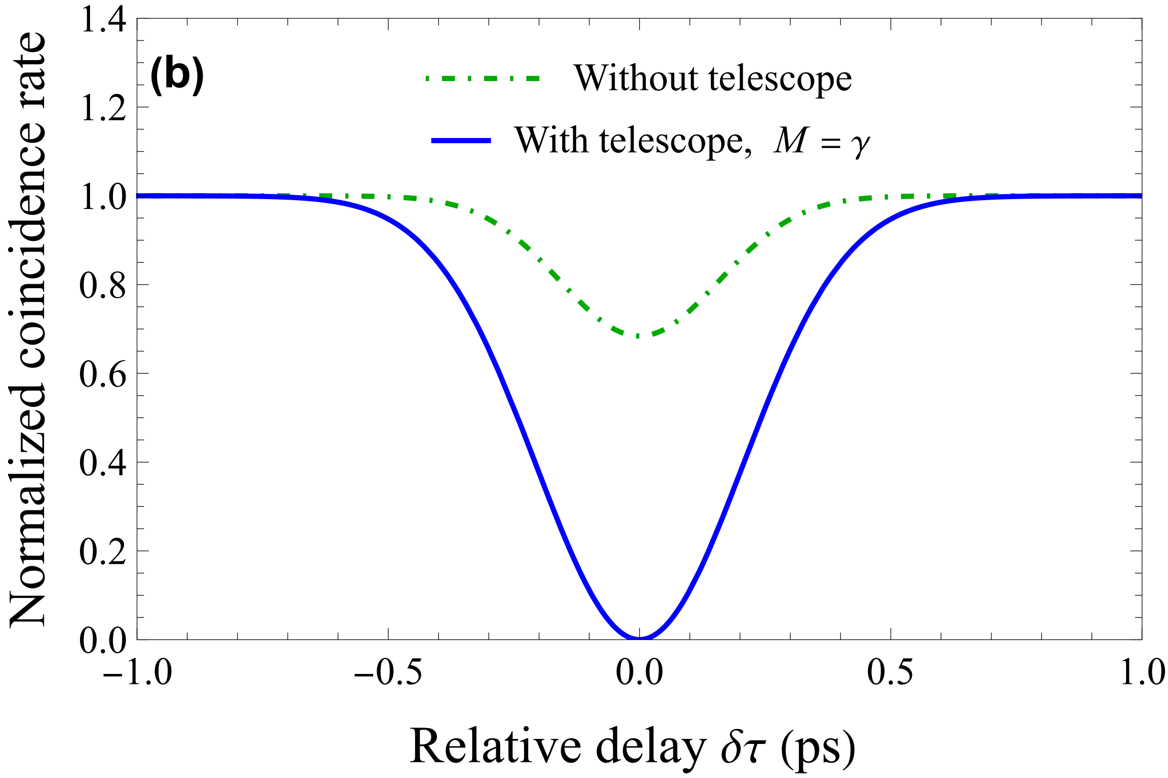

Figure 22: (a) HOMI visibility of two unentangled photons generated in a 5-mm-long KDP crystal pumped by pulses of 62 fs at 415 nm as a function of the time telescope magnification M. The visibility reaches the maximum at the optimal magnification $|M| = \gamma = \Delta t_e/\Delta t_o$ for both the erect and inverted images. (b) HOMI coincidence rate. Since the photons have highly different durations, the HOMI visibility is low without a time telescope. However, a time telescope applied to one of the photons can make the photons indistinguishable and achieve the unit HOMI visibility.

Single-photon source

As the second example, we consider two photons generated by single-photon sources, such as quantum dots [105, 106], with different radiative lifetimes and show how they can be made indistinguishable by a time telescope. The state of light emitted by a quantum dot with a radiative lifetime τ_i and a brightness μ_i $(i = 1, 2)$ can be written as [48, 106]

$$\rho_i = \int dt_1 \int dt_2 \psi_i(t_1)\psi_i^*(t_2)A_i^\dagger(t_1)|0\rangle\langle 0|A_i(t_2) + (1-\mu_i)|0\rangle\langle 0|, \tag{187}$$

where $A_i(t)$ is the annihilation operator for a photon at time t, while $\psi_i(t)$ defines the temporal mode of the emitted photon and is assumed to be a decaying exponential $\psi_i(t) = \sqrt{\mu_i/\tau_i}\exp(-t/2\tau_i)\theta(t)$, where $\theta(t)$ is the Heaviside step function. The limits of integration can be understood as infinite.

Let us suppose that the second source has a longer radiation lifetime, $\tau_2 > \tau_1$. Stretching the first photon by means of an erecting magnifying time telescope with a magnification M, we could expect that the photons become indistinguishable at $M = \tau_2/\tau_1$. In this case, they should result in a unit HOMI visibility in the setup depicted in Figure 23. Let us calculate this visibility assuming that the field emitted by the first source undergoes a transformation $A_1'(t) = A_1(t/M)/\sqrt{M}$ described by Eq. (174).

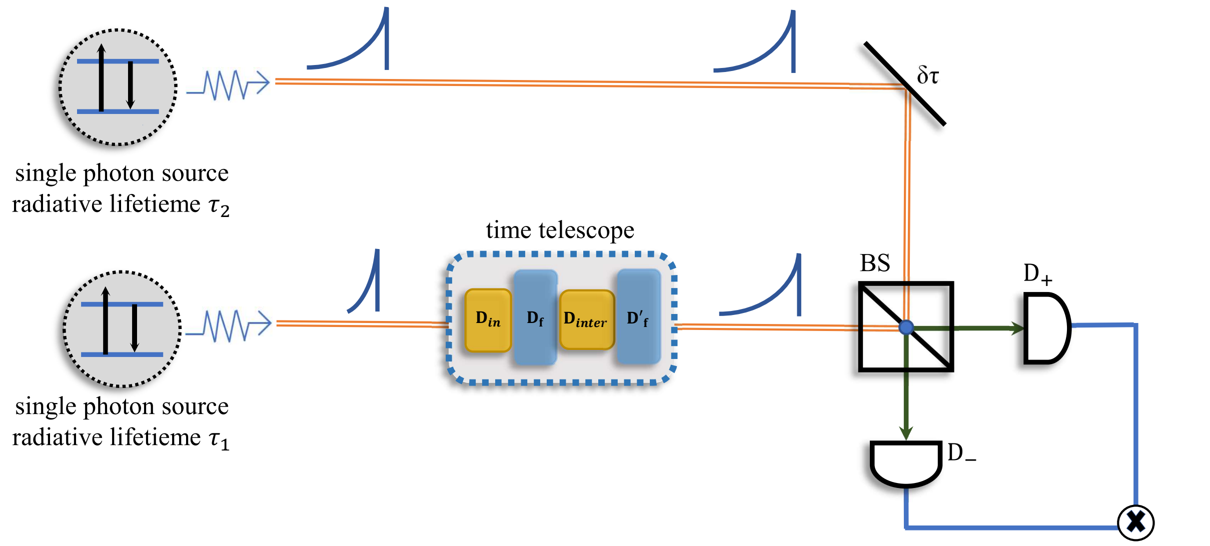

Figure 23: Schematic representation of the generation of two photons from individual sources and their second-order interference. Different radiative lifetimes $\tau_2 = 3\tau_1$ correspond to different shapes of the pulses produced by spontaneous emission. An erecting magnifying time telescope is used to stretch the first photon and observe the second-order interference.

Similar to the preceding section, we write the field at the detector $D_\pm$ as $C_\pm(t) = [A_1'(t) \pm A_2(t+\delta\tau)]/\sqrt{2}$, and the coincidence rate as

$$R_c(\delta\tau) = \frac{1}{T}\int dt \int dt' \mathrm{Tr}\left[C_+^\dagger(t)C_-^\dagger(t')C_-(t')C_+(t)\rho_1\rho_2\right]. \tag{188}$$

Substituting Eq. (187) into Eq. (188) and applying the commutation relations $[A_i(t), A_i^\dagger(t')] = \delta(t-t')$, we obtain the coincidence rate in the form of Eq. (183) (as shown in Appendix C) with the probability of photon pair generation $P_b = \mu_1\mu_2$ and the conditional probability of destructive interference $p_{\text{int}}(\delta\tau) = |c(\delta\tau)|^2/P_b$, where

$$c(\delta\tau) = \frac{1}{\sqrt{M}} \int \psi_1(t/M)\psi_2^*(t+\delta\tau)dt \tag{189}$$

is the temporal overlap of the stretched first and delayed second photons.

In the case of a positive magnification, $M > 0$, we obtain by substituting the explicit forms of the modal functions

$$p_{\text{int}}(\delta\tau) = \begin{cases} \frac{4M\tau_1\tau_2}{(M\tau_1+\tau_2)^2} e^{-\delta\tau/\tau_2}, & \text{if } \delta\tau \geq 0, \\ \\ \frac{4M\tau_1\tau_2}{(M\tau_1+\tau_2)^2} e^{\delta\tau/M\tau_1}, & \text{if } \delta\tau \leq 0, \end{cases} \tag{190}$$

and the visibility $V = p_{\text{int}}(0)$ is

$$V_{M>0} = \frac{4M\tau_1\tau_2}{(M\tau_1+\tau_2)^2}. \tag{191}$$

This function (see Figures 24(a) and 25(a)) reaches its maximum value 1 at $M = \tau_2/\tau_1$, which means that the optimal magnification is given by the ratio of the lifetimes, as anticipated above.

In the case of negative magnification, $M < 0$, we obtain

$$p_{\text{int}}(\delta\tau) = \frac{4|M|\tau_1\tau_2}{(|M|\tau_1-\tau_2)^2} \left(e^{-\delta\tau/2|M|\tau_1} - e^{-\delta\tau/2\tau_2}\right)^2 \theta(\delta\tau). \tag{192}$$

The maximal value of this function is reached at

$$\delta\tau_{\min} = \frac{2|M|\tau_1\tau_2}{|M|\tau_1-\tau_2} \ln\left(|M|\tau_1/\tau_2\right). \tag{193}$$

Thus, the visibility is

$$V_{M<0} = p_{\text{int}}(\delta\tau_{\min}) = 4\left(\frac{\tau_2}{|M|\tau_1}\right)^{\frac{|M|\tau_1+\tau_2}{|M|\tau_1-\tau_2}}. \tag{194}$$

This function (see Figures 24(a) and 25(a)) reaches its maximum at $M = -\tau_2/\tau_1$, where its value is $4e^{-2} \approx 0.54$. Substituting the optimal value of magnification into Eq. (192), we obtain

$$p_{\text{int}}(\delta\tau) = \left(\frac{\delta\tau}{\tau_2}\right)^2 e^{-\delta\tau/\tau_2}\theta(\delta\tau). \tag{195}$$

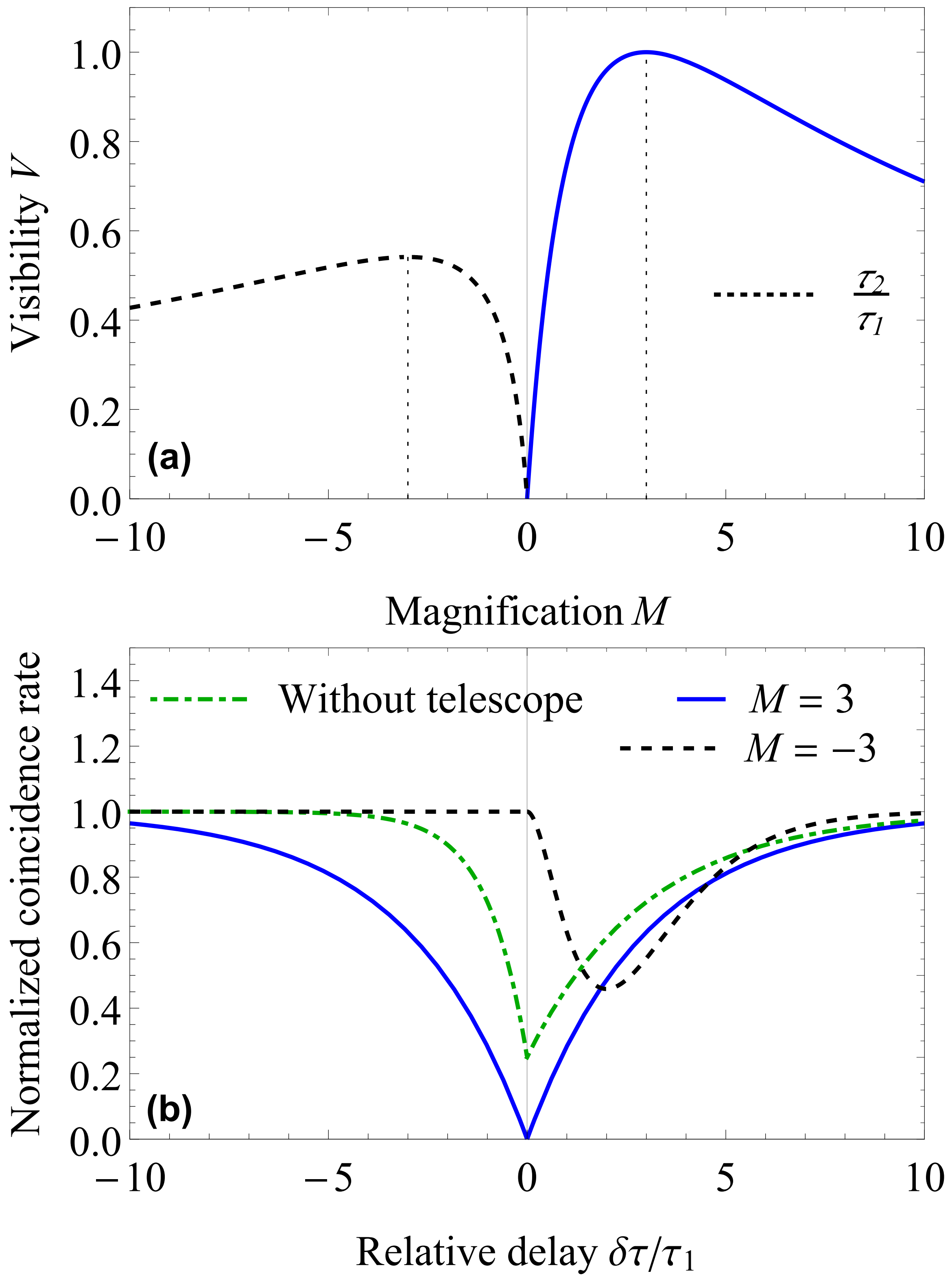

Figure 24: (a) HOMI visibility as a function of applied magnification. The inverting time telescope ($M < 0$) fails to reach the unit visibility, while the erecting one ($M > 0$) succeeds at $M = \tau_2/\tau_1 = 3$. (b) Normalized coincidence count rate plotted against the relative delay for different values of magnification. The erecting time telescope ($M = 3$) performs much better than the inverting one ($M = -3$).

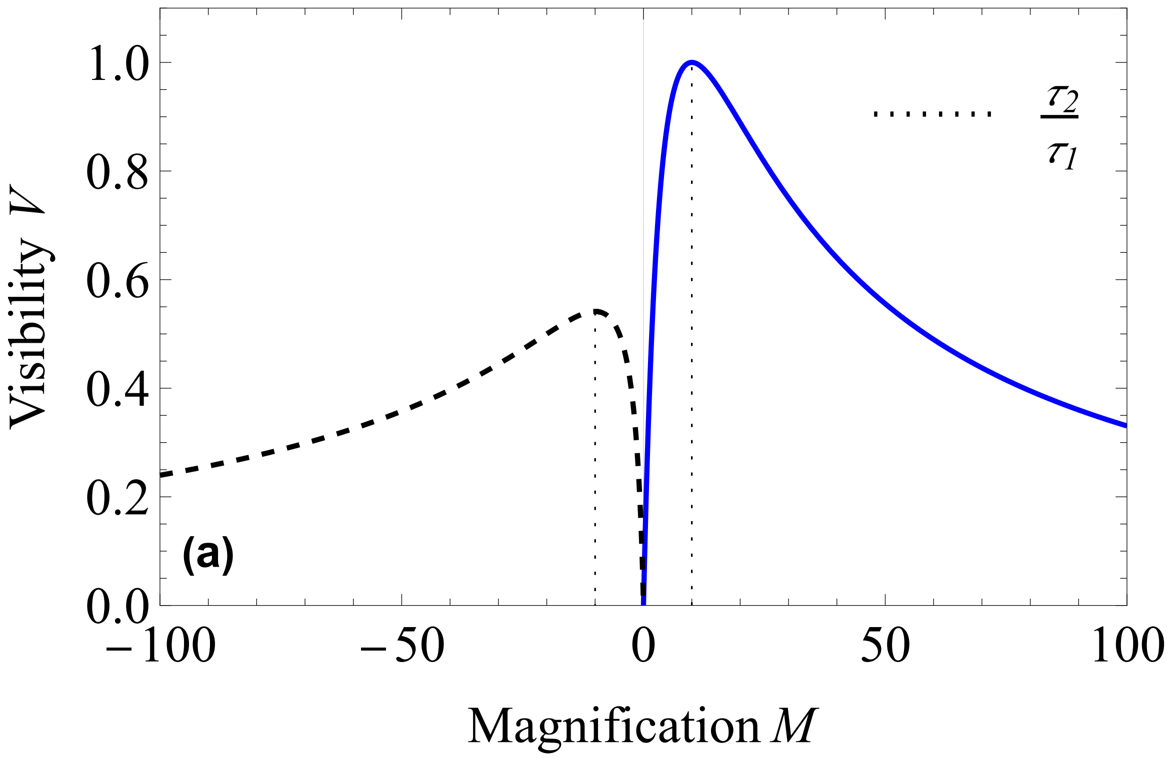

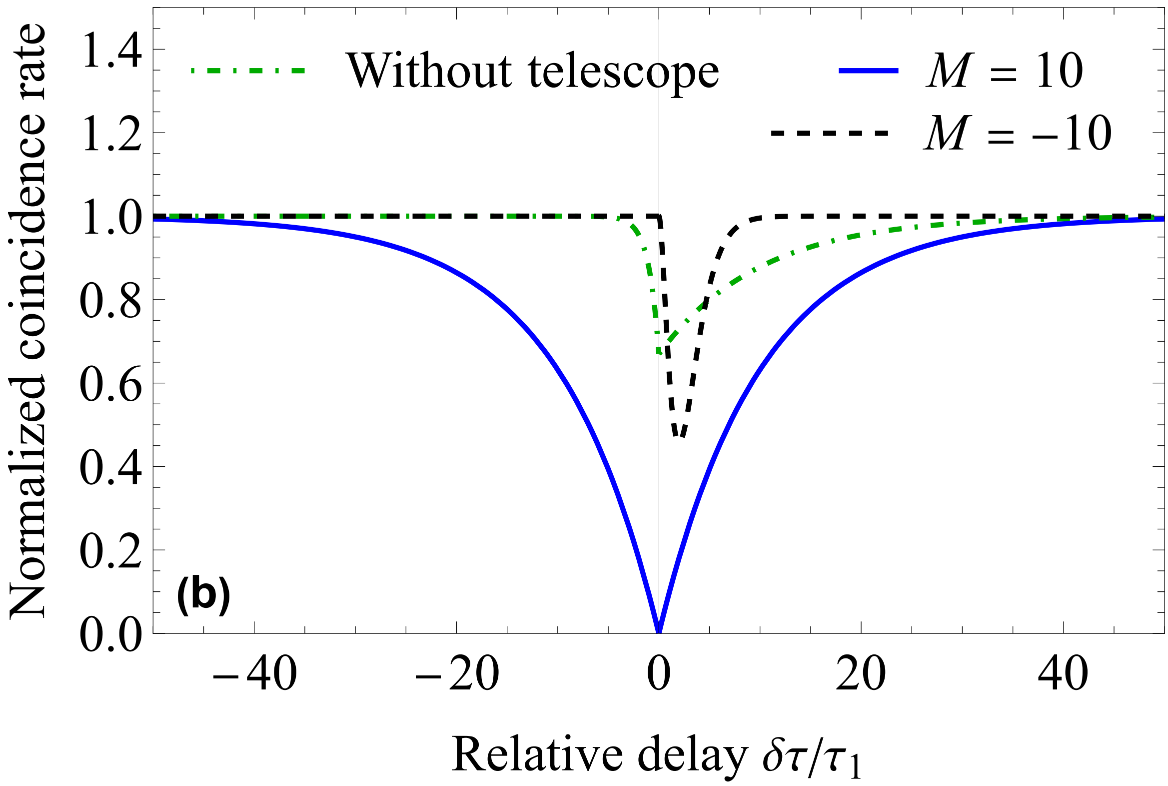

Figure 25: Plots similar to Figure 24 for $\tau_2/\tau_1 = 10$.

The coincidence rate calculated from Eq. (183) with $p_{\mathrm{int}}(\delta\tau)$ calculated above is shown in Figures 24(b) and 25(b). We see that the erecting time telescope outperforms significantly the inverting one, when applied to non-symmetric single-photon pulses, such as decaying exponentials typical to single-photon emitters. The maximal HOMI visibility reachable with an inverting time telescope is limited to $4e^{-2} \approx 0.54$ for any ratio of the emitters' lifetimes because the shape of the emitted pulses is not time-symmetric. In contrast, the erecting time telescope provides unit visibility at optimal magnification.

3.4 Summary

In this chapter, we have developed a general theory of a time telescope created by two time lenses and shown that minimal losses are reached when just two dispersive media are used. We have also shown that an erecting time telescope can be built by using two time lenses with opposite signs of their focal GDDs. In contrast to the spatial Galilean telescope, this device creates a real erect image and can be used in photonic quantum networks for pure temporal scaling of optical fields, not accompanied by residual temporal chirp.

We have considered two examples of the application of such a time telescope to distinguishable photons produced by SPDC and single emitters such as quantum dots and shown that in both cases the photons can be made perfectly indistinguishable by means of an erecting time telescope. Recent research shows that both time lenses and dispersive elements can be realized on an integrated photonic chip with very low losses [107], which opens up bright perspectives for applications of time telescopy to realizations of quantum photonic-photonic interconnects.

Chapter 4

Intensity correlations and Schmidt-mode decompositions

For the rest of my life I will reflect on what light is.

– Albert Einstein

High-dimensional quantum state engineering requires higher-dimensional Hilbert space of the quantum states for information encoding with the multi-mode Gaussian states of light being the most promising candidates for quantum information and quantum metrology purposes [108, 109]. Spatiotemporal degrees of freedom displaying entanglement allow us to have multiple approaches for this task to become competitive with the present quantum computing race. One of the most successful approaches to estimating the number of temporal modes makes use of Schmidt decomposition, however, it portrays experimental limitations. This demands a new way to count the temporal modes of light fields using classical coherence. In this chapter, we demonstrate how the temporal width of the second-order autocorrelation function measured in this way can be used for a precise determination of the number of Schmidt modes in PDC.

This Chapter is structured in the following way: In Section 4.1, we study the correlation functions of PDC-generated photon pairs and understand how the time-stretched autocorrelation function resolves the possibility of photodetection by modern photodetectors. In Section 4.2 we give an analytical expression for the second-order autocorrelation function in the low-gain regime of PDC with a Gaussian modeling of the phase-matching function. Finally, we illustrate the different limiting cases of the general formalism by considering a symmetric group velocity matching in a periodically poled KTP crystal and an asymmetric group velocity matched KDP crystal in Section 4.3.

4.1 Correlation functions

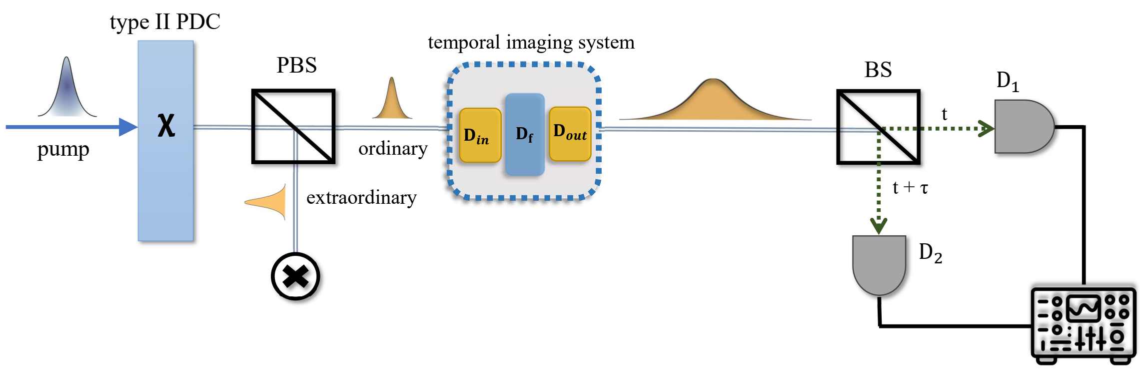

Figure 26: Scheme for generation of photon pairs and detection of their second-order correlation function. A pump pulse impinges on a nonlinear crystal cut for type-II collinear PDC. Two subharmonic pulses appear as ordinary and extraordinary waves in the crystal. The pump is removed, while two subharmonic pulses are separated by a polarized beam splitter (PBS). Afterwards, the ordinary pulse passes through a temporal imaging system, composed of an input dispersive medium, a time lens, and an output dispersive medium. The stretched ordinary pulse is split by a beam splitter (BS) and detected by photodetectors D_1 and D_2. The second-order autocorrelation function of the ordinary wave is obtained from the records of both photodetectors.

From the field transformation in the crystal, Eqs. (98a) and (98b), we find that the mean field of the generated light is zero: $\langle A_1(t)\rangle = \langle B_1(t)\rangle = 0$. The field obtained from the vacuum employing a Bogoliubov transformation is known to possess Gaussian statistics, which means that its higher-order moments are expressed via its second-order moments [51]. Thus, all correlation functions can be obtained from the first-order ones: the normal autocorrelator and crosscorrelator $\left\langle \hat{E}_\mu^{(-)}(L,t)\hat{E}_\mu^{(+)}(L,t)\right\rangle$ and $\left\langle \hat{E}_o^{(-)}(L,t)\hat{E}_e^{(+)}(L,t)\right\rangle$ respectively, and anomalous autocorrelator and crosscorrelator $\left\langle \hat{E}_\mu^{(+)}(L,t)\hat{E}_\mu^{(+)}(L,t)\right\rangle$ and $\left\langle \hat{E}_o^{(+)}(L,t)\hat{E}_e^{(+)}(L,t)\right\rangle$ respectively. For the field generated in a type-II PDC, the normal crosscorrelator and anomalous autocorrelation are identically zero, as can be easily found from Eqs. (98a) and (98b). The anomalous crosscorrelator, also known in the low-gain regime as biphoton amplitude, plays a central role in the description of entanglement between the generated photons and will be considered later. The only correlator to be calculated in this section is the normal autocorrelator of the ordinary wave, $\left\langle \hat{E}_o^{(-)}(L,t)\hat{E}_o^{(+)}(L,t)\right\rangle$.

The second-order autocorrelation function of the ordinary wave is defined as [50]

$$g^{(2)}(\tau) = \frac{\left\langle E_o^{(-)}(L,t)\, E_o^{(-)}(L,t+\tau)E_o^{(+)}(L,t+\tau)E_o^{(+)}(L,t)\right\rangle}{\left\langle E_o^{(-)}(L,t)E_o^{(+)}(L,t)\right\rangle \left\langle E_o^{(-)}(L,t+\tau)E_o^{(+)}(L,t+\tau)\right\rangle}, \tag{196}$$

and is measured typically by a Hanbury Brown and Twiss setup shown in Figure 26, which involves the detection of single photons and a record of the time intervals between successive photon detections.

The numerator of Eq. (196) is expressed via first-order correlators by the Gaussian moment factoring theorem [51] (we omit the position L for simplicity),

$$\begin{aligned}\langle E_o^{(-)}(t)E_o^{(-)}(t+\tau)E_o^{(+)}(t+\tau)E_o^{(+)}(t)\rangle &= \langle E_o^{(-)}(t)E_o^{(+)}(t)\rangle\langle E_o^{(-)}(t+\tau)E_o^{(+)}(t+\tau)\rangle \\ &+ |\langle E_o^{(-)}(t)E_o^{(+)}(t+\tau)\rangle|^2 + |\langle E_o^{(+)}(t)E_o^{(+)}(t+\tau)\rangle|^2.\end{aligned} \tag{197}$$

Upon discarding the last term, the anomalous autocorrelation being identically equal to zero, and substituting the rest into Eq. (196), we obtain

$$g^{(2)}(\tau) = 1 + \left|g^{(1)}(\tau)\right|^2, \tag{198}$$

where

$$g^{(1)}(\tau) = \frac{\left|G^{(1)}(t,\tau)\right|}{\left[I_o(t)I_o(t+\tau)\right]^{1/2}}, \tag{199}$$

is the normalized first-order correlation function [50]. Here, we have introduced the non-normalized first-order correlation function $G^{(1)}(t,\tau) = \left\langle E_o^{(-)}(L,t)\, E_o^{(+)}(L,t+\tau)\right\rangle$ and the ordinary wave intensity (in the photon-flux units) $I_o(t) = G^{(1)}(t,0)$.

Substituting Eq. (98a) into the definition of $G^{(1)}(t,\tau)$, we obtain

$$G^{(1)}(t,\tau) = e^{-\omega_o\tau}\int V_o^*(t,t')V_o(t+\tau,t')\mathrm{d}t'. \tag{200}$$

This function will be calculated analytically in the low-gain regime of PDC in Section 4.2.

Time-stretched autocorrelation function

Picosecond-scale pulses of light generated by PDC in typical nonlinear crystals are impossible to resolve by modern photodetectors. In previous chapters, we studied the possibility of stretching the field envelope of the ordinary wave through a temporal imaging system. We also discussed how a single-lens temporal imaging system always imparts a chirp on the field amplitude and how a two-lens temporal imaging system can eliminate it, however, in the direct detection case considered here, it is unimportant.

The non-normalized first-order correlation function for the field after the temporal imaging system is $G^{(1)}_{\mathrm{im}}(t,\tau) = \left\langle E_o^{(-)}(z_d,t)\, E_o^{(+)}(z_d,t+\tau)\right\rangle$ where z_d is the position after the temporal imaging system. The modulus of this function is just a scaled and delayed version of the modulus of the function $G^{(1)}(t,\tau)$ analyzed in the previous section:

$$\left|G^{(1)}_{\mathrm{im}}(t,\tau)\right| = \frac{1}{|M|}\left|G^{(1)}(t'/M,\tau/M)\right| \tag{201}$$

where $t' = t-\tau_g$ is the group delayed time and τ_g is the group delay in all the elements of the temporal imaging system. It means that for a sufficiently large magnification $|M|$, both the mean intensity $\left|G^{(1)}_{\mathrm{im}}(t,0)\right|$ and the normalized second-order autocorrelation function $g^{(2)}_{\mathrm{im}}(\tau) = g^{(2)}(\tau/M)$ can be brought to the time scale surpassing the resolution time of the photodetectors.

4.2 The second-order autocorrelation function

We studied in Section 2.1 the transformation of optical quantum fields from a nonlinear crystal input face to its output one. In this context, we write this transformation in a compact form, we define the group-delayed envelopes: $E^{(+)}_o(L,t) = A_{1d}(t-k'_0L-\tau_o)e^{ik^0_oL-i\omega_o t}$ and $E^{(+)}_e(L,t) = B_{1d}(t-k'_0L-\tau_e)e^{ik^0_eL-i\omega_e t}$. In this notation, the field transformation in the crystal has the form

$$A_{1d}(t) = A_{0d}(t) + \int \tilde{J}_0(t,t')B^{\dagger}_{0d}(t')\mathrm{d}t', \tag{202a}$$

$$B_{1d}(t) = B_{0d}(t) + \int \tilde{J}_0(t',t)A^{\dagger}_{0d}(t')\mathrm{d}t', \tag{202b}$$

where $A_{0d}(t) = A_0(t+\tau_o)$ and $B_{0d}(t) = B_0(t+\tau_e)$ are delayed vacuum fields and the zero-centered joint temporal amplitude (JTA) of two generated photons $\tilde{J}_0(t,t')$ is the double Fourier transform of their phase-shifted JSA $J_0(\Omega,\Omega') = J(\Omega,\Omega')e^{-i(\tau_o\Omega+\tau_e\Omega')}$:

$$\tilde{J}_0(t,t') = \int\int J_0(\Omega,\Omega')e^{-i\Omega t-i\Omega' t'}\frac{\mathrm{d}\Omega\mathrm{d}\Omega'}{(2\pi)^2}. \tag{203}$$

The first-order autocorrelation function of the delayed ordinary wave is

$$G^{(1)}_d(t,\tau) = \left\langle A^{\dagger}_{1d}(t)A_{1d}(t+\tau)\right\rangle = \int \tilde{J}^*_0(t,t')\tilde{J}_0(t+\tau,t')\mathrm{d}t'. \tag{204}$$

The function introduced in Section 4.1 differs from it by a delay and a phase: $G^{(1)}(t,\tau) = G^{(1)}_d(t-k'_oL-\tau_o,\tau)e^{-i\omega_o\tau}$. Thus, below we will calculate the delayed function, which carries all necessary information on the field coherence. The correspondingly delayed intensity is denoted as $I_d(t) = G^{(1)}_d(t,0)$.

Gaussian modeling

Both JSA and JTA can be significantly simplified by approximating them with double Gaussian functions. Upon substituting Eqs. (85) and (105) into (100), the JSA becomes a double Gaussian function

$$J_0(\Omega,\Omega') = \kappa L\alpha_0 \exp\left[-\frac{(\Omega+\Omega')^2}{4\Omega_p^2} - \frac{(\tau_o\Omega+\tau_e\Omega')^2}{2\sigma_s^2}\right]. \tag{205}$$

Substituting it into Eq. (203) and applying the multidimensional Gaussian integration technique Eq. (138), we obtain the JTA also in the form of a double Gaussian function

$$\tilde{J}_0(t,t') = J_1 e^{-M_{11}t^2-M_{22}t'^2-2M_{12}tt'}, \tag{206}$$

where $J_1 = \kappa L\alpha_0\Omega_p^2/\pi|T_o - T_e|$, $T_\mu = \sqrt{2}\Omega_p\tau_\mu/\sigma_s$, and $M_{i,j}$ are the elements of the matrix

$$\mathbf{M} = \frac{\Omega_p^2}{(T_o-T_e)^2}\begin{pmatrix} 1+T_e^2 & -1-T_oT_e \\ -1-T_oT_e & 1+T_o^2 \end{pmatrix}. \tag{207}$$

Inserting Eq. (206) into Eq. (204) and performing the integration (see Appendix D), we obtain

$$G_d^{(1)}(t,\tau) = \left[I_d(t)I_d(t+\tau)\right]^{1/2}\ e^{-\tau^2/2\Delta\tau_o^2}, \tag{208}$$

where the mean intensity of the ordinary wave is,

$$I_d(t) = \frac{P_b}{\sqrt{2\pi}\Delta t_o}e^{-t^2/2\Delta t_o^2} \text{ and} \tag{209a}$$

$$P_b = \frac{(\kappa L\alpha_0\Omega_p)^2}{2\pi|T_e-T_o|}, \tag{209b}$$

is the biphoton generation probability per pump pulse introduced in previous chapters. Moreover, the standard deviation of the mean intensity is,

$$\Delta t_o = \frac{\sqrt{1+T_o^2}}{2\Omega_p}, \tag{210}$$

and

$$\Delta\tau_o = \frac{|T_e-T_o|\sqrt{1+T_o^2}}{\Omega_p|1+T_oT_e|} \tag{211}$$

is the coherence time. Additionally, we introduce the normalized mean intensity of the ordinary photon as, $\tilde{I}_o(t) = I_d(t)/I_d^{\max}$, where

$$I_d^{\max} = \frac{P_b}{\sqrt{2\pi}\Delta t_\mu}. \tag{212}$$

The correlation function (208) describes a field emitted by a Gaussian Schell-model source [51]. For such a field, the degree of global coherence is introduced as

$$C = \frac{\Delta\tau_o}{\Delta t_o} = 2\left|\frac{T_o - T_e}{1 + T_o T_e}\right|, \tag{213}$$

which tends to zero for a completely incoherent field and to infinity for a fully coherent one [51]. This quantity can be inferred from the experimental data of temporally magnified photodetection described in Section 4.1. A Gaussian fit of the distribution of arrival times on every detector of Figure 26 will give a standard deviation $\Delta t_M = M\Delta t_o$, while a Gaussian fit of the $g^{(2)}(\tau) - 1$ function will give a standard deviation $\Delta t_M = M\Delta t_o/\sqrt{2}$. As a result, the degree of global coherence can be found as $C = \sqrt{2}\Delta\tau_M/\Delta t_M$.

Schmidt decomposition

A double-Gaussian JTA, Eq. (206), can be represented in the form of Schmidt decomposition by means of Mehler's formula for Hermite polynomials [110]

$$\tilde{J}_0(t, t') = \sqrt{P_b}\sum_{n=0}^{\infty}\sqrt{\lambda_n}\psi_n(t)\phi_n(t'), \tag{214}$$

where $\psi_n(t)$ and $\phi_n(t')$ are the Schmidt modal functions of the ordinary and extraordinary photons respectively, defined via the Hermite-Gauss functions $h_n(x)$ as

$$\psi_n(t) = \frac{1}{\sqrt{\tau_1}}h_n(t/\tau_1), \tag{215a}$$

$$\phi_n(t) = \frac{1}{\sqrt{\tau_2}}h_n(t/\tau_2), \tag{215b}$$

λ_n are the Schmidt coefficients

$$\lambda_n = \frac{2}{K+1}\left(\frac{K-1}{K+1}\right)^n \tag{216}$$

normalized to unity, $\sum_n \lambda_n = 1$, and

$$K = \frac{1}{\sum_n \lambda_n^2} = \frac{\sqrt{(1+T_o^2)(1+T_e^2)}}{|T_o - T_e|} \tag{217}$$

is the Schmidt number. The Schmidt number K shows the effective number of entangled modes for each photon and as such is a measure of the degree of entanglement [87, 88, 111]. The temporal widths of the Schmidt modes are

$$\tau_{1,2} = \frac{\sqrt{|T_o - T_e|}}{\sqrt{2}\Omega_p}\left(\frac{1+T_{o,e}^2}{1+T_{e,o}^2}\right)^{\frac{1}{4}}. \tag{218}$$

Substituting the decomposition (214) into Eq. (204) and using the completeness of modal functions, we obtain

$$G_d^{(1)}(t,\tau) = P_b \sum_{n=0}^{\infty} \lambda_n \psi_n^*(t)\psi_n(t+\tau), \tag{219}$$

which is known as Mercer expansion in coherence modes [51]. We see that the Schmidt modes of two entangled waves are the coherence modes of each wave. From Eqs. (213) and (217) we obtain

$$K^2 = 1 + \frac{4}{C^2}, \tag{220}$$

which relates the measure of entanglement K to the measure of coherence C. Equation (220) has a clear physical meaning: The higher is the coherence, the lower is the entanglement, with a single-mode regime ($K = 1$) for a fully coherent ordinary wave ($C = \infty$). In addition, this equation allows one to determine experimentally the number of modes by measuring C, as described in the preceding section.

4.3 Symmetric and asymmetric group velocity matching

We illustrate the general formalism by considering a crystal with $\tau_o = -\tau_e$, which is known as symmetric group velocity matching [74, 78] or extended phase matching [81]. This type of phase matching is attractive because it allows one to pass from the single-mode to a multimode regime by simply varying the pump bandwidth [112]. It was first engineered in a crystal of periodically-poled potassium titanyl phosphate (ppKTP) [113], which we consider here as an example. The pump propagates along the X axis of this biaxial crystal and is polarized along the Y axis, i.e. represents an ordinary wave. The two subharmonic waves are polarized along the Y (ordinary wave) and Z (extraordinary wave) axes of the crystal.

The refractive indices for the Y and Z polarized waves are obtained from the Sellmeier equations for KTP [113] and, for a crystal of length $L = 40$ mm pumped at wavelength $\lambda_p = 2\pi c/\omega_p = 791.5$ nm, we obtain $\tau_o = -\tau_e = 2.95$ ps. The phase mismatch at degeneracy for a periodically poled crystal with the poling period Λ and order m is defined as [58]

$$\Delta_0 = k_p(\omega_p) - k_o(\omega_0) - k_e(\omega_0) + \frac{2\pi m}{\Lambda}. \tag{221}$$

The poling period required for reaching the phase matching at degeneracy for $m = 1$ is $\Lambda = 47.6\ \mu$m. Substituting $\tau_o = -\tau_e > 0$ into Eq. (217), we obtain

$$K = \frac{1}{2}\left(T_o + \frac{1}{T_o}\right) = \frac{1}{2}\left(\frac{\delta_s \tau_o}{\tau_p} + \frac{\tau_p}{\delta_s \tau_o}\right), \tag{222}$$

where $\delta_s = 2\sqrt{\ln 2}/\sigma_s \approx 1.03$. The minimal value of $K = 1$ is reached at the pump pulse

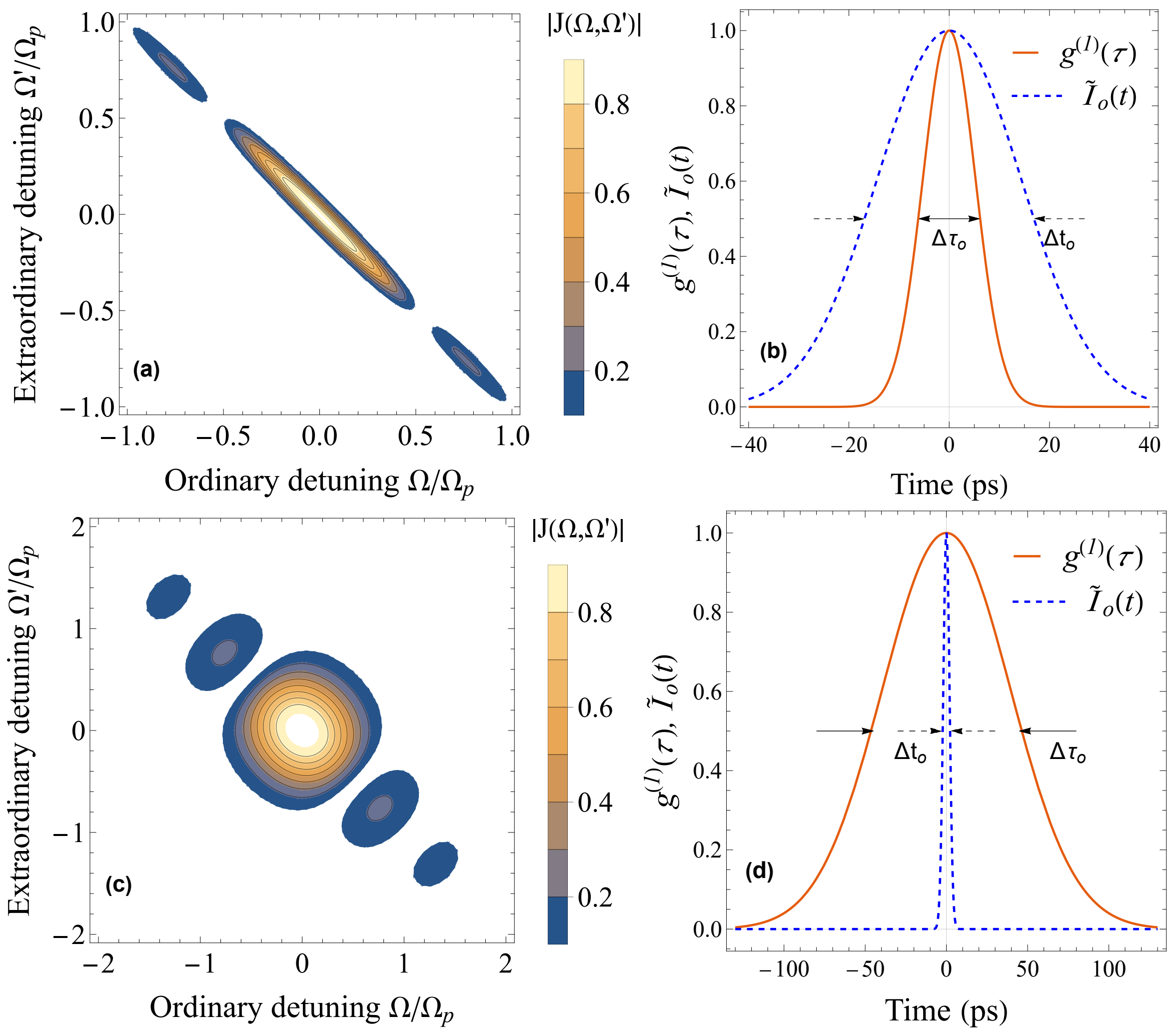

Figure 27: (a) Normalized JSA and (b) first-order autocorrelation function and normalized mean intensity of the ordinary wave generated in PDC in a 40-mm-long ppKTP crystal pumped at a wavelength of $\lambda_p = 791.5$ nm by pulses of duration 30 ps, resulting in a multimode generation with $K \approx 5$. Similar plots in (c) and (d) for pump pulses of duration 3 ps, resulting in a single-mode generation with $K \approx 1$.

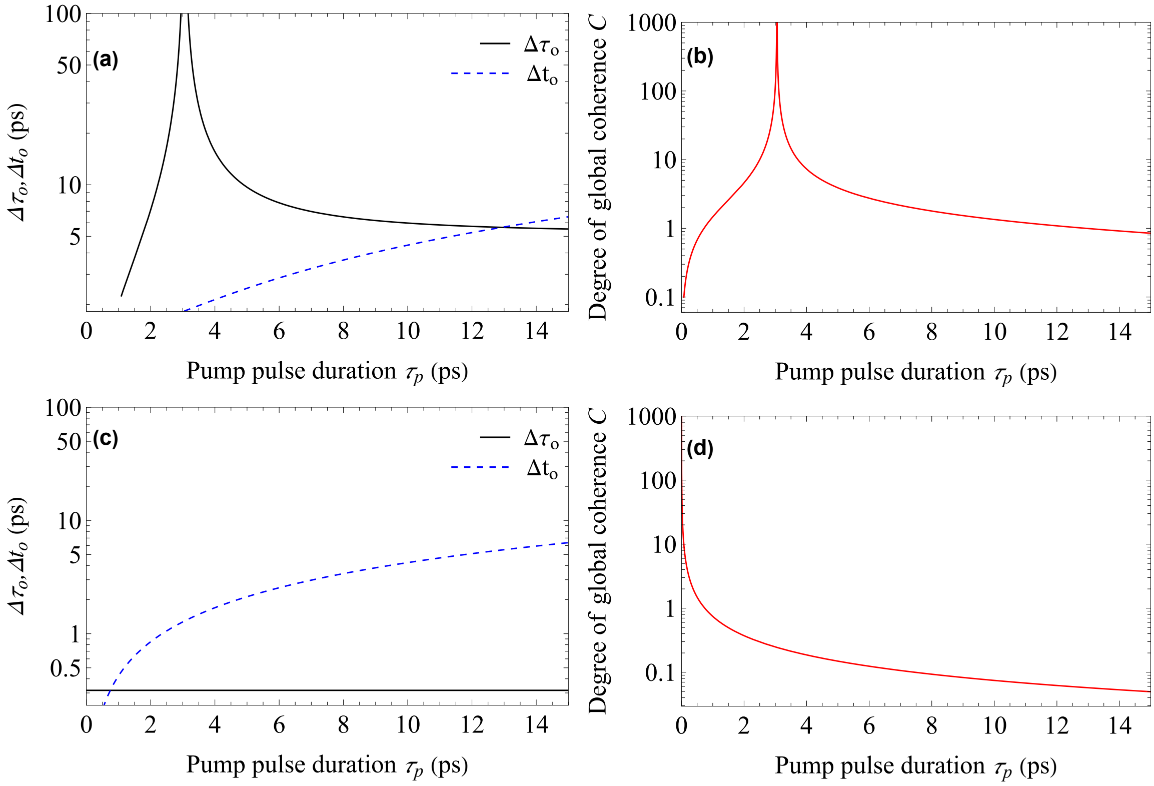

Figure 28: (a) Coherence time $\Delta\tau_o$ and the standard deviation of the mean intensity Δt_o and (b) degree of global coherence C as functions of the pump pulse duration τ_p for the waves generated in PDC in a 40-mm-long ppKTP crystal with symmetric group velocity matching by setting $\tau_o = -\tau_e = 2.95$ ps. Similar plots in (c) and (d) for waves generated by SPDC in a 5-mm-long KDP crystal with asymmetric group velocity matching with $\tau_o = 0$ and $\tau_e = 360$ fs.

duration $\tau_p = \delta_s \tau_o \approx 3$ ps, which corresponds to $\Omega_p = 2\pi \times 62$ GHz or FWHM spectral bandwidth $\Delta\lambda = 0.3$ nm. In this case, the photons are disentangled, each occupying just one Gaussian temporal mode, as required for some applications, for example, heralding the generation of modally pure single photons [102]. For comparison, we consider the case of $\tau_p = 3$ ps and also the case of a ten times longer pump pulse with $\tau_p = 30$ ps, which corresponds to $\Omega_p = 2\pi \times 6.2$ GHz or FWHM spectral bandwidth $\Delta\lambda = 0.03$ nm. Figure 27 shows the JSA of the photons and their normalized correlation function and mean intensity.

In the single-mode case, we have $T_o \approx 1$ and $K \approx 1$. We find $\Delta t_o = 1.8$ ps and $\Delta\tau_o = 284$ ps, whereform $C = 157$, which corresponds to Eq. (220) with $K \approx 1$. In the multimode case, we have $T_o \approx 0.1$ and obtain $K \approx 5$ from Eq. (222). We find also $\Delta t_o = 13$ ps and $\Delta\tau_o = 5.2$ ps from Eqs. (210) and (211), where we obtain $C = 0.4$. These values of K and C are related by Eq. (220). The same values of K and C appear for pulses shorter 10 times than in the single-mode case, i.e. $\tau_p = 0.3$ ps.

Figure 28 illustrates the coherence time $\Delta\tau_o$, the standard deviation of the mean intensity Δt_o and degree of global coherence C as functions of the pump pulse duration τ_p. Plots (a) and (b) represent the symmetric group velocity-matched ppKTP crystal considered in this section and plots (c) and (d) show the asymmetric group velocity-matched KDP crystal considered in Section 3.3 with $\tau_o = 0$ and $\tau_e = 360$ fs. We see that a single-mode regime with coherence tending to infinity is realized in both cases for certain values of the pump pulse duration.

4.4 Summary

In this chapter, we have established a link between the second-order correlation function and the spectral decomposition of the joint spectral amplitude (JSA) of photons generated in type-II SPDC. This connection enables us to precisely evaluate the number of temporal modes in a pulse by measuring its temporal width and coherence time, providing valuable insights for quantum information encoding. We demonstrated this capability with photons generated in symmetric group velocity-matched non-linear crystal ppKTP and asymmetric group velocity-matched KDP crystal. Additionally, we illustrated how a temporal imaging system can stretch ultrashort temporal waveforms on the picosecond scale, which are not optimal for detections by photodetectors, to the nanosecond scale. Thus, we have developed a method for experimental determination of the number of Schmidt modes of a photon pair generated in PDC.

Conclusion

In this thesis, we studied multiple applications of temporal imaging systems. Quantum temporal imaging is poised to play a crucial role in future quantum technologies, being applied across various hardware setups. The ongoing advancements in quantum technologies demand specialized tools capable of manipulating quantum states without compromising encoded information. The temporal manipulation, involving time stretching and compression, aids in the detection of these states by quantum registers and significantly impacts telecommunication protocols. Furthermore, within quantum networks, there's a combination of slower components like quantum memories and faster elements such as communication lines and noiseless manipulation of the quantum states can play a crucial role in realizing an optimal quantum network.

The Hong-Ou-Mandel interference, as the first demonstration of two-photon interference, proves to be a successful method for investigating the indistinguishability of photon pairs. As our first application, we focused on applying a time lens to the light generated in a frequency-degenerate type-II SPDC (Spontaneous Parametric Down-Conversion) process driven by a pulsed broadband source. This particular SPDC scenario results in signal and idler photons with distinct spectral and temporal properties, leading to reduced indistinguishability and compromised visibility in Hong-Ou-Mandel interference. Through our analysis, we demonstrated that inserting a time lens into one arm of the interferometer, along with careful selection of its magnification factor, enables achieving 100% visibility in Hong-Ou-Mandel interference under the condition of sufficiently large focal GDD of the used time lens. This successful intervention restores perfect indistinguishability between the signal and idler photons.

In our theoretical model, we considered the synchronization of the pulsed SPDC source and the time lens to optimize the destructive interference of the signal and idler waves. We investigated the impact of desynchronization on second-order interference visibility, finding that for large values of the focal GDD (Group Delay Dispersion) of the lens, desynchronization has a negligible effect, allowing for perfect interference visibility. Our analytical calculations assumed a Gaussian shape for the pump pulses and a Gaussian approximation for the phase-mismatch function, yielding important analytical results, including spectra and temporal shapes of the waves. We also derived an analytical formula for the optimal magnification factor of the time lens, providing unit visibility in Hong-Ou-Mandel interference, with a straightforward physical interpretation related to the temporal durations of the pulses. We further assessed the feasibility of our proposal for experimental realization, offering quantitative estimations for two potential time lens implementations—based on EOPM (Electro-Optic Phase Modulator) and FWM (Four-Wave Mixing). Our results suggest that the theoretical proposal is experimentally feasible, with some differences in the input bandwidth capabilities between the two types of time lenses.

Moving towards the next application of quantum temporal imaging, we have formulated a general theory for a time telescope employing two time lenses. Our findings reveal that optimal efficiency is achieved with just two dispersive media. Additionally, we have demonstrated the creation of an erecting time telescope using two time lenses with opposite signs of their focal GDDs. In contrast to spatial Galilean telescopes, this device generates a real erect image and proves valuable in photonic quantum networks for pure temporal scaling of optical fields, free from residual temporal chirp. We have specifically applied this time telescope to distinguishable photons generated by SPDC and single emitters like quantum dots. In both cases, our results illustrate that photons can attain perfect indistinguishability through the use of an erecting time telescope. Recent advancements indicate the feasibility of realizing both time lenses and dispersive elements on an integrated photonic chip with minimal losses, as highlighted in recent research. This development opens promising avenues for employing time telescopy in the realization of quantum photonic-photonic interconnects.

Finally, we studied the possibility of measuring the time-resolved second-order autocorrelation function of one of two beams generated in type-II parametric downconversion by means of temporal magnification of this beam, bringing its correlation time from the picosecond to the nanosecond scale, resolvable by modern photodetectors. We also showed that such a measurement enables one to infer directly the degree of global coherence of that beam, which is linked by a simple relation to the number of Schmidt modes characterizing the entanglement between the two generated beams. We illustrated the proposed method by the photon pairs generated in a periodically poled KTP crystal with a symmetric group velocity matching and a KDP crystal with an asymmetric group velocity matching for various durations of the pump pulse, resulting in different numbers of modes.

Prospectives

The applications of quantum temporal imaging systems in photonic technologies do not stop here and can be extended to study the theory of super-resolution in optics. Abbe and Rayleigh, in their seminal late-nineteenth-century works [114], defined the classical resolution limit for optical instruments based on diffraction at the system's pupil. Diffraction causes a finite-sized diffraction pattern for a point source at the output, and as two sources approach, their patterns overlap, making discrimination challenging. The minimum separation for discrimination involves various factors, with the Rayleigh criterion being the most recognized, indicating patterns are just resolved when one's central maximum aligns with the other's first minimum. In classical optics, resolution is characterized by spatial transmission bandwidth, determined by the system's pupil size, allowing a finite band of spatial frequencies. Super-resolution aims to surpass this limit, restoring frequencies beyond the band. However, achieving super-resolution necessitates *a priori information* about the input object, and significant improvement beyond the Rayleigh limit often results in a reduced signal-to-noise ratio. Quantum theory investigations in Ref. [9] give an insight that the idea can be extended to temporal imaging, indicating that the extension can be achieved by introducing a time lens in place of the traditional lens.

Broadband temporal modes of pulsed optical fields have recently gained recognition for their substantial potential in photonic quantum information processing and time-frequency metrology. However, fully harnessing their capabilities requires efficient and flexible tools for manipulation. Surprisingly, the most fundamental tool, a single-mode temporal filter, has yet to be demonstrated. In a prospective study, one could propose an experimentally viable approach to realize an authentic single-mode temporal filter. This approach is founded on the concept of a temporal cavity, a device with resonances dependent on temporal modes within the framework of frequency comb modes. Analogous to spatial-mode cleaner cavities in the spatial domain, this device has the potential to enable robust temporal mode filtering and detection. Such advancements could open new prospects in time-frequency metrology and multidimensional quantum information processing.

In Ref. [115], the authors introduced the concept of a temporal lens designed to focus and magnify ultrashort electron packets in the time domain. These temporal lenses are formed by synthesizing optical pulses that interact with electrons through the ponderomotive force. The resulting temporal lens equation closely resembles the form observed in conventional light optics. Similar to ray diagrams employed in the optical domain, electron counterparts are constructed to aid in visualizing the compression process of electron packets. The study demonstrates that these temporal lenses not only compensate for electron pulse broadening due to velocity dispersion but also facilitate compression to durations significantly shorter than their initial widths. With these capabilities, the proposed scheme presents opportunities for investigating quantum temporal imaging in fermionic systems. The exploration can be extended to various aspects, including the observation of distinguishability of states, applications in quantum networks, and counting fermionic modes.

Appendices

Appendix A

Fraunhofer limit for dispersion of a chirped pulse

In most publications on a time lens, a Fourier-limited pulse is considered at the input to the temporal imaging system. However, a single-photon pulse produced by a PDC source in a sufficiently long crystal may be not Fourier-limited, having a nonnegligible frequency chirp. Here we analyze the dispersive broadening of a chirped pulse and find the conditions for the Fraunhofer limit of dispersion.

We consider a classical field with the positive-frequency part $E^{(+)}(t) = Y_0(t)e^{-i\omega_0 t}$, where ω_0 is the carrier frequency and $Y_0(t)$ is the envelope amplitude, which we assume to have a Gaussian distribution with the (intensity) standard deviation Δt_0:

$$Y_0(t) = E_0 e^{-t^2/4\Delta t_0^2}, \tag{223}$$

where E_0 is the peak amplitude. In the frequency domain, we have

$$\tilde{Y}_0(\Omega) = \int Y_0(t)e^{i\Omega t}dt = 2\sqrt{\pi}\Delta t_0 E_0 e^{-\Delta t_0^2\Omega^2}, \tag{224}$$

so the standard deviation of the intensity spectrum $S_0(\Omega) = |\tilde{Y}_0(\Omega)|^2$ is $\sigma_0 = 1/2\Delta t_0$. For the FWHM temporal and spectral widths T_0^{F} and Ω_0^{F}, respectively, we find the time-bandwidth product $T_0^{\mathrm{F}}\Omega_0^{\mathrm{F}} = 4\ln 2 \approx 2\pi \times 0.44$, as expected for a Fourier-limited Gaussian pulse.

This pulse passes through a dispersive medium of length L_1 with the dispersion law $k_1(\Omega) = k_1^0 + k_1'\Omega + k_1''\Omega^2/2$, which we limit to terms up to the quadratic one in the frequency detuning $\Omega = \omega - \omega_0$. The field at the output is simply $\tilde{Y}_1(\Omega) = \tilde{Y}_0(\Omega)e^{ik_1(\Omega)L_1}$, which gives in the time domain

$$Y_1(t) = \int \tilde{Y}_1(\Omega)e^{-i\Omega t}\frac{d\Omega}{2\pi} = E_1 e^{-\tau^2/4\Delta t_1^2 - i\tau^2/2C_1}, \tag{225}$$

where $E_1 = E_0 e^{ik_1^0 L_1}/\sqrt{1 - iD_1/2\Delta t_0^2}$ is the new peak amplitude, $D_1 = k_1'' L_1$ is the GDD acquired in the medium, $\tau = t - k_1' L_1$ is the time delayed by the group delay in the medium,

$$C_1 = D_1 + 4\Delta t_0^4/D_1 \tag{226}$$

is the chirp coefficient of the output pulse, and

$$\Delta t_1 = \sqrt{\Delta t_0^2 + D_1^2/4\Delta t_0^2} \tag{227}$$

is the (intensity) standard deviation of the temporal distribution of the outgoing pulse. The spectral distribution is unchanged $|\tilde{Y}_1(\Omega)|^2 = |\tilde{Y}_0(\Omega)|^2$ and the spectral standard deviation is $\sigma_1 = \sigma_0$.

Had we considered the Fraunhofer limit for this dispersion, we would have obtained the condition $D_1^2 \gg 4\Delta t_0^4$ and the relation $\Delta t_1 = |D_1|/2\Delta t_0$ [12, 13, 17, 37]. However, in our case, we are looking for the Fraunhofer limit for the second dispersive medium of length L_2 with the dispersion law $k_2(\Omega) = k_2^0 + k_2'\Omega + k_2''\Omega^2/2$ on the path of the same pulse. Similarly to the first medium, we have for the pulse at the output of the second medium: $\tilde{Y}_2(\Omega) = \tilde{Y}_1(\Omega)e^{ik_2(\Omega)L_2} = \tilde{Y}_0(\Omega)e^{i[k_1(\Omega)L_1 + k_2(\Omega)L_2]}$, which gives in the time domain

$$Y_2(t) = E_2 e^{-\tau^2/4\Delta t_2^2 - i\tau^2/2C_2}, \tag{228}$$

where $E_2 = E_0 e^{i(k_1^0 L_1 + k_2^0 L_2)}/\sqrt{1 - i(D_1 + D_2)/2\Delta t_0^2}$ is the new peak amplitude, $D_2 = k_2'' L_2$ is the GDD aquired in the second medium, $\tau = t - k_1' L_1 - k_2' L_2$ is the time delayed by the total group velocity delay in both media, $C_2 = D_1 + D_2 + 4\Delta t_0^4/(D_1 + D_2)$ is the chirp coefficient of the output pulse, and

$$\Delta t_2 = \sqrt{\Delta t_0^2 + (D_1 + D_2)^2/4\Delta t_0^2} \tag{229}$$

is the (intensity) standard deviation of the temporal distribution of the outgoing pulse after the second medium.

The Fraunhofer limit for the dispersion in the second medium occurs when the second term under the square root in Eq. (229) is much greater than the first one, meaning $(D_1 + D_2)^2 \gg 4\Delta t_0^4$, in which case we can rewrite Eq. (229) as $\Delta t_2 = |D_1 + D_2|/2\Delta t_0$. We can rewrite these two relations through the characteristics of the pulse entering the second medium only, if we express $(\Delta t_0, D_1)$ via $(\Delta t_1, C_1)$ by inverting the system of equations (226) and (227). For this end, we multiply Eq. (226) by D_1 and the square of Eq. (227) by $4\Delta t_0^2$ and obtain the same expression on the right-hand sides, i.e., $C_1 D_1 = 4\Delta t_0^2 \Delta t_1^2$. This expression allows us to exclude D_1 from Eq. (227) and Δt_0 from Eq. (226), obtaining $\Delta t_0 = 1/2\sigma_0 = 1/2\sigma_1 = \Delta t_1(1 + 4\Delta t_1^4/C_1^2)^{-1/2}$ and $D_1 = C_1(1 + C_1^2/4\Delta t_1^4)^{-1}$. The two relations of the Fraunhofer dispersion limit are thus

$$\begin{aligned} (D_1 + D_2)^2 &\gg 1/4\sigma_1^4 = 4\Delta t_1^4(1 + 4\Delta t_1^4/C_1^2)^{-2}, && (230) \\ \Delta t_2 &= |D_1 + D_2|\sigma_1 && (231) \\ &= |D_1 + D_2|(1 + 4\Delta t_1^4/C_1^2)^{1/2}/2\Delta t_1. \end{aligned}$$

We see that for a considerable D_1, the condition $D_2^2 \gg 4\Delta t_1^4$ may be not satisfied and $\Delta t_2 \neq D_2/2\Delta t_1$ in the Fraunhofer limit. Instead, Eqs. (230) and (231) should be used. In our setup, D_1 is the GDD acquired by the ordinary photon in the nonlinear crystal and D_2 is the GDD of the dispersive element before the time lens, and we define $D_{\text{in}} = D_1 + D_2$.

Appendix B

Gaussian pulse passage through a time telescope

We consider a classical field with the positive-frequency part $E^{(+)}(t) = Y_0(t)e^{-i\omega_0 t}$, where ω_0 is the carrier frequency and $Y_0(t)$ is the envelope amplitude, which we assume to have a Gaussian distribution with the (intensity) standard deviation Δt_0,

$$Y_0(t) = E_0 e^{-t^2/4\Delta t_0^2}, \tag{232}$$

where E_0 is the peak amplitude. In the frequency domain, we have

$$\tilde{Y}_0(\Omega) = \int Y_0(t)e^{i\Omega t}dt = 2\sqrt{\pi}\Delta t_0 E_0 e^{-\Delta t_0^2\Omega^2}, \tag{233}$$

so the standard deviation of the intensity spectrum $S_0(\Omega) = |\tilde{Y}_0(\Omega)|^2$ is $\Delta\Omega_0 = 1/2\Delta t_0$. For the FWHM temporal and spectral widths $T_0 = 2\sqrt{2\ln 2}\Delta t_0$ and $\Omega_0 = 2\sqrt{2\ln 2}\Delta\Omega_0$ respectively, we find the time-bandwidth product $T_0\Omega_0 = 4\ln 2 \approx 2\pi \times 0.44$, as expected for a Fourier-limited Gaussian pulse.

We consider the passage of this pulse through the time telescope shown in Figure 18. Every time lens changes the pulse bandwidth, leaving its duration intact. In contrast, every dispersive medium changes the pulse duration, leaving its bandwidth intact. After the first time lens the field becomes $Y_1(t) = Y_0(t)\exp(it^2/2D_\mathrm{f})$. By taking the Fourier transform, we find the standard deviation of its spectrum,

$$\Delta\Omega_1 = \Delta\Omega_0\sqrt{1 + D_\mathrm{f}^{-2}/4\Delta\Omega_0^4}. \tag{234}$$

After passing through the dispersive medium with GDD $D_\mathrm{inter} = D_\mathrm{f}(1 - M)$, the field becomes [46]

$$Y_2(t) \propto \int Y_1(t')e^{-i(t-t')^2/2D_\mathrm{inter}}dt, \tag{235}$$

which gives a chirped Gaussian pulse with the (intensity) standard deviation

$$\Delta t_2 = M\Delta t_0 \sqrt{1 + D_{\mathrm{f}}^2 (1-M)^2 / 4\Delta t_0^4 M^2}. \tag{236}$$

After the second time lens with the focal GDD $D'_{\mathrm{f}} = -MD_{\mathrm{f}}$, the field is $Y_3(t) = Y_2(t)\exp(it^2/2D'_{\mathrm{f}})$ and the standard deviation of its spectrum is $\Delta\Omega_3 = \Delta\Omega_0/M$. Passage through the last dispersive medium compresses the pulse to duration $\Delta t_4 = M\Delta t_0$.

Appendix C

Single emitter interferometry

Substituting for the fields at the detectors $D_\pm$ in Eq. (188) and applying the commutation relations, we obtain

$$\begin{aligned}R_c(\delta\tau) = \frac{1}{4T}\int \mathrm{d}t \int \mathrm{d}t' \mathrm{Tr}\Big[\Big(&-A_1^\dagger(t/M)A_2^\dagger(t'+\delta\tau)A_1(t'/M)A_2(t+\delta\tau)\\ &+ A_1^\dagger(t/M)A_2^\dagger(t'+\delta\tau)A_2(t'+\delta\tau)A_1(t/M) + A_2^\dagger(t+\delta\tau)A_1^\dagger(t'/M)A_1(t'/M)A_2(t+\delta\tau)\\ &- A_2^\dagger(t+\delta\tau)A_1^\dagger(t'/M)A_2(t'+\delta\tau)A_1(t/M)\Big)\rho_1\rho_2\Big].\end{aligned} \tag{237}$$

The above expression can be evaluated analytically by integrating each of the terms inside the trace,

$$\begin{aligned}R_c(\delta\tau) &= \frac{1}{4TM}\int\int_0^T \mathrm{d}t\mathrm{d}t'\Big[-f_1(t/M,t'/M)f_2(t'+\delta\tau,t+\delta\tau) + f_1(t/,t/M)f_2(t'+\delta\tau,t'+\delta\tau)\\ &\quad + f_1(t'/M,t'/M)f_2(t+\delta\tau,t+\delta\tau) - f_1(t'/M,t/M)f_2(t+\delta\tau,t'+\delta\tau)\Big]\\ &= \frac{1}{4TM}\Big[2|M|\mu_1\mu_2 - 2\int\int_0^T \mathrm{d}t\mathrm{d}t' f_1(t/M,t'/M)f_2(t'+\delta\tau,t+\delta\tau)\Big]\\ &= \frac{P_b}{2}\Big[1-p_{\mathrm{int}}(\delta\tau)\Big],\end{aligned} \tag{238}$$

where we have introduced the temporal function $f(t_1,t_2) = \psi(t_1)\psi^*(t_2)$. Now we write the temporal overlap of the stretched first and delayed second photons using Eqs. (238) and (189)

$$c(\delta\tau) = \frac{1}{\sqrt{\tau_1\tau_2}}\int_0^\infty \mathrm{d}t e^{-t/2|M|\tau_1-(t+\delta\tau)/2\tau_2}\theta(t/|M|)\theta(t+\delta\tau). \tag{239}$$

For $|M| > 0$: In the case of $\delta\tau > 0$ we can just put the Heaviside step function $\theta(t/M)\theta(t+\delta\tau) = 1$ and evaluate the integral using $\int_0^\infty \mathrm{d}te^{-at} = 1/a$. And, for the case of $\delta\tau < 0$, we evaluate as

$$\begin{aligned} c(\delta\tau) = \frac{1}{\sqrt{\tau_1\tau_2}}\Bigg[\int_0^{-\delta\tau} &\mathrm{d}te^{-t/2|M|\tau_1-(t+\delta\tau)/2\tau_2}\theta(t/|M|)\theta(t+\delta\tau) \\ + \int_{-\delta\tau}^{\infty} \mathrm{d}te^{-t/2|M|\tau_1-(t+\delta\tau)/2\tau_2}\theta(t/|M|)\theta(t+\delta\tau)\Bigg] \\ = \frac{1}{\sqrt{\tau_1\tau_2}}\left[0+\frac{2|M|\tau_1\tau_2}{|M|\tau_1+\tau_2}e^{\delta\tau/2|M|\tau_1}\right] = \frac{2|M|\sqrt{\tau_1\tau_2}}{|M|\tau_1+\tau_2}e^{\delta\tau/2|M|\tau_1} \end{aligned} \tag{240}$$

and we finalize these calculations as

$$c(\delta\tau) = \begin{cases} \frac{2|M|\sqrt{\tau_1\tau_2}}{|M|\tau_1+\tau_2}e^{-\delta\tau/2\tau_2}, & \text{if } \delta\tau > 0 \\ \\ \frac{2|M|\sqrt{\tau_1\tau_2}}{|M|\tau_1+\tau_2}e^{\delta\tau/2|M|\tau_1}. & \text{if } \delta\tau < 0 \end{cases} \tag{241}$$

Through this, we obtain Eq. (190).

For $|M| < 0$: In the case of $\delta\tau > 0$, we integrate our expression in the limits of the region where the functions $\theta(-t/|M|)$ and $\theta(t+\delta\tau)$ overlap and we obtain

$$\begin{aligned} c'(\delta\tau) &= \frac{1}{\sqrt{\tau_1\tau_2}}\int_{-\delta\tau}^{0} \mathrm{d}te^{t/2|M|\tau_1-(t+\delta\tau)/2\tau_2} \\ &= \frac{2|M|\sqrt{\tau_1\tau_2}}{|M|\tau_1-\tau_2}\left(e^{-\delta\tau/2|M|\tau_1}-e^{-\delta\tau/2\tau_2}\right). \end{aligned} \tag{242}$$

And, in the case of $\delta\tau < 0$, we discover that $\theta(-t/|M|)\theta(t+\delta\tau) = 0$. Therefore, we obtain $c(\delta\tau) = 0$ resulting in Eq. (192). We introduce a constant $\gamma = \tau_2/\tau_1$ to simplify our further calculations and write Eq. (192)

$$p_{\text{int}}(\delta\tau) = \frac{4\gamma}{(1-\gamma)^2}\left(e^{-\delta\tau/2\tau_1}-e^{-\delta\tau/2\gamma\tau_1}\right)^2. \tag{243}$$

To find the maximum value of this probability, we take its derivative with respect to $\delta\tau$, put it to zero and solve for $\delta\tau$:

$$\frac{8\gamma}{(1-\gamma)^2}\left(e^{-\delta\tau/2M\tau_1}-e^{-\delta\tau/2\tau_1\gamma}\right)\left(\frac{e^{-\delta\tau/2\tau_1\gamma}}{2\tau_1\gamma}-\frac{e^{-\delta\tau/2\tau_1}}{2\tau_1}\right) = 0. \tag{244}$$

We observe that the factor $\left(e^{-\delta\tau/2M\tau_1}-e^{-\delta\tau/2\tau_1\gamma}\right)$ cannot be zero and the exponentials have opposite signs, so the only solution is when the second factor is zero:

$$\gamma e^{-\delta\tau/2\tau_1} = e^{-\delta\tau/2\gamma\tau_1} \tag{245}$$

Taking the natural logarithm on both sides and solving for $\delta\tau$, we obtain Eq. (193).

Appendix D

Gaussian model

Substituting Eq. (205) into (203), we arrive at

$$\tilde{J}_0(t,t') = \int\int \kappa L \alpha_0 \exp\left[-\frac{(\Omega+\Omega')^2}{4\Omega_p^2} - \frac{(\tau_o\Omega+\tau_e\Omega')^2}{2\sigma_s^2}\right] e^{-i\Omega t - i\Omega' t'} \frac{\mathrm{d}\Omega\mathrm{d}\Omega'}{(2\pi)^2}. \tag{246}$$

Expanding the squares, and using $T_\mu = \sqrt{2}\Omega_p\tau_\mu/\sigma_s$, we write

$$\tilde{J}_0(t,t') = \int\int \kappa L \alpha_0 \exp\left[\frac{1}{4\Omega_p^2}\left(-\Omega^2\left[1+T_o^2\right] - \Omega'^2\left[1+T_e^2\right] - 2\Omega\Omega'\left[1+T_oT_e\right]\right) - i\Omega t - i\Omega' t'\right] \frac{\mathrm{d}\Omega\mathrm{d}\Omega'}{(2\pi)^2}. \tag{247}$$

Using the multidimensional Gaussian integral technique from Eq. (138), the above expression takes the form

$$\tilde{J}_0(t,t') = \frac{\kappa L \alpha_0}{(2\pi)^2}\left[\frac{(2\pi)^2}{\det\Lambda}\right]^{\frac{1}{2}} e^{-\frac{1}{2}\mathbf{v}^T\Lambda^{-1}\mathbf{v}}, \tag{248}$$

where

$$\Lambda = \frac{1}{2\Omega_p^2}\begin{pmatrix} 1+T_o^2 & 1+T_oT_e \\ 1+T_oT_e & 1+T_e^2 \end{pmatrix}, \tag{249}$$

and $\mathbf{v} = (-t,-t')^T$. From this, we can calculate

$$\frac{\Lambda^{-1}}{2} = \mathbf{M} = \frac{\Omega_p^2}{(T_o-T_e)^2}\begin{pmatrix} 1+T_e^2 & -1-T_oT_e \\ -1-T_oT_e & 1+T_o^2 \end{pmatrix}. \tag{250}$$

Now, substituting Eq. (206) into Eq. (204), we arrive at

$$G_d^{(1)}(t,\tau) = \int J_1^2 e^{-M_{11}t^2-2M_{22}t'^2-2M_{12}tt'-M_{11}(t+\tau)^2-2M_{12}(t+\tau)t'}\mathrm{d}t'. \tag{251}$$

The above expression is a Gaussian integral, which can be integrated using the identity

$$\int_{-\infty}^{\infty} e^{-ax^2+bx+c}\,dx = \sqrt{\frac{\pi}{a}}\,e^{\frac{b^2}{4a}+c}, \tag{252}$$

yielding us

$$G_d^{(1)}(t,\tau) = J_1^2\sqrt{\frac{\pi}{2M_{22}}}e^{-M_{11}t^2-M_{11}(t+\tau)^2+M_{12}^2(2t+\tau)^2/2M_{22}}. \tag{253}$$

Now, if we express the mean intensity from Eq. (111) via the joint temporal amplitude, we obtain

$$I_d(t) = \int \tilde{J}_0^*(t,t')\tilde{J}_0(t,t')\mathrm{d}t', \tag{254}$$

and substituting Eq. (206) into the above expression yields us

$$I_d(t) = \int J_1^2 e^{2(-M_{11}t^2-M_{22}t'^2-2M_{12}tt')}\mathrm{d}t'. \tag{255}$$

Similarly, the time-delayed mean intensity reads

$$I_d(t+\tau) = \int J_1^2 e^{2(-M_{11}(t+\tau)^2-M_{22}t'^2-2M_{12}(t+\tau)t')}\mathrm{d}t', \tag{256}$$

and comparing Eqs. (251), (255) and (256), we arrive at Eq. (208).

Appendix E

Mathematica implementations

Visibility of entangled photon pairs

We use the following code to define the matrix Λ (see Eq. (140)) in Mathematica:

Listing E.1: Define Λ

```
\[CapitalLambda]=1/(2\[CapitalOmega]p^2) {{1+To^2−I D/M,1+To Te,0,I D},{1+To Te,1+Te^2+I D M,−I D
    ,0},{0,− I D,1+To^2+I D/M,1+To Te},{I D,0,1+To Te,1+Te^2−I D M}};
```

The functions **Inverse**[ ] and **Det**[ ] can be used to give us the inverse and the determinant of the matrix Λ respectively. Now, we define the determinant of Λ as a function of dimensionless focal GDD D in the following way:

Listing E.2: Determinant Λ

```
detL[D_]:=(Te−To) ^4/(16*\[ CapitalOmega]p^8)*(1+M^2*fm*fp*D^2);
```

Next, we write the elements of the matrix Γ from Eq. (144) as a function of D:

Listing E.3: Γ matrix elements

```
\[CapitalGamma]11[D_]:=\[Nu][D]*(1+Te^2+M^2*D^2*fp);
\[CapitalGamma]22[D_]:=\[Nu][D]*(1+To^2+D^2*fp);
\[CapitalGamma]12[D_]:=\[Nu][D]*(−1−Te*To−M*D^2*fp);
```

Using these elements, we define the expressions for visibility for the perfect and the imperfect synchronizations respectively as functions of τ, t and D:

Listing E.4: Interferometric visibilities

```
pint [\[ Tau]_,D_]:=(2*D)/(Abs[Te−To]*Sqrt[1+M^2*fm*fp*D^2])*Exp[−\[CapitalGamma]22[D]*\[Tau
    ]^2/(2*\[Sigma]cw^2)];
pintimp [\[ Tau]_,t_,D_]:=(2*D)/(Abs[Te−To]*Sqrt[1+M^2*fm*fp*D^2])*Exp[−(\[CapitalGamma]11[D
    ]*t^2+2*\[CapitalGamma]12[D]*t*(t−\[Tau])+\[CapitalGamma]22[D]*(t−\[Tau])^2)/(2*\[Sigma]cw
    ^2)];
```

Conditional plot for the coincidence count rate

We define Eq. (190) using the code:

Listing E.5: Single photon interferometric visibility

```
ppint2[M_]:=(4 M Subscript[\[Tau], 1] Subscript[\[Tau], 2] )/(M Subscript[\[Tau], 1]+Subscript[\[
    Tau], 2])^2 E^(-\[Delta]\[Tau]/(Subscript[\[Tau], 2]));
mpint2[M_]:=(4 M Subscript[\[Tau], 1] Subscript[\[Tau], 2] )/(M Subscript[\[Tau], 1]+Subscript[\[
    Tau], 2])^2 E^(\[Delta]\[Tau]/(M Subscript[\[Tau], 1]));
Subscript[\[Tau], 1]=1;Subscript[\[Tau], 2]=3;
```

The plot for the normalized coincidence count rate in Figure 24 is conditional, and the conditions can be called using the function **If**[,]. The code below demonstrates how these conditions are implemented, generating the depicted figure, and one can easily customize parameters like plot style, theme, and range as the code provides flexibility for adjustments.

Listing E.6: Conditional plot

```
    Show[Plot[{If[\[Delta]\[Tau]>0,1-ppint2[3]], If [\[Delta]\[Tau]<0,1-mpint2 [3]]},{\[ Delta]\[Tau
        ],-10,10}, PlotTheme->"Scientific", PlotStyle->Directive[Opacity[1],Blue],PlotRange
        ->{{-10,10},{0,1.5}}, PlotLegends->Placed[{"M = 3" },{0.8,0.9}], Epilog->Inset[Style["(b)",14,
        Bold, GrayLevel [0]],{-9,0.1}], FrameLabel->{{HoldForm["Normalized coincidence rate"],
        None},{HoldForm["Relative delay \[Delta]\[Tau]/Subscript [\[Tau], 1]"], None}},LabelStyle
        ->{14, FontFamily->"Times New Roman",FontStyle->Italic,GrayLevel[0]},ImageSize->
        Medium],Plot[{If[\[Delta]\[Tau]>0,1-ppint2[1]],If [\[Delta]\[Tau]<0,1-mpint2 [1]]},{\[ Delta
        ]\[Tau],-10,10}, PlotStyle->Directive[Opacity[1],Darker[Green],DotDashed],PlotRange
        ->{{-10,10},{0,1.2}}, PlotLegends->Placed[{"Without telescope" },{0.3,0.9}], FrameLabel->{{
        HoldForm["Normalized coincidence rate"],None},{HoldForm["Relative delay \[Delta]\[Tau]/
        Subscript [\[Tau], 1]"], None}},LabelStyle ->{16, FontFamily->"Times New Roman",FontStyle
        ->Italic,GrayLevel[0]},ImageSize->Medium],Plot[{If[\[Delta]\[Tau]>0,1-(E^(-(\[Delta]\[Tau]/
        Subscript[\[Tau], 1])) \[Delta]\[Tau]^2)/Subscript[\[Tau], 1]^2], If [\[Delta]\[Tau
        ]<0,1]},{\[ Delta]\[Tau],-10,10}, PlotTheme->"Scientific", PlotStyle->Directive[Opacity[1],
        Black,Dashed],PlotRange ->{{-5,10},{0,1.5}}, PlotLegends->Placed[{"M = -3" },{0.78,0.8}],
        FrameLabel->{{HoldForm["Normalized coincidence rate"],None},{HoldForm["Relative delay 
        \[Delta]\[Tau]/|M|Subscript [\[Tau], 1]"], None}},LabelStyle ->{16, FontFamily->"Times New 
        Roman",FontStyle->Italic,GrayLevel[0]},ImageSize->Medium]]
```

Bibliography

[1] M. A. Nielsen and I. L. Chuang. *Quantum Computation and Quantum Information: 10th Anniversary Edition*. Cambridge University Press, 2012.

[2] A. M. Turing. “I.—Computing Machinery and Intelligence”. *Mind* LIX (1950), pp. 433–460. DOI: 10.1093/mind/lix.236.433.

[3] N. Gisin, G. Ribordy, W. Tittel, and H. Zbinden. “Quantum cryptography”. *Reviews of Modern Physics* 74 (2002), pp. 145–195. DOI: 10.1103/revmodphys.74.145.

[4] D. P. DiVincenzo. “Quantum Computation”. *Science* 270 (1995), pp. 255–261.

[5] F. Arute et al. “Quantum supremacy using a programmable superconducting processor”. *Nature* 574 (2019), pp. 505–510. DOI: 10.1038/s41586-019-1666-5.

[6] N. Gisin and R. Thew. “Quantum communication”. *Nature Photonics* 1 (2007), pp. 165–171. DOI: 10.1038/nphoton.2007.22.

[7] S. J. Freedman and J. F. Clauser. “Experimental Test of Local Hidden-Variable Theories”. *Physical Review Letters* 28 (1972), pp. 938–941. DOI: 10.1103/physrevlett.28.938.

[8] A. Aspect, P. Grangier, and G. Roger. “Experimental Tests of Realistic Local Theories via Bell’s Theorem”. *Physical Review Letters* 47 (1981), pp. 460–463. DOI: 10.1103/physrevlett.47.460.

[9] M. I. Kolobov, ed. *Quantum Imaging*. New York: Springer, 2007.

[10] H. J. Kimble. “The quantum internet”. *Nature* 453 (2008), pp. 1023–1030. DOI: 10.1038/nature07127.

[11] D. Awschalom et al. “Development of Quantum Interconnects (QuICs) for Next-Generation Information Technologies”. *PRX Quantum* 2 (2021), p. 017002. DOI: 10.1103/PRXQuantum.2.017002.

[12] V. Torres-Company, J. Lancis, and P. Andres. “Space-Time Analogies in Optics”. *Prog. Optics*. Ed. by E. Wolf. Vol. 56. Elsevier, 2011, pp. 1–80. DOI: https://doi.org/10.1016/B978-0-444-53886-4.00001-0.

[13] R. Salem, M. A. Foster, and A. L. Gaeta. “Application of space–time duality to ultrahigh-speed optical signal processing”. *Advances in Optics and Photonics* 5 (2013), p. 274. DOI: 10.1364/aop.5.000274.

[14] S. A. Akhmanov, A. P. Sukhorukov, and A. S. Chirkin. “Nonstationary phenomena and space-time analogy in nonlinear optics”. *J. Exp. Theor. Phys.* 28 (1969), pp. 748–757.

[15] B. H. Kolner. “Active pulse compression using an integrated electro-optic phase modulator”. *Appl. Phys. Lett.* 52 (1988), p. 1122.

[16] B. H. Kolner and M. Nazarathy. “Temporal imaging with a time lens”. *Opt. Lett.* 14 (1989), pp. 630–632.

[17] B. H. Kolner. “Space-Time duality and the theory of temporal imaging”. *IEEE J. Quantum Elect.* 30 (1994), pp. 1951–1963.

[18] J. Giordmaine, M. Duguay, and J. Hansen. “Compression of optical pulses”. *IEEE J. Quantum Elect.* 4 (1968), p. 252.

[19] D. Grischkowsky. “Optical pulse compression”. *Appl. Phys. Lett.* 25 (1974), pp. 566–568.

[20] G. P. Agrawal, P. L. Baldeck, and R. R. Alfano. “Temporal and spectral effects of cross-phase modulation on copropagating ultrashort pulses in optical fibers”. *Physical Review A* 40 (1989), pp. 5063–5072. DOI: 10.1103/physreva.40.5063.

[21] L. Mouradian et al. “Spectro-temporal imaging of femtosecond events”. *IEEE Journal of Quantum Electronics* 36 (2000), pp. 795–801. DOI: 10.1109/3.848351.

[22] C. V. Bennett, R. P. Scott, and B. H. Kolner. “Temporal magnification and reversal of 100 Gb/s optical data with an up-conversion time microscope”. *Appl. Phys. Lett.* 65 (1994), p. 2513.

[23] C. V. Bennett and B. H. Kolner. “Upconversion time microscope demonstrating 103X magnification of femtosecond waveforms”. *Opt. Lett.* 24 (1999), pp. 783–785. DOI: 10.1364/OL.24.000783.

[24] C. V. Bennett and B. H. Kolner. “Principles of parametric temporal imaging. I. System configurations”. *IEEE J. Quantum Elect.* 36 (2000), pp. 430–437. DOI: 10.1109/3.831018.

[25] C. V. Bennett and B. H. Kolner. “Principles of parametric temporal imaging. II. System performance”. *IEEE J. Quantum Elect.* 36 (2000), pp. 649–655. DOI: 10.1109/3.845718.

[26] V. J. Hernandez et al. “104 MHz rate single-shot recording with subpicosecond resolution using temporal imaging”. *Opt. Express* 21 (2013), p. 196.

[27] M. A. Foster et al. “Silicon-chip-based ultrafast optical oscilloscope”. *Nature* 456 (2008), pp. 81–84.

[28] M. A. Foster et al. “Ultrafast waveform compression using a time-domain telescope”. *Nat. Photonics* 3 (2009), pp. 581–585.

[29] Y. Okawachi et al. “High-resolution spectroscopy using a frequency magnifier”. *Opt. Express* 17 (2009), pp. 5691–5697. DOI: 10.1364/OE.17.005691.

[30] O. Kuzucu et al. “Spectral phase conjugation via temporal imaging”. *Opt. Express* 17 (2009), pp. 20605–20614.

[31] M. Jastrzębski et al. “Spectrum-to-position mapping via programmable spatial dispersion implemented in an optical quantum memory”. *Physical Review A* 109 (2024). DOI: 10.1103/physreva.109.012418.

[32] L. A. Lugiato, A. Gatti, and E. Brambilla. “Quantum imaging”. *J. Opt. B* 4 (2002), S176.

[33] Y. Shih. “Quantum Imaging”. *IEEE J. Sel. Top. Quant.* 13 (2007), pp. 1016–1030. DOI: 10.1109/JSTQE.2007.902724.

[34] D. Kielpinski, J. F. Corney, and H. M. Wiseman. “Quantum Optical Waveform Conversion”. *Phys. Rev. Lett.* 106 (2011), p. 130501.

[35] Y. Zhu, J. Kim, and D. J. Gauthier. “Aberration-corrected quantum temporal imaging system”. *Phys. Rev. A* 87 (2013), p. 043808.

[36] J. Lavoie et al. “Spectral compression of single photons”. *Nat. Photonics* 7 (2013), pp. 363–366.

[37] M. Karpiński, M. Jachura, L. J. Wright, and B. J. Smith. “Bandwidth manipulation of quantum light by an electro-optic time lens”. *Nat. Photonics* 11 (2017), pp. 53–57.

[38] F. Sośnicki and M. Karpiński. “Large-scale spectral bandwidth compression by complex electro-optic temporal phase modulation”. *Opt. Express* 26 (2018), pp. 31307–31316. DOI: 10.1364/OE.26.031307.

[39] F. Sośnicki, M. Mikołajczyk, A. Golestani, and M. Karpiński. “Aperiodic electro-optic time lens for spectral manipulation of single-photon pulses”. *Appl. Phys. Lett.* 116 (2020). 234003. DOI: 10.1063/5.0011077.

[40] M. Mazelanik et al. “Temporal imaging for ultra-narrowband few-photon states of light”. *Optica* 7 (2020), pp. 203–208. DOI: 10.1364/OPTICA.382891.

[41] M. Mazelanik, A. Leszczyński, and M. Parniak. “Optical-domain spectral super-resolution via a quantum-memory-based time-frequency processor”. *Nature Comm.* 13 (2022), pp. 1–12.

[42] J. M. Donohue, M. Mastrovich, and K. J. Resch. “Spectrally Engineering Photonic Entanglement with a Time Lens”. *Phys. Rev. Lett.* 117 (2016), p. 243602. DOI: 10.1103/PhysRevLett.117.243602.

[43] S. Mittal et al. “Temporal and spectral manipulations of correlated photons using a time lens”. *Phys. Rev. A* 96 (2017), p. 043807. DOI: 10.1103/PhysRevA.96.043807.

[44] G. Patera and M. I. Kolobov. “Temporal imaging with squeezed light”. *Opt. Lett.* 40 (2015), p. 1125.

[45] G. Patera, J. Shi, D. B. Horoshko, and M. I. Kolobov. “Quantum temporal imaging: application of a time lens to quantum optics”. *J. Opt.* 19 (2017), p. 054001.

[46] G. Patera, D. B. Horoshko, and M. I. Kolobov. “Space-time duality and quantum temporal imaging”. *Phys. Rev. A* 98 (2018), p. 053815. DOI: 10.1103/PhysRevA.98.053815.

[47] J. Shi, G. Patera, M. I. Kolobov, and S. Han. "Quantum temporal imaging by four-wave mixing". *Opt. Lett.* 42 (2017), pp. 3121–3124. DOI: 10.1364/OL.42.003121.

[48] J. Shi, G. Patera, D. B. Horoshko, and M. I. Kolobov. "Quantum temporal imaging of antibunching". *J. Opt. Soc. Am. B* 37 (2020), pp. 3741–3753. DOI: 10.1364/JOSAB.400270.

[49] C. Joshi et al. "Picosecond-resolution single-photon time lens for temporal mode quantum processing". *Optica* 9 (2022), pp. 364–373. DOI: 10.1364/OPTICA.439827.

[50] R. J. Glauber. "The Quantum Theory of Optical Coherence". *Phys. Rev.* 130 (1963), pp. 2529–2539. DOI: 10.1103/PhysRev.130.2529.

[51] L. Mandel and E. Wolf. *Optical Coherence and Quantum Optics*. Cambridge: Cambridge University Press, 1995. DOI: 10.1017/CBO9781139644105.

[52] Y. Arakawa and M. J. Holmes. "Progress in quantum-dot single photon sources for quantum information technologies: A broad spectrum overview". *Applied Physics Reviews* 7 (2020). DOI: 10.1063/5.0010193.

[53] C. Toninelli et al. "Single organic molecules for photonic quantum technologies". *Nature Materials* 20 (2021), pp. 1615–1628. DOI: 10.1038/s41563-021-00987-4.

[54] M. W. Doherty et al. "The nitrogen-vacancy colour centre in diamond". *Physics Reports* 528 (2013), pp. 1–45. DOI: 10.1016/j.physrep.2013.02.001.

[55] A. Christ et al. "Probing multimode squeezing with correlation functions". *New Journal of Physics* 13 (2011), p. 033027. DOI: 10.1088/1367-2630/13/3/033027.

[56] F. Sośnicki, M. Mikołajczyk, A. Golestani, and M. Karpiński. "Interface between picosecond and nanosecond quantum light pulses". *Nat. Photonics* 17 (2023), pp. 761–766. DOI: 10.1038/s41566-023-01214-z.

[57] M. Fox. *Quantum Optics: An Introduction*. Oxford Master Series in Physics. OUP Oxford, 2006.

[58] R. W. Boyd. *Nonlinear Optics*. New York: Academic Press, 2008.

[59] D. Walls and G. J. Milburn, eds. *Quantum Optics*. Springer Berlin Heidelberg, 2008. DOI: 10.1007/978-3-540-28574-8.

[60] G. P. Agrawal, P. L. Baldeck, and R. R. Alfano. "Temporal and spectral effects of cross-phase modulation on copropagating ultrashort pulses in optical fibers". *Phys. Rev. A* 40 (1989), pp. 5063–5072. DOI: 10.1103/PhysRevA.40.5063.

[61] D. B. Horoshko, M. M. Eskandary, and S. Y. Kilin. "Quantum model for traveling-wave electro-optical phase modulator". *J. Opt. Soc. Am. B* 35 (2018), pp. 2744–2753. DOI: 10.1364/JOSAB.35.002744.

[62] M. I. Kolobov. “The spatial behavior of nonclassical light”. *Rev. Mod. Phys.* 71 (1999), p. 1539.

[63] R. Loudon. *The Quantum Theory of Light.* 2nd ed. Oxford: Oxford University Press, 1983.

[64] R. Hanbury Brown and R. Q. Twiss. “Correlation between Photons in two Coherent Beams of Light”. en. *Nature* 177 (1956), pp. 27–29.

[65] R. Hanbury Brown and R. Q. Twiss. “Interferometry of the intensity fluctuations in light - I. Basic theory: the correlation between photons in coherent beams of radiation”. en. *Proc. R. Soc. Lond.* 242 (1957), pp. 300–324.

[66] R. Hanbury Brown and R. Q. Twiss. “Interferometry of the intensity fluctuations in light. II. An experimental test of the theory for partially coherent light”. en. *Proc. R. Soc. Lond.* 243 (1958), pp. 291–319.

[67] U. Fano. “Quantum theory of interference effects in the mixing of light from phase-independent sources”. en. *Am. J. Phys.* 29 (1961), pp. 539–545.

[68] H. J. Kimble, M. Dagenais, and L. Mandel. “Photon Antibunching in Resonance Fluorescence”. *Phys. Rev. Lett.* 39 (1977), pp. 691–695.

[69] M. Henny et al. “The fermionic Hanbury Brown and Twiss experiment”. en. *Science* 284 (1999), pp. 296–298.

[70] L. Mandel. “Sub-Poissonian photon statistics in resonance fluorescence”. *Optics Letters* 4 (1979), p. 205. DOI: 10.1364/ol.4.000205.

[71] C. K. Hong, Z. Y. Ou, and L. Mandel. “Measurement of subpicosecond time intervals between two photons by interference”. *Phys. Rev. Lett.* 59 (1987), pp. 2044–2046. DOI: 10.1103/PhysRevLett.59.2044.

[72] A. M. Brańczyk. “Hong-Ou-Mandel Interference” (2017). arXiv: 1711.00080 [quant-ph].

[73] W. P. Grice and I. A. Walmsley. “Spectral information and distinguishability in type-II down-conversion with a broadband pump”. *Phys. Rev. A* 56 (1997), pp. 1627–1634. DOI: 10.1103/PhysRevA.56.1627.

[74] T. E. Keller and M. H. Rubin. “Theory of two-photon entanglement for spontaneous parametric down-conversion driven by a narrow pump pulse”. *Phys. Rev. A* 56 (1997), pp. 1534–1541. DOI: 10.1103/PhysRevA.56.1534.

[75] W. P. Grice, R. Erdmann, I. A. Walmsley, and D. Branning. “Spectral distinguishability in ultrafast parametric down-conversion”. *Phys. Rev. A* 57 (1998), R2289–R2292. DOI: 10.1103/PhysRevA.57.R2289.

[76] J. B. Spring et al. “Boson Sampling on a Photonic Chip”. *Science* 339 (2013), pp. 798–801. DOI: 10.1126/science.1231692.

[77] V. S. Shchesnovich and M. E. O. Bezerra. “Distinguishability theory for time-resolved photodetection and boson sampling”. *Phys. Rev. A* 101 (2020), p. 053853. DOI: 10.1103/PhysRevA.101.053853.

[78] V. Ansari, J. M. Donohue, B. Brecht, and C. Silberhorn. “Tailoring nonlinear processes for quantum optics with pulsed temporal-mode encodings”. *Optica* 5 (2018), pp. 534–550. DOI: 10.1364/OPTICA.5.000534.

[79] J. Ashby et al. “Temporal mode transformations by sequential time and frequency phase modulation for applications in quantum information science”. *Opt. Express* 28 (2020), pp. 38376–38389. DOI: https://doi.org/10.1364/oe.410371.

[80] M. Karpiński et al. “Control and Measurement of Quantum Light Pulses for Quantum Information Science and Technology”. *Adv. Quantum Technol.* 4 (2021), p. 2000150. DOI: https://doi.org/10.1002/qute.202000150.

[81] V. Giovannetti, L. Maccone, J. H. Shapiro, and F. N. C. Wong. “Generating Entangled Two-Photon States with Coincident Frequencies”. *Phys. Rev. Lett.* 88 (2002), p. 183602. DOI: 10.1103/PhysRevLett.88.183602.

[82] O. Kuzucu et al. “Two-Photon Coincident-Frequency Entanglement via Extended Phase Matching”. *Phys. Rev. Lett.* 94 (2005), p. 083601. DOI: 10.1103/PhysRevLett.94.083601.

[83] R. Shimizu and K. Edamatsu. “High-flux and broadband biphoton sources with controlled frequency entanglement”. *Opt. Express* 17 (2009), pp. 16385–16393.

[84] C. M. Caves and D. D. Crouch. “Quantum wideband traveling-wave analysis of a degenerate parametric amplifier”. *J. Opt. Soc. Am. B* 4 (1987), pp. 1535–1545.

[85] A. Gatti, R. Zambrini, M. San Miguel, and L. A. Lugiato. “Multiphoton multimode polarization entanglement in parametric down-conversion”. *Phys. Rev. A* 68 (2003), p. 053807. DOI: 10.1103/PhysRevA.68.053807.

[86] E. Brambilla, A. Gatti, M. Bache, and L. A. Lugiato. “Simultaneous near-field and far-field spatial quantum correlations in the high-gain regime of parametric down-conversion”. *Phys. Rev. A* 69 (2004), p. 023802. DOI: 10.1103/PhysRevA.69.023802.

[87] D. B. Horoshko, G. Patera, A. Gatti, and M. I. Kolobov. “X-entangled biphotons: Schmidt number for 2D model”. *Eur. Phys. J. D* 66 (2012), p. 239. DOI: 10.1140/epjd/e2012-30099-y.

[88] A. Gatti, T. Corti, E. Brambilla, and D. B. Horoshko. “Dimensionality of the spatiotemporal entanglement of parametric down-conversion photon pairs”. *Phys. Rev. A* 86 (2012), p. 053803. DOI: 10.1103/PhysRevA.86.053803.

[89] D. B. Horoshko et al. “Bloch-Messiah reduction for twin beams of light”. *Phys. Rev. A* 100 (2019), p. 013837. DOI: 10.1103/PhysRevA.100.013837.

[90] L. La Volpe et al. “Spatiotemporal Entanglement in a Noncollinear Optical Parametric Amplifier”. *Phys. Rev. Applied* 15 (2021), p. 024016. DOI: 10.1103/PhysRevApplied.15.024016.

[91] Y. R. Shen. “Quantum Statistics of Nonlinear Optics”. *Phys. Rev.* 155 (1967), pp. 921–931. DOI: 10.1103/PhysRev.155.921.

[92] D. B. Horoshko. “Generator of spatial evolution of the electromagnetic field”. *Phys. Rev. A* 105 (2022), p. 013708. DOI: 10.1103/PhysRevA.105.013708.

[93] B. Huttner, S. Serulnik, and Y. Ben-Aryeh. “Quantum analysis of light propagation in a parametric amplifier”. *Phys. Rev. A* 42 (1990), pp. 5594–5600. DOI: 10.1103/PhysRevA.42.5594.

[94] D. N. Klyshko. *Photons and Nonlinear Optics*. New York: Gordon and Breach, 1988.

[95] W. P. Grice, A. B. U’Ren, and I. A. Walmsley. “Eliminating frequency and space-time correlations in multiphoton states”. *Phys. Rev. A* 64 (2001), p. 063815. DOI: 10.1103/PhysRevA.64.063815.

[96] D. Eimerl et al. “Optical, mechanical, and thermal properties of barium borate”. *J. Appl. Phys.* 62 (1987), pp. 1968–1983. DOI: 10.1063/1.339536.

[97] V. S. Shchesnovich. “Partial indistinguishability theory for multiphoton experiments in multiport devices”. *Phys. Rev. A* 91 (2015), p. 013844. DOI: 10.1103/PhysRevA.91.013844.

[98] J. Shi and T. Byrnes. “Effect of partial distinguishability on quantum supremacy in Gaussian Boson sampling”. *npj Quantum Inf.* 8 (2022), pp. 1–11.

[99] W. J. Smith. “Modern optical engineering: the design of optical systems”. McGraw-Hill, 2000. Chap. 9.

[100] “Handbook of optics: Volume II Devices, Measurements, and Properties”. Ed. by M. Bass. McGraw-Hill, 1995. Chap. 2.

[101] I. P. Christov. “Theory of a ‘time telescope’”. *Optical and Quantum Electronics* 22 (1990), pp. 473–479. DOI: 10.1007/bf02113971.

[102] P. J. Mosley et al. “Heralded Generation of Ultrafast Single Photons in Pure Quantum States”. *Phys. Rev. Lett.* 100 (2008), p. 133601. DOI: 10.1103/PhysRevLett.100.133601.

[103] P. J. Mosley, J. S. Lundeen, B. J. Smith, and I. A. Walmsley. “Conditional preparation of single photons using parametric downconversion: a recipe for purity”. *New J. Phys.* 10 (2008), p. 093011. DOI: 10.1088/1367-2630/10/9/093011.

[104] F. Zernike. “Refractive Indices of Ammonium Dihydrogen Phosphate and Potassium Dihydrogen Phosphate between 2000 Å and 1.5 μ”. *J. Opt. Soc. Am.* 54 (1964), pp. 1215–1220. DOI: 10.1364/JOSA.54.001215.

[105] P. Senellart, G. Solomon, and A. White. “High-performance semiconductor quantum-dot single-photon sources”. *Nature Nanot.* 12 (2017), pp. 1026–1039.

[106] R. Trivedi, K. A. Fischer, J. Vučković, and K. Müller. "Generation of Non-Classical Light Using Semiconductor Quantum Dots". *Adv. Quantum Tech.* 3 (2020), p. 1900007. DOI: https://doi.org/10.1002/qute.201900007.

[107] M. Yu et al. "Integrated femtosecond pulse generator on thin-film lithium niobate". *Nature* 612 (2022), pp. 252–258.

[108] G. Adesso, S. Ragy, and A. R. Lee. "Continuous Variable Quantum Information: Gaussian States and Beyond". *Open Systems & Information Dynamics* 21 (2014), p. 1440001. DOI: 10.1142/s1230161214400010.

[109] C. Weedbrook et al. "Gaussian quantum information". *Rev. Mod. Phys.* 84 (2012), pp. 621–669. DOI: 10.1103/RevModPhys.84.621.

[110] D. B. Horoshko and M. I. Kolobov. "Interferometric sorting of temporal Hermite-Gauss modes via temporal Gouy phase" (2023). arXiv: 2310.11918 [quant-ph].

[111] C. K. Law and J. H. Eberly. "Analysis and Interpretation of High Transverse Entanglement in Optical Parametric Down Conversion". *Physical Review Letters* 92 (2004). DOI: 10.1103/physrevlett.92.127903.

[112] B. Brecht, D. V. Reddy, C. Silberhorn, and M. G. Raymer. "Photon Temporal Modes: A Complete Framework for Quantum Information Science". *Phys. Rev. X* 5 (2015), p. 041017. DOI: 10.1103/PhysRevX.5.041017.

[113] F. König and F. N. C. Wong. "Extended phase matching of second-harmonic generation in periodically poled KTiOPO4 with zero group-velocity mismatch". *Applied Physics Letters* 84 (2004), pp. 1644–1646. DOI: 10.1063/1.1668320.

[114] J. Rayleigh. *The Collected Optics Papers of Lord Rayleigh*. The Collected Optics Papers of Lord Rayleigh. Optical Society of America, 1994.

[115] S. A. Hubert et al. "Temporal Lenses for Attosecond and Femtosecond Electron Pulses". *Proceedings of the National Academy of Sciences of the United States of America* 106 (2009), pp. 10558–10563.

Author's publications

Featured in this thesis

- S. Srivastava, D. B. Horoshko, M. Karpiński, B. Brecht, and M. I. Kolobov, "Time-resolved second-order autocorrelation function of parametric downconversion," *in preparation*, (2024).
- S. Srivastava, D. B. Horoshko, and M. I. Kolobov, "Erecting time telescope for photonic quantum networks," Opt. Express 31(23), 38560 (2023).
- S. Srivastava, D. B. Horoshko, and M. I. Kolobov, "Making entangled photons indistinguishable by a time lens," Phys. Rev. A 107(3), (2023).

Not featured in this thesis

- B. Dioum, S. Srivastava, M. Karpiński, and G. Patera, "Temporal cavities as temporal mode filters for frequency combs," arXiv.2303.09155, (2023).

Poster presentations

- "Temporal imaging to make photons indistinguishable", Siegman International School on Lasers, Dublin, Ireland (2023)
- "Making photons indistinguishable by means of a time lens", International Conference on Quantum Communication, Measurement and Computing QCMC, Lisbon, Portugal (2022)

Seminars

- "Time telescope for photonic interconnects" (QuiDiQua workshop) - University of Lille, France (2023)
- Temporal imaging with entangled photons (QuiCHE project workshop) - University of Warsaw, Poland (2023)
- "Time telescope for making photons absolutely indistinguishable" (QuiCHE project workshop) - Heinrich-Heine-University of Düsseldorf, Germany (2022)

ABSTRACT

This dissertation investigates diverse utilizations of temporal imaging systems in the domain of quantum communications and information processing tasks. Firstly, we propose an application of quantum temporal imaging to restore the indistinguishability of the signal and the idler photons produced in type-II spontaneous parametric down-conversion with a pulsed broadband pump. It is known that in this case, the signal and the idler photons have different spectral and temporal properties. We demonstrate that inserting a time lens in one arm of the interferometer and choosing properly its magnification factor restores perfect indistinguishability of the signal and the idler photons and provides 100% visibility of the Hong-Ou-Mandel interference in the limit of high focal group delay dispersion of the time lens. Secondly, we encounter that a single-time-lens imaging system always imparts a residual temporal chirp on the image, which may be detrimental for quantum networks, where the temporal image interacts with other fields. Therefore, we show that a two-time-lens imaging system satisfying the telescopic condition, a time telescope, is necessary and sufficient for creating a chirpless image. We also develop a general theory of a time telescope, find the conditions for loss minimization, and show how an erecting time telescope creating a real image of a temporal object can be constructed. Finally, we study the possibility of measuring the time-resolved second-order autocorrelation function of one of two beams generated in type-II parametric downconversion employing temporal magnification of this beam, bringing its correlation time from the picosecond to the nanosecond scale, resolvable by modern photodetectors. We show that such a measurement enables one to infer directly the degree of global coherence of that beam, which is linked by a simple relation to the number of Schmidt modes characterizing the entanglement between the two generated beams.

Keywords: Spontaneous parametric down-conversion, Temporal imaging systems, Hong-Ou-Mandel interference, Entanglement, Time telescope, Second-order autocorrelation function.

RÉSUMÉ

Cette thèse étudie diverses utilisations des systèmes d'imagerie temporelle dans le domaine des communications quantiques et des tâches de traitement de l'information. Premièrement, nous proposons une application de l'imagerie temporelle quantique pour restaurer l'indiscernabilité des photons signal et complémentaire produits lors d'une conversion paramétrique spontanée de type II avec une pompe à large bande pulsée. Nous savons que dans ce cas, les photons signal et les photons complémentaire ont des propriétés spectrales et temporelles différentes. Nous démontrons que l'insertion d'une lentille temporelle dans un bras de l'interféromètre et le choix approprié de son facteur de grossissement rétablissent une parfaite indiscernabilité des photons signal et complémentaire et fournissent une visibilité à 100% de l'interférence de Hong-Ou-Mandel dans la limite de dispersion du retard du groupe focal élevée de la lentille temporelle. Deuxièmement, nous constatons qu'un système d'imagerie à lentille temporelle unique transmet toujours un "chirp" temporel résiduel à l'image, ce qui peut être préjudiciable aux réseaux quantiques, où l'image temporelle interagit avec d'autres champs. Par conséquent, nous montrons qu'un système d'imagerie à deux lentilles temporelles satisfaisant la condition télescopique, un télescope temporel, est nécessaire et suffisant pour créer une image sans chirp. Nous développons également une théorie générale d'un télescope temporel, trouvons les conditions de minimisation des pertes et montrons comment un télescope temporel non inverseur créant une image droite réelle d'un objet temporel peut être construit. Enfin, nous étudions la possibilité de mesurer la fonction d'autocorrélation du second ordre résolue dans le temps de l'un des deux faisceaux générés lors d'une conversion paramétrique spontanée de type II en utilisant un grossissement temporel de ce faisceau, amenant son temps de corrélation de la picoseconde à l'échelle de la nanoseconde, résoluble par photodétecteurs modernes. Nous montrons qu'une telle mesure permet de déduire directement le degré de cohérence globale de ce faisceau, qui est lié par une simple relation au nombre de modes de Schmidt caractérisant l'intrication entre les deux faisceaux générés.

Mots clés: Conversion paramétrique spontanée, Systèmes d'imagerie temporelle, Interférence de Hong-Ou-Mandel, Intrication, Télescope temporel, Fonction d'autocorrélation de second order.